Classical Applications and Quantum Aspects of Microresonator-based Optical Frequency Combs

Zijiao Yang

Shanghai, China

Bachelor of Science, University of Science and Technology of China, 2016

A Dissertation Presented to the Graduate Faculty

of the University of Virginia in Candidacy for the Degree of

Doctor of Philosophy

Department of Physics

University of Virginia

December 2022

ii

Classical Applications and Quantum Aspects of Microresonator-based Optical Frequency Combs

Zijiao Yang

(ABSTRACT)

Chip-based microresonators have realized the miniaturization of the optical frequency combs in the past two decades. They provide a platform connecting the optical frequencies and the electronic frequencies, which revolutionized areas such as metrology, instrumentation and spectroscopy. The high repetition rate that can go up to 1 THz is one of the most interesting features of the microcombs. The corresponding large comb spacing and high-speed carrier are advantageous to wavelength multiplexing, high-speed RF generation, coherent sampling, and self-referencing. However, the detection of comb repetition rate, the precursor to all comb-based applications, becomes challenging at these repetition rates due to the limited bandwidth of photodiodes and electronics. In the first part of this dissertation, I introduce a new way to detect and stabilize the high microcomb repetition rate that doesn't require high-speed photodiodes or electronic devices. To leverage this feature of high repetition rate and large comb spacing, a microcomb-based arbitrary RF waveform generator (AWG) is demonstrated. This all-optics-based AWG has potential to be fully integrated on a photonic chip and achieve ultra-high analog bandwidths.

On the other hand, a microresonator works as both a cavity and a nonlinear medium. The nonlinear optics process inside the microresonator could contribute to many quantum applications. Over the last few years, a large variety of quantum optics experiments have been performed in the photonic integrated circuits. They opened

new paths towards applications such as quantum computing, quantum metrology and quantum sensing. In the second part of this dissertation, some quantum aspects of the microcombs are introduced and a squeezed quantum microcomb on a chip is demonstrated for the first time, which could serve as a deterministic approach to scale up the quantum system.

Acknowledgments

During the six years of my life in Charlottesville, I had great experience and met great people. I would like to thank my advisor, Professor Xu Yi, for his support and guidance. I was fortunate to have a chance to work on a variety of projects and learn the essentials in scientific research. I would like to thank my colleagues and collaborators. Good collaborations are so helpful and lead to productive research. I would like to thank all my friends for the time we spent together and the good memories. I would like to thank my family for their encouragement, support and love.

Contents

x

List of Figures

Chapter 1

Introduction

Optical frequency combs were developed around the beginning of the 21st century and soon let to John L. Hall and Theodor W. Hänsch's winning of the Nobel Prize in Physics in 2005[1, 2]. Optical frequency combs have revolutionized areas such as metrology, time keeping and spectroscopy ever since[3, 4, 5]. A traditional way to generate an optical frequency comb is through a mode-locked laser inside a cavity. In the past 15 years, a new type of optical frequency comb has been developed in microresonators where the Kerr parametric process is used to demonstrate microresonator-based optical frequency combs (microcombs)[6, 7] and dissipative Kerr cavity solitons[8, 9, 10, 11]. Microcombs have a wide range of applications from metrology [12] to spectroscopy[13] and make it possible to miniaturize the optical frequency combs to chip scale through integrated photonics. On the other hand, the quantum aspects of microcomb have been studied recently [14, 15, 16, 17, 18, 19] for its capability of providing hundreds of frequency multiplexed quantum channels from a single microresonator. In this thesis, both classical applications and quantum aspects of microcombs are introduced and discussed.

Chapter 2 is an introduction to the background of optical microresonators and their nonlinear behaviors. Microresonator quality factor, dispersion and lineshapes will be introduced. The dynamics of Kerr frequency combs based on the coupled-mode theory and Lugiato-Lefever equation will also be covered.

Chapter 3 introduces some common factors that impact the dispersion of a microresonator such as material dispersion, geometric dispersion and mode interaction. Different approaches in dispersion engineering and some examples are given.

Chapter 4 covers the conventional electro-optic modulation (EOM) method and a new Vernier frequency division method to detect the high repetition rates of microcombs. Comparison between the EOM method the Vernier frequency division method is shown. The stabilization of the high repetition rate with low rate electronic devices is also demonstrated.

Chapter 5 introduces a concept and experiment of a fully optics based radio-frequency arbitrary waveform generator. Different waveform generations are demonstrated. The performance of the arbitrary waveform generator such as the effective number of bits (ENOB) is discussed.

Chapter 6 is a brief introduction to the background of quantum optics. Basic concepts in quantum optics are covered such as the time evolution in quantum systems, quantum optics states as well as squeezed state generations in nonlinear optics systems.

Chapter 7 is specifically about the two-mode squeezed state generations in microcomb. Concept and theory of two-mode squeezed microcomb are first introduced. Numerical calculation of two-mode squeezed states can be performed based on the theory. The first experimental demonstration of a two-mode squeezed microcomb is then presented.

Chapter 2

Background of microresonator-based frequency comb

2.1 Introduction

An optical frequency comb is a series of laser lines that are discrete and equally spaced on the spectrum. The development of optical frequency comb let to John L. Hall and Theodor W. Hänsch's winning of the Nobel Prize in Physics in 2005[1, 2]. Optical frequency combs have revolutionized metrology, time keeping and spectroscopy [3, 4, 5]. A traditional way to generate an optical frequency comb is through mode-locked laser inside a cavity consists of mirrors and a non-linear crystal, for example, Kerr-lens mode-locking.

The separation between two adjacent spectral lines in a frequency comb is called repetition rate f_{rep}, which is about the free spectral range (FSR) of the cavity or $1/t_r$, where t_r is the round trip time inside the cavity. While the spectral lines in a frequency comb are equally spaced, the distance between zero and any of the spectral lines is not an integer times f_{rep}, i.e. the origin of the frequency axis doesn't overlap

with a spectral line. The offset frequency between the frequency comb and 0 is call carrier envelop offset f_{CEO}. The frequency of the n-th spectral line can be then described as $f_n = f_{CEO} + n \cdot f_{rep}$. Optical frequency combs can work as a bridge between the optics regime (hundreds of THz) and electronics regime (up to hundreds of GHz). A photodiode can not directly detect the oscillation of an optical field. Instead it will only measure the root mean square power of the optical field. By overlapping the light with unknown frequency and the known frequency comb, and appropriately choosing the f_{rep}, the unknown frequency and the closest spectral line in the frequency comb will form a detectable beat for the photodiode.

In the recent decade, optical frequency combs have been realized in optical microresonators. They are called microresonator-based optical frequency combs, or microcombs. The development of microcombs opened a new path to many applications such as spectroscopy[13, 20, 21], imaging[22, 23], ranging[24, 25], optical communication[26] and quantum optics[27, 28, 29, 30].

In this chapter, the properties of microresnator will be first introduced, including the quality factor, dispersion and spectral line shapes. The formation of microcomb and soliton states are also discussed.

2.2   Background of optical microresonators

Optical microresonators[31] are a kind of whispering gallery mode resonators[32, 33] at optical frequencies. Light is circulating around the microresonators and trapped inside by total internal reflection.

Small mode volume and low loss are two key features of microresonators. These fea-
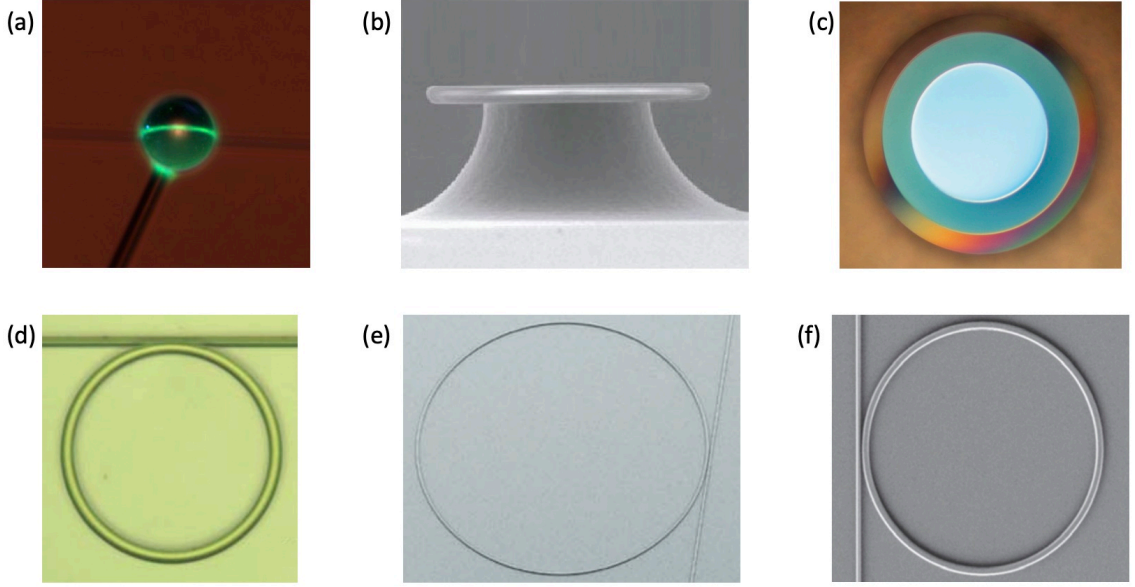
Figure 2.1: **Microresonators of different geometries and materials.** (a) Silica micro-sphere resonator[31]. (b) Silica micro-toroid resonator[34]. (c) Silica micro-disk resonator[35]. (d) Aluminum nitride micro-ring resonator[36]. (e) Lithium niobate micro-ring resonator[37] (f) Silicon nitride micro-ring resonator[38]

.

tures lead to strong nonlinear effects such as microresonator-based optical frequency comb (microcomb)[6] and dissipative Kerr soliton microcomb[9].

In this chapter, key properties such as quality factor, dispersion, spectral line shapes and coupling regimes of microresonators will be introduced, followed by the theoretical background of soliton microcombs.

2.2.1 Basic concept of microresonators

At the resonances of a microresonator, the round-trip optical path is approximately an integer times the wavelength,

$$2\pi n r = m\lambda_m, \tag{2.1}$$

where n is the index of refraction, r is the radius of the microresonator, λ_m is the wavelength in vacuum of the m-th resonant wavelength. The free spectral range (FSR) is the spacing between two adjacent resonant frequencies,

$$FSR = \frac{c_0}{2\pi nr},$$

(2.2)

where c_0 is the speed of light in vacuum. Eq. (2.2) indicates that in the case without dispersion, i.e. n is a constant, FSR is also a constant at different wavelengths. The dispersive case will be discussed in section 2.2.3 as well as in chapter 3.

2.2.2 Quality factor of microresonators

Because of factors such as material absorption and scattering, the energy of the optical mode in a microresonator is dissipating over time. The cavity dissipation rate κ is defined as the ratio between the energy dissipation speed and the total energy stored in the cavity,

$$\frac{dE_{stored}}{dt} = -\kappa E_{stored}.$$

(2.3)

If there is no coupling to the cavity, the stored energy in a cavity decays exponentially over time,

$$E_{stored}(t) = E_{stored}(0)e^{-\kappa t}.$$

(2.4)

Since κ is usually related to the angular frequency ω of the optical mode, quality factor Q is defined as the ratio between stored energy in the cavity and the energy

dissipation per optical cycle,

$$Q = \frac{E_{stored}}{-dE_{stored}/d\omega t} = \frac{\omega}{\kappa}.$$ (2.5)

Under this definition, the quality factor Q is much less frequency related compared to κ, while Q could be slightly different at different frequencies due to frequency-dependent material absorption and scattering.

2.2.3 Dispersion in microresonators

For two adjacent longitudinal modes of the same transverse mode family in a microresonator, the frequency separation between them is the FSR. In the real world case, because of the dispersion, the FSR is not a constant at different wavelengths and the resonance frequencies are not equally spaced. The resonance frequency ω_μ (angular frequency) of the μ-th resonance, or mode number μ, can be written in the Taylor expansion form,

$$\omega_\mu = \omega_0 + D_1\mu + \frac{1}{2}D_2\mu^2 + \sum_{j=3}^{\infty}\frac{1}{j!}D_j\mu^j,$$ (2.6)

where ω_0 is resonance frequency at mode zero, D_j is the j-th order dispersion. D_1 equals to $2\pi FSR$ and D_2 is related to the group velocity dispersion (GVD). D_2 can be connected to the dispersion parameter β_2 and D_1,

$$D_2 \approx -\frac{c}{n}\beta_2 D_1^2,$$ (2.7)

where n is the index of refraction. All the dispersion terms can be defined as integrated
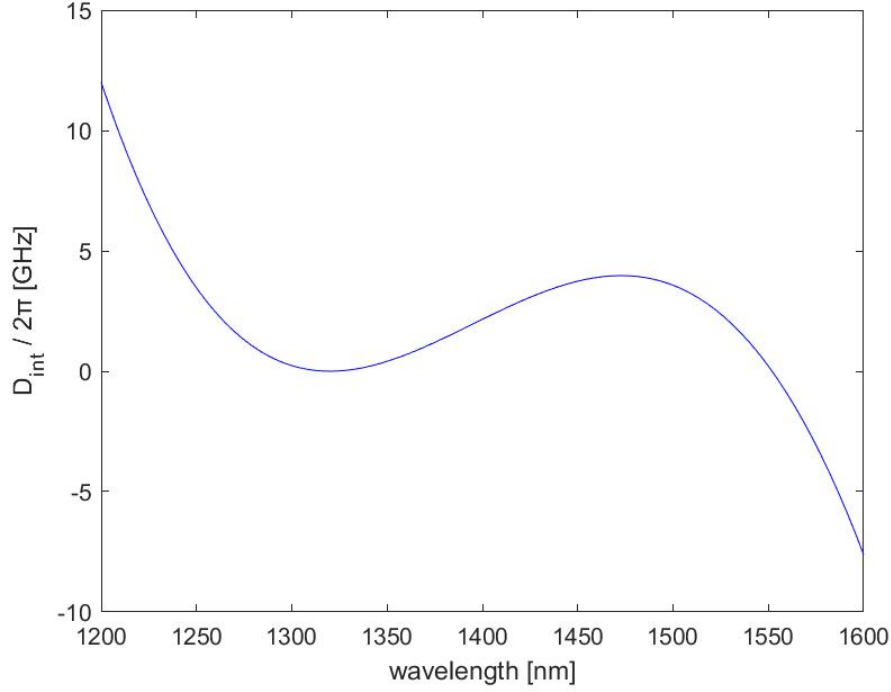
Figure 2.2: A microresonator mode spectrum that contains both normal and anomalous dispersion regimes.

dispersion,

$$D_{int}(\mu) = \sum_{j=2}^{\infty} \frac{1}{j!} D_j \mu^j. \tag{2.8}$$

It is called anomalous dispersion regime when $D_{int} > 0$ and normal dispersion regime when $D_{int} < 0$. This is slightly different from the dispersion regime defined with $dn/d\lambda$, but the two definitions do overlap in a wide range. In the case when D_2 dominates the dispersion, we usually refer to $D_2 > 0$ as anomalous dispersion and $D_2 < 0$ as normal dispersion.

2.2.4 Properties of the optical modes

2.3 Coupling in microresonators

Light is typically coupled into and out of a microresonator through a tapered fiber or bus waveguide. When the laser is being swept across the resonance, the spectrum of the resonance can be recorded with a photodiode as a transmission versus frequency figure.

2.3.1 Spectral line shapes of microresonator's resonances

The resonance spectrum can be derived from coupled-mode theory[39]. The coupling rate between the microresonator and tapered fiber or bus waveguide is κ_{ext}. The intrinsic loss of the resonator is κ_0. The dissipation in Eq.(2.3) involves two terms $\kappa = \kappa_0 + \kappa_{ext}$. The equation of motion for the optical field A is given by,

$$\frac{dA(t)}{dt} = -\frac{\kappa_0 + \kappa_{ext}}{2}A + \sqrt{\kappa_{ext}}S_{in}e^{-i(\omega-\omega_0)t}, \tag{2.9}$$

where S_{in} is the pump field that is being coupled into the cavity and ω is the pump frequency. Transform Eq.(2.9) to a relative frequency frame and take $a(t) = A(t)e^{i(\omega-\omega_0)t}$ and $s_{in} = S_{in}e^{i(\omega-\omega_0)t}$, we obtain

$$\frac{da(t)}{dt} = -i(\omega_0 - \omega)a - \frac{\kappa}{2}a + \sqrt{\kappa_{ext}}s_{in}. \tag{2.10}$$

In the steady state where $da(t)/dt = 0$, the optical field becomes

$$a = \frac{\sqrt{\kappa_{ext}}}{i(\omega_0 - \omega) + \kappa/2} s_{in}. \tag{2.11}$$

The transmitted field is given by

$$s_{out} = s_{in} - \sqrt{\kappa_{ext}} a. \tag{2.12}$$

The resonance spectrum can be recorded on a photodiode and the optical power is detected. The transmission can be calculated by taking the ratio between the output optical power and input optical power,

$$T(\omega) = \frac{|s_{out}|^2}{|s_{in}|^2} = 1 - \frac{\kappa_0 \kappa_{ext}}{(\omega_0 - \omega)^2 + (\kappa_0 + \kappa_{ext})^2/4}. \tag{2.13}$$

This is a Lorentzian lineshape and the full width at the half maximum (FWHM), or linewidth, is equals to κ which is the total dissipation rate of the cavity including intrinsic loss and coupling rate. By sweeping the laser frequency across the cavity resonance and recording the resonance spectrum, the loaded quality factor can be calculated from the linewidth

$$Q = \frac{\omega}{\kappa} = \frac{\omega}{\kappa_0 + \kappa_{ext}}. \tag{2.14}$$

2.3.2 Different coupling regimes

According to the strength of the coupling rate κ_{ext}, the coupling condition can be defined as three regimes,

Under-coupling $\kappa_0 > \kappa_{\text{ext}}$: In the under-coupled regime, cavity dissipation is faster than the coupling rate. This is a weak coupling condition. When κ_{ext} is much smaller than κ_0, the calculated loaded quality factor can be approximated as the intrinsic quality factor.

Critical coupling $\kappa_0 = \kappa_{\text{ext}}$: In the critically coupled regime, cavity dissipation is equals to the coupling rate. Transmission under critical coupling is zero. Critical coupling requires the minimum power for a soliton state.

Over-coupling $\kappa_0 < \kappa_{\text{ext}}$: In the over-coupled regime, cavity dissipation is larger than the coupling rate. This regime is ideal for quantum optics expriments.

The loading condition of the waveguide to resonator coupling can be characterized by escape efficiency $\eta = \kappa_{ext}/\kappa$. Different coupling regimes correspond to different escape efficiency values: $0 < \eta < 0.5$ for under-coupling, $\eta = 0.5$ for critical coupling and $0.5 < \eta < 1$ for over-coupling.

The dip of the resonance lineshape can be achieved by taking $\omega = \omega_0$ in Eq.(2.13)

$$T(\omega) = (\frac{\kappa_0 - \kappa_{ext}}{\kappa_0 + \kappa_{ext}})^2. \tag{2.15}$$

Eq.(2.15) is a quadratic equation for κ, so for a certain transmission T and loaded quality factor Q, there are two possible κ_{ext} can be derived. It's not possible to know if the cavity is under-coupled or over-coupled only judging from its transmission. One possible way to know the actual transmission is to gradually changing the coupling rate to the cavity either by changing the location of the tapered-fiber, or having a series of cavities that have different coupling conditions on a photonic integrated circuit. Another possible method is to measure loaded quality factors and lineshapes at

different wavelengths, as the coupling rate normally increases with larger wavelength. However, the intrinsic quality factor is usually wavelength dependent as well, so this method is not always reliable.

2.4 Kerr frequency combs

Kerr microresonator based optical frequency combs (microcombs)[6] and dissipative Kerr solitons[9] have been realized in the past two decades. The dynamics of Kerr microcombs can be describe by coupled mode theory[34, 40]. For the more complicated dissipative Kerr solitons, the time domain coupled mode equations, known as Lugiato-Lefever Equation (LLE)[41, 42, 43, 9], is a more convient way to describe its dynamics.

2.4.1 Kerr nonlinearity

Kerr microcombs form because of Kerr effect, which is a third-order nonlinearity. In parametric nonlinear optical processes, where the material's quantum state is unchanged, the dielectric polarization of the material can be written by a Taylor expansion in terms of the electric field[44]

$$\mathbf{P} = \epsilon_0 \chi^{(1)} \cdot \mathbf{E} + \epsilon_0 \chi^{(2)} : \mathbf{EE} + \epsilon_0 \chi^{(3)} \vdots \mathbf{EEE} + \cdots , \qquad (2.16)$$

where ϵ_0 is the vacuum permittivity and $\chi^{(1)}$, $\chi^{(2)}$, $\chi^{(3)} \cdots$ are the components of the electric susceptibility. In a linear material, only the first term is significant and that is the linear index of refraction n_0. The third order electric susceptibility $\chi^{(3)}$ is known

as the Kerr effect. Compared to the second-order nonlinearty, Kerr effect doesn't require the materails to be free of centrosymmetry. The dielectric polarization that associates with the Kerr effect can be written as

$$\mathbf{P_4} = \frac{3\epsilon_0}{4}\chi^3[|E_4|^2E_4 + 2(|E_1|^2 + |E_2|^2 + |E_3|^2)E_4 + 2E_1E_2E_3e^{i\theta_+} + 2E_1E_2E_3^*e^{i\theta_-}], \quad (2.17)$$

where θ_+ and θ_- are defined as

$$\theta_+ = (k_1 + k_2 + k_3 - k_4)z - (\omega_1 + \omega_2 + \omega_3 - \omega_4)t, \quad (2.18)$$

$$\theta_- = (k_1 + k_2 - k_3 - k_4)z - (\omega_1 + \omega_2 - \omega_3 - \omega_4)t. \quad (2.19)$$

The first term in Eq.(2.17) corresponds to the self phase modulation (SPM). The second to the fourth terms are for the cross phase modulation (XPM). The last two terms result from four wave mixing (FWM). The efficiency of the FWM process depends on the phase matching θ_+ and θ_-. The result from SPM is equivalent to an index of refraction that increases linearly with the intensity of the light

$$n(I) = n_0 + n_2I, \quad (2.20)$$

where n_2 is the Kerr nonlinear refractive index.

2.4.2 Coupled mode equations

The formation of the Kerr frequency combs can be described by coupled mode equations. The equations of motion for the field of the $\mu - th$ mode A_μ can be written as[34, 45, 40]

$$\frac{dA_\mu}{dt} = -(i\omega_\mu + \kappa/2)A_\mu + \delta_{0,\mu}\sqrt{\frac{\kappa_{ext}P_{in}}{\hbar\omega_0}}e^{-i\omega_p t} + ig\sum_{\mu_1,\mu_2,\mu_3} A_{\mu_1}A_{\mu_2}A_{\mu_3}^*, \qquad (2.21)$$

where P_in is pump power, ω_p is the pump frequency, $g = \hbar\omega_0^2 cn_2/(n_0 V_{eff})$ is the equivalent Kerr nonlinear coefficient, c is the speed of light. V_{eff} is the effective cavity mode volume which is defined as the circumference times the effective mode area A_{eff}

$$V_{eff} = 2\pi r \cdot A_{eff} = 2\pi r \cdot \frac{\int(|E(x,y)|^2 dA)^2}{\int |E(x,y)|^4 dA} \qquad (2.22)$$

$|A_\mu|^2$ is normalized to the unit of photon number. In this section, g is taken as a constant for all mode numbers. This can be understood as an approximation with a narrow span of the frequency comb.

With a relative frequency frame transform by taking $a_\mu = A_\mu e^{i(\omega_p + D_1\mu)}$ in Eq.(2.21), the fast oscillating optical field in A_μ can be eliminated. Eq.(2.21) can be then written as

$$\frac{da_\mu}{dt} = -(i\omega_\mu - i\omega_p - iD_1\mu + \kappa/2)a_\mu + \delta_{0,\mu}f + ig\sum_{\mu_1,\mu_2,\mu_3} a_{\mu_1}a_{\mu_2}a_{\mu_3}^* e^{-iD_1(\mu_1+\mu_2-\mu_3-\mu)t},$$

$$(2.23)$$

where $f = \sqrt{\kappa_{ext}P_{in}/\hbar\omega_0}$ is the normalized pump. In microresonators, there is usually $\kappa \ll D_1$, so that only when phase matching condition is satisfied, i.e. $\mu_3 = \mu_1 + \mu_2 - \mu$, the FWM term in the equation above has non-zero contribution. The coupled mode equations can be then simplified to

$$\frac{da_\mu}{dt} = -(i\omega_\mu - i\omega_p - iD_1\mu + \kappa/2)a_\mu + \delta_{0,\mu}f + ig\sum_{\mu_1,\mu_2} a_{\mu_1}a_{\mu_2}a^*_{\mu_1+\mu_2-\mu}. \qquad (2.24)$$

The threshold of the parametric oscillation can be derived from Eq.(2.24 when only considering the pump mode $\mu = 0$ and a pair of the primary sidebands $\mu = \pm m$ [34, 45, 40]

$$P_{th} = \frac{\kappa^2 n_0^2 V_{eff}}{8\eta\omega_0 cn_2}. \qquad (2.25)$$

The mode number of the primary sidebands can be derived at the same time,

$$m = \sqrt{\frac{\kappa}{D_2}(\sqrt{\frac{P_{in}}{P_{th}} - 1} + 1)}. \qquad (2.26)$$

2.4.3 Lugiato-Lefever equation

Coupled mode equations describe the dynamics of the frequency combs in the frequency domain. A time domain overall optical amplitude $A(\phi, t)$ can be defined as the optical amplitude at the azimuthal angle ϕ in a microresonator. With this definition, it is possible to transform the coupled mode equations to time domain by discrete Fourier transform

$$A(\phi, t) = \sum_{\mu} a_{\mu} e^{i\mu\phi} \tag{2.27}$$

$$\frac{dA(\phi, t)}{dt} = i\frac{D_2}{2}\frac{\partial^2 A}{\partial \phi^2} + ig|A|^2 A - i\delta\omega A - \frac{\kappa}{2}A + f. \tag{2.28}$$

This is in the same form as the Lugiato-Lefever equation (LLE) [41, 43], where $\delta\omega$ is the pump-resonance detuning $\delta\omega = \omega_0 - \omega_p$. This equation is equivalent to the coupled mode equation that fully describes the dynamics of the microcomb. An analytical soliton solution can be derived from Eq.(2.28) in the absence of loss and gain

$$\frac{dA(\phi, t)}{dt} - i\frac{D_2}{2}\frac{\partial^2 A}{\partial \phi^2} - ig|A|^2 A + i\delta\omega A = 0. \tag{2.29}$$

The soliton solution has a hyperbolic secant form

$$A = B\,sech(\frac{\phi}{\phi_{\tau}}) \tag{2.30}$$

where B is the soliton amplitude and ϕ_{τ} is the pulse width in the azimuth coordinate. Substitute Eq.(2.30) in Eq.(2.29)

$$(\frac{D_2}{2\phi_{\tau}^2} - \delta\omega) + (gB^2 - \frac{D_2}{\phi_{\tau}^2})sech^2(\phi/\phi_{\tau}) = 0. \tag{2.31}$$

This equation can be understood as in a soliton state, the phase shift caused by Kerr nonlinearity balances the phase shift from the dispersion. From this equation, we can get

$$D_2 = gB^2\phi_\tau^2, \tag{2.32}$$

$$\delta\omega = \frac{D_2}{2\phi_\tau^2} = \frac{gB^2}{2}. \tag{2.33}$$

It is indicating that the soliton solutions only exist when the cavity has anomalous dispersion ($D_2 > 0$) and the pump laser is red-detuned ($\delta\omega > 0$). The requirement of anomalous dispersion is to balance the phase shift caused by the Kerr effect. The fact that the pump laser needs to be red-detuned can be understood as a "saturable absorber-like" feature of microresonators. When the optical field in the cavity is in a continuous-wave form, the light intensity is low and the pump laser is red-detuned. While in the case of a soliton state (pulse state), because of the large Kerr phase shift induced by the large light intensity, the pump laser stays back on resonance.

In the case when gain and loss exist, they can be treated as perturbations to obtain an approximated analytical solution to Eq.(2.28)[46, 9]. The solutions show that soliton amplitude B and pulse width ϕ_τ are still in the form of Eq.(2.32) and Eq.(2.33), and they only depend on the pump laser detuning $\delta\omega$. The solutions also set a maximum allowed detuning for a soliton state and the pulse width of the soliton

$$\delta\omega \leq \frac{g\pi^2 f^2}{2\kappa^2}, \tag{2.34}$$

$$\phi_\tau = \sqrt{\frac{D_2}{2\delta\omega}}. \tag{2.35}$$

2.4.4 Numerical methods

The coupled mode equations or Lugiato-Lefever equation don't generally have analytical solutions except for some very specific cases with approximations. Numerical methods are more often used to understand and simulate the dynamics of microcombs. A normalization of the LLE is perferred by taking $t = 2\tau/\kappa$, $\phi = \sqrt{2D_2/\kappa}\theta$ and $A = \sqrt{\kappa/2g}\Phi$, where τ,θ and Φ are the normalized time, azimuthal angle and optical field[9]. By doing the normalization, a more general simulation result can be obtained that could correspond to a series of scenarios. Eq.(2.28) can be written as

$$\frac{d\Phi(\theta,\tau)}{d\tau} = \frac{i}{2}\frac{\partial^2\Phi}{\partial\theta^2} + i|\Phi|^2\Phi - (i\nu + 1)\Phi + \widetilde{f}, \qquad (2.36)$$

where $\nu = 2\delta/\kappa$ is the normalized detuning and $\widetilde{f} = \sqrt{8g/\kappa^3}f$ is the normalized pump. $|\widetilde{f}|^2 = 1$ corresponds to the parametric threshold.

Split-step Fourier method[47, 44] has been used extensively to study the dynamics of pulse propagations in nonlinear dispersive materials, such as soliton propogation in fibers[48] and microresonators[43]. The idea of this method is to obtain an approximate numerical solution by dividing a time interval into two steps and assuming only one of the dispersion and nonlinear effects acts in a single step.

To numerically solve the LLE with split-step Fourier method, in the first step, the optical field evolves only with dispersion. Transform the optical field $\Phi(\theta,\tau)$ into frequency domain by fast Fourier transform (FFT) and applied the phase shift from dispersion, we obtain the optical field $\Phi_D(\tau + \delta\tau)$ only with the effect of dispersion

$$\Phi_D(\tau + \delta\tau) = \text{FFT}^{-1}\{e^{-\frac{i\mu^2}{2}\delta\tau}\text{FFT}[\Phi(\theta,\tau)]\}, \qquad (2.37)$$

where we have used the property of the discrete Fourier transform in Eq.(2.27)

$$\text{FFT}(\frac{i}{2}\frac{\partial^2 \Phi}{\partial \theta^2}) = -\frac{i\mu^2}{2}\text{FFT}[\Phi(\theta, \tau)] = -\frac{i\mu^2}{2}\widetilde{\Phi}(\mu, \tau). \tag{2.38}$$

In the second step, the optical field evolves only with nonlinear effect

$$\Phi(\tau + \delta\tau) = e^{i|\Phi|^2 - i\nu - 1}\Phi_D(\tau + \delta\tau) + \widetilde{f}\delta\tau. \tag{2.39}$$

Chapter 3

Dispersion engineering of microresonators

3.1 Introduction

An important feature of microresonators is their capability to be designed and fabricated to have desired dispersion behaviors. Compared to bulk optics, integrated microresonators have more degrees of freedom to be tailored in order to have a specific dispersion spectrum. This process is known as dispersion engineering, which can be done in multiple approaches such as cavity cross section design[49] and material modifications[50]. Dispersion engineering of microresonators plays important roles in applications such as microcomb bandwidth and power shaping[49], self-referencing with dispersive wave[51] and quantum microcomb[30].

3.2 Factors of dispersion

Dispersion in a microresonator depends a variety of factors. The most common ones are materials dispersion, geometric dispersion and mode-interaction-induced dispersion[44].

3.2.1   Material dispersion

The index of refractive of a material usually depends on the frequency ω of the optical field. This property is call chromatic dispersion and it is the nature of a material. This dispersion is related to the resonance frequencies of a material where the material absorbs the optical field. When the optical field frequency ω is far from the material resonance frequencies, the index of refraction can be approximated by the Sellmeier equation[44]

$$n^2(\omega) = 1 + \sum_j \frac{B_j \omega_j^2}{\omega_j^2 - \omega^2}, \tag{3.1}$$

where ω_j are the material resonance frequencies and B_j is the strength of the j-th resonance. In many materials, the chromatic dispersion results in a normal dispersion regime over a broad range of wavelengths. As we discussed in Section 2.4.3, anomalous dispersion is required for soliton states. For those materials with normal chromatic dispersion[52], certain dispersion engineering is needed in order to generate soliton states.

3.2.2   Geometric dispersion

The optical field is not always confined in a single material, such as in optical fibers or waveguides (Fig.3.2). The propagation constant of the optical mode depends on the distribution of the optical mode and the materials around. Effective index of refractive for this optical mode can be defined as the ratio between the propagation constant β and the wavenumber in vacuum k_0 [44]
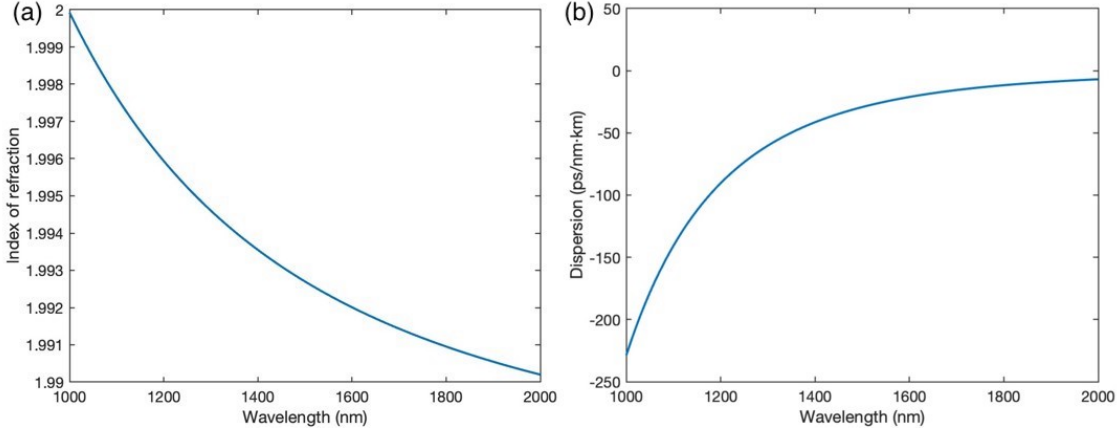
Figure 3.1: **Index of refraction and dispersion of bulk Si$_3$N$_4$** (a) Index of refraction of bulk Si$_3$N$_4$ decreases with increasing wavelength. (b) Bulk Si$_3$N$_4$ experiences normal chromatic dispersion. Two traces are numerically calculated with the refractive index equation $n = \sqrt{1 + 2.948\lambda^2/(\lambda^2 - 0.1310^2)}$.

$$n_{\text{eff}} = \frac{\beta}{k_0} = \frac{c}{v_p},$$

(3.2)

where c is the speed of light and v_p is the phase velocity of the optical mode. The effective index of refraction can be numerically calculated with finite element method (FEM), such as COMSOL Multiphysics. To more accurately calculate the absolute mode number m in Eq.(2.1), n_{eff} should be used along with the effective radius r_{eff} of the microresonator as different location on a cross section experiences slightly different radius in a microresonator

$$r_{\text{eff}} = \frac{\int r|E(x,y)|^2 dA}{\int |E(x,y)|^2 dA}.$$

(3.3)

The absolute mode number can be then calculated as

$$m = \frac{2\pi n_{eff} r_{eff}}{\lambda}.$$

(3.4)

Dispersion of different orders D_j can be obtained by doing a polynomial fit for a series of $\{\lambda, m\}$. Effective mode index (EMI) in a microresonator is defined as the product of the effective radius and effective index of refraction

$$\text{EMI} = r_{eff} n_{eff}. \tag{3.5}$$

Therefore the absolute mode number can be written in terms of EMI as

$$m = \frac{2\pi\text{EMI}}{\lambda}. \tag{3.6}$$

In an FEM solver such as COMSOL Multiphysics, the solver output in an axial symmetric model is the EMI instead of n_{eff}.

3.2.3   Mode interaction

Spatial mode interaction is another factor that causes dispersion in a microresonator. Spatial mode interaction can originate from the interaction between different spatial modes in the same cavity[53] or the coupling between spatial modes from different cavities when they are put close together[54].

Spatial mode interaction causes the resonance frequencies of the two cavities deviate from their original locations, thus changes the dispersion behaviors of both cavities. The frequencies of the hybrid modes resulted from the mode interaction are given by[55, 56, 57]

$$\omega_{\mu\pm} = \frac{\omega_{\mu A} + \omega_{\mu B}}{2} \pm \sqrt{G^2 + \frac{1}{4}(\omega_{\mu A} - \omega_{\mu B})^2}, \tag{3.7}$$
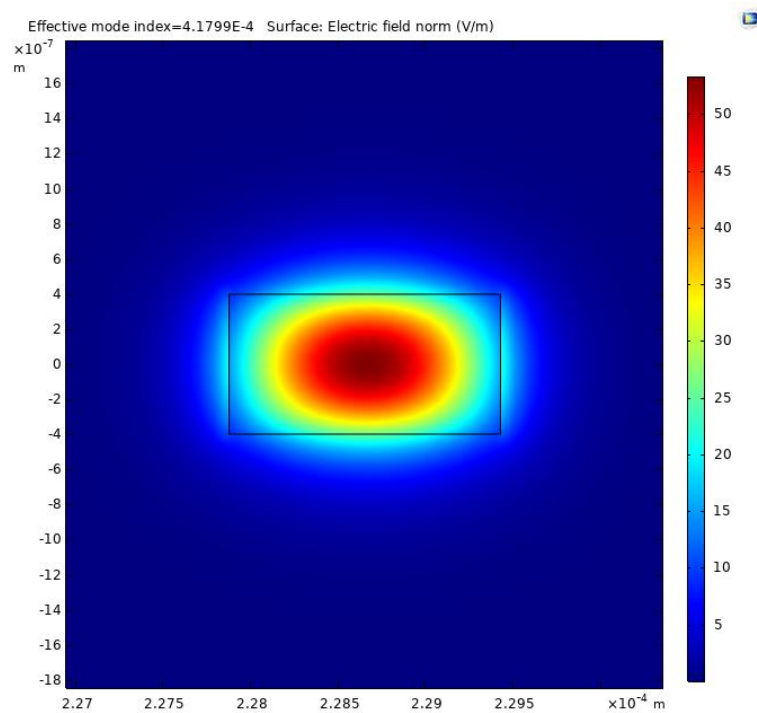
Figure 3.2: **COMSOL FEM simulation of TE$_{00}$ mode of a Si$_3$N$_4$ micro-ring resonator cross section.** The optical mode distributes in both the Si$_3$N$_4$ core and silica cladding. n_{eff} and the effective mode index depend on the distribution of the optical mode and the material properties.
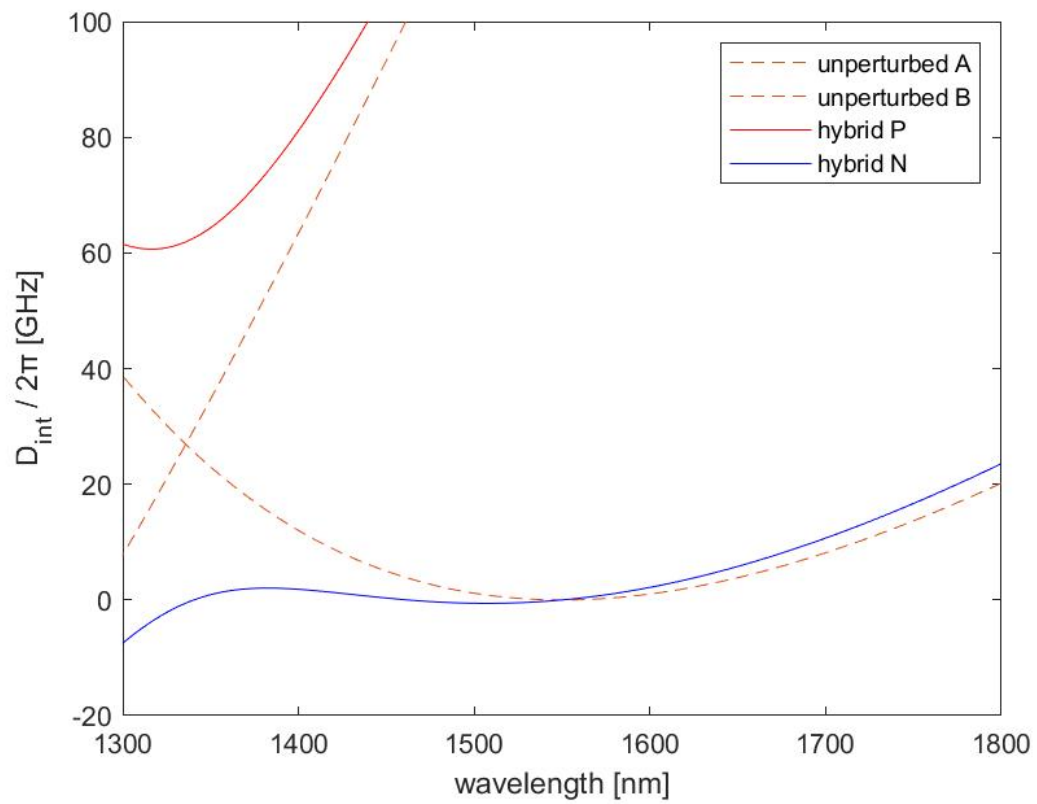
Figure 3.3: **Dispersion caused by spatial mode interaction between two microresonators.** Because of spatial mode interaction, the mode spectra of two cavities deviate from their original parabolic shapes.

where $\omega_{\mu A}$ and $\omega_{\mu B}$ are the frequencies of mode μ in cavity A and B, $\pm$ sign corresponds to the positive and negative branches of the hybrid modes, and G is the coupling rate between the two spatial modes. The dynamics of Kerr frequency combs of the hybrid modes can be studies with the LLE in Eq.(2.28) including interaction terms iGA_A and iGA_B[58]

$$\frac{dA_A(\phi, t)}{dt} = i\frac{D_2}{2}\frac{\partial^2 A_A}{\partial \phi^2} + ig|A_A|^2 A_A - i\delta\omega A_A - \frac{\kappa}{2}A_A + f_A + iGA_B,$$

$$(3.8)$$

$$\frac{dA_B(\phi, t)}{dt} = i\frac{D_2}{2}\frac{\partial^2 A_B}{\partial \phi^2} + ig|A_B|^2 A_B - i\delta\omega A_B - \frac{\kappa}{2}A_B + f_B + iGA_A,$$

where A_A and A_B are the optical fields in cavity A and B respectively, f_A and f_B are the pump for cavity A and B.

3.3 Examples of dispersion engineering

A variety of dispersion profiles can be designed by dispersion engineering with the idea of tailoring the cross section or introducing spatial mode interaction. We will present some examples in this section.

3.3.1 Dispersion for soliton generation

Eq.(2.32) indicates that anomalous dispersion ($D_2 > 0$) is needed for soliton states. By doing FEM simulation on D_2 over a broad range of wavelength, the results show a range of pump wavelengths that are suitable for soliton generations. More usually
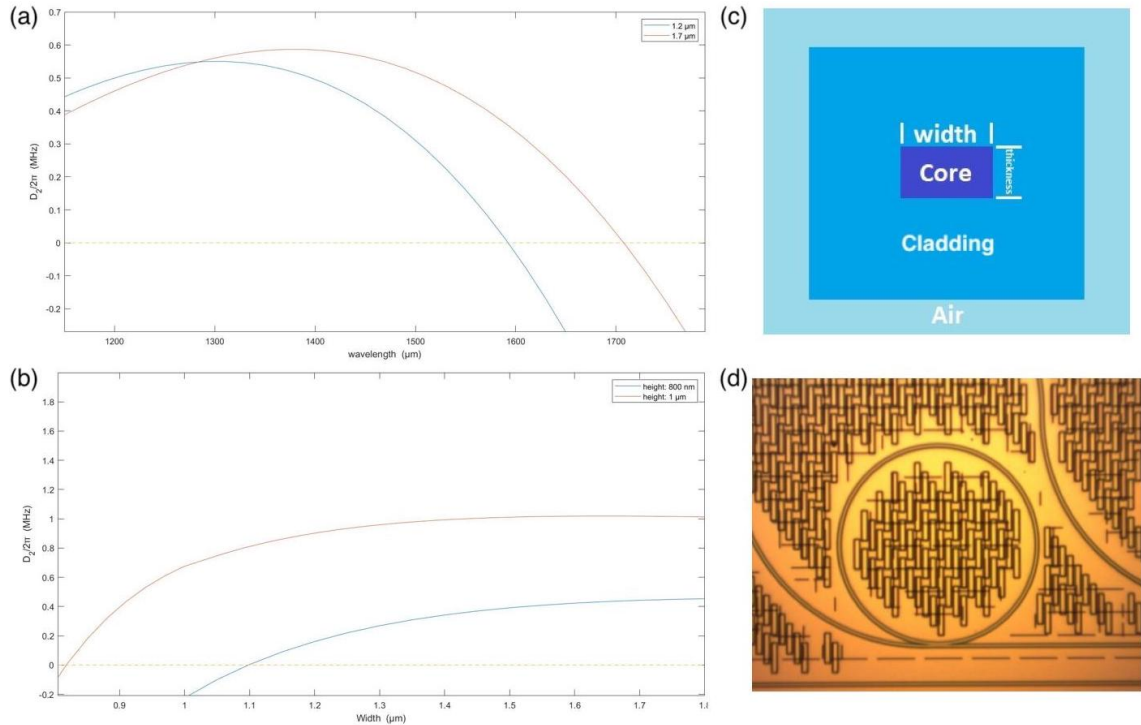
Figure 3.4: **FEM simulation to find anomalous dispersion for SiN micro-ring resonators.** (a) $D_2/2\pi$ at different wavelengths for the same cross section structure. Blue trace has a 1.2 μm × 0.8 μm (width × height (or thickness)) cross section and the red trace has a 1.7 μm × 0.8 μm cross section. Both traces have a radius of 300 μm. (b) $D_2/2\pi$ at different widths for the thickness and wavelength. Blue trace has a thickness of 800 nm and the red trace has a thickness of 1 μm. Both traces have a radius of 300 μm and are at 1550 nm. (c) A schematic of the cross section. (d) A microscopic photo of the SiN micro-ring resonator.

we want to keep the pump at a relatively fixed wavelength. Sweeping the width of the cross section shows what to expect for different dimensions (Fig. 3.4).

3.3.2 Dispersion engineering for microcomb shape tailoring

The shape of the microcomb is mostly determined by the dispersion of the cavity. A cavity with small anomalous dispersion results in a microcomb with broad span (Eq.(2.35)). Dispersive waves are another interesting aspect in the microcomb shape
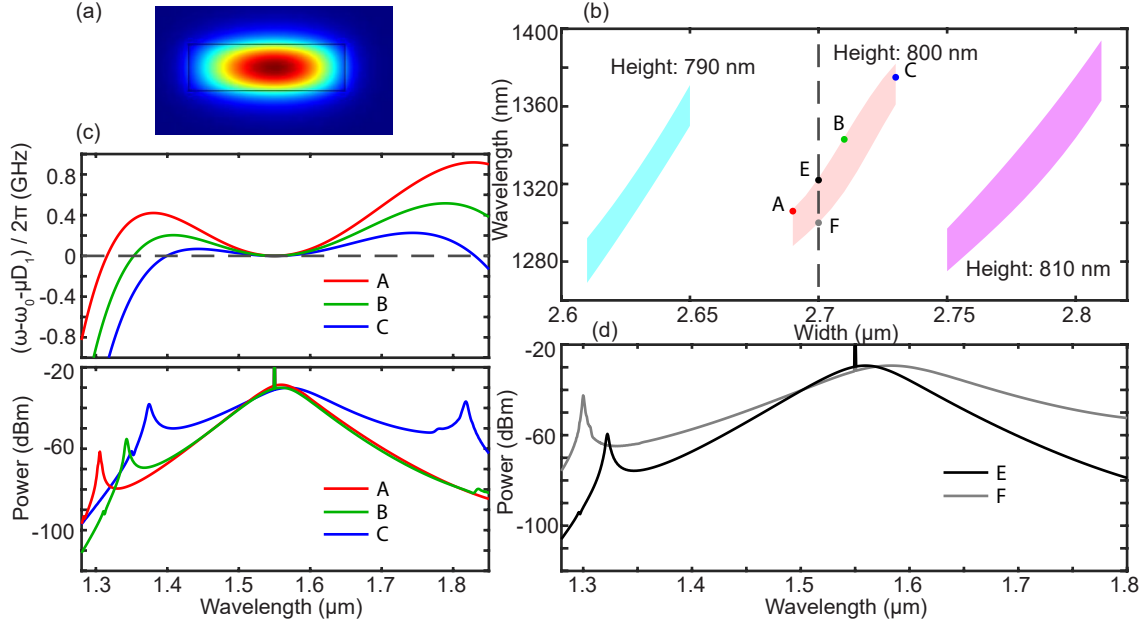
Figure 3.5: **Dispersive generation with cross section tailoring.** (a) The optical mode in a 2.7 μm × 0.8 μm cross section. The cavity is a SiN racetrack cavity that has an FSR of 110 GHz. (b) Dispersive wave existence wavelengths for different cross section dimensions. The location of the dispersive for a specific cross section dimension can be tuned through Raman scattering by changing the pump power. The horizontal direction of each colored region shows how much the fab error tolerance is. (c) Simulated integrated dispersion (top) and corresponding soliton microcombs (bottom). A,B and C correspond to different cross section dimensions in (b). (d) Raman tuning of dispersive wave. E and F correspond to different pump power levels for the same cross section in (b). Microcomb simulations are based on LLE with Raman terms[61].

design. When the span of a microcomb overlap with where the integrated dispersion changes sign, a dispersive could be generated[59, 60]. The result of dispersive increases in the intensity at the modes where this phase-matching is happening. Dispersive waves are sometimes desired for the comb line amplification feature so that a comb line that is further away from the pump can be detectable[51].

Cross section tailoring (Fig. 3.5) or introducing spatial mode interaction (Fig. 3.6) are controllable ways to design a dispersion that supports dispersive waves. Engineering the cross section is a straightforward approach which appears much simpler in the
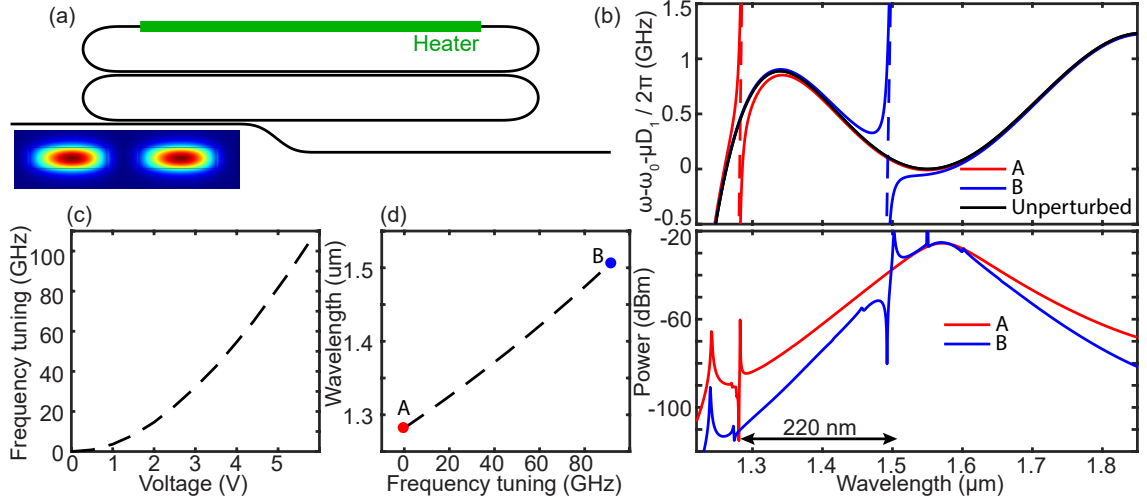
Figure 3.6: **Dispersive generation with spatial mode interaction between two racetrack resonators.** (a) Two racetrack SiN cavities with FSRs of 110 GHz and 110.3 GHz respectively. The coupling rate between two cavities is 1 GHz. Relative resonance frequencies of two cavity are tuned by an integrated heater. (b) Simulated integrated dispersion (top) and corresponding soliton microcombs (bottom). A and B correspond to the lower and upper limits of the integrated heater tuning range on the dispersive wave wavelength. (c) Resonance frequency shift versus integrated heater voltage. (d) Dispersive wave wavelength shift versus integrated heater voltage. Microcomb simulations are based on LLE with spatial mode interaction (Eq.(3.8)).

layout and design. However, the location of the dispersive wave is relatively sensitive to fabrication uncertainties. Introducing mode interaction on the other hand, is not that sensitive to fabrication errors, but is more complicated in the design and operation.

3.3.3 Dispersion for quantum applications

Quantum photonics expriments sometimes require different shapes of dispersion profile than those of the soliton generations. One example is in the squeezed state generation[30] where a flat dispersion profile could be preferred to have equally spaced quantum modes. This can be done by engineering the cross section, such as choosing

the zero dispersion point in Fig. 3.4.

3.4 Mode spectrum measurement

Measuring the mode spectrum in experiment is as important as designing the dispersion. There are multiple approaches to measure the mode spectrum.

Calibrated laser wavelength sweep method is widely used, such as with an Mach-Zehnder interferometer (MZI)[62] or a frequency comb[63], where the laser wavelength is scanned over a broad range and the transmitted signal from the cavity is recorded. The locations of different modes can then be found in data processing (Fig. 3.7 (a)).

In some cases we need the mode spectrum measurement to have higher resolution, such as when measuring a dispersion profile that is close to flat. Electro-optic modulation (EOM) method can be used to achieve a better resolution[30] (Fig. 3.7 (b)). In the EOM method, the pump and the m-th EOM sideband are input to the cavity and the wavelength being scanned across a single resonance mode. By tuning the modulation frequency on the EOM, when the resonance dips created by the pump and the m-th sideband overlap, the sideband is right at the resonance mode number μ. The frequency difference between the pump mode and mode number μ can be obtained as $\Delta f_\mu = m f_{\text{VCO}}$. We can acheive a resolution of 100 kHz or better with EOM method, while the laser scan method usually has a resolution in MHz level. However, EOM method is much slower to operate in experiment than the laser scan method. The measurement span of EOM method is limited by the EOM setup and it's usually much narrower than the laser scan method.
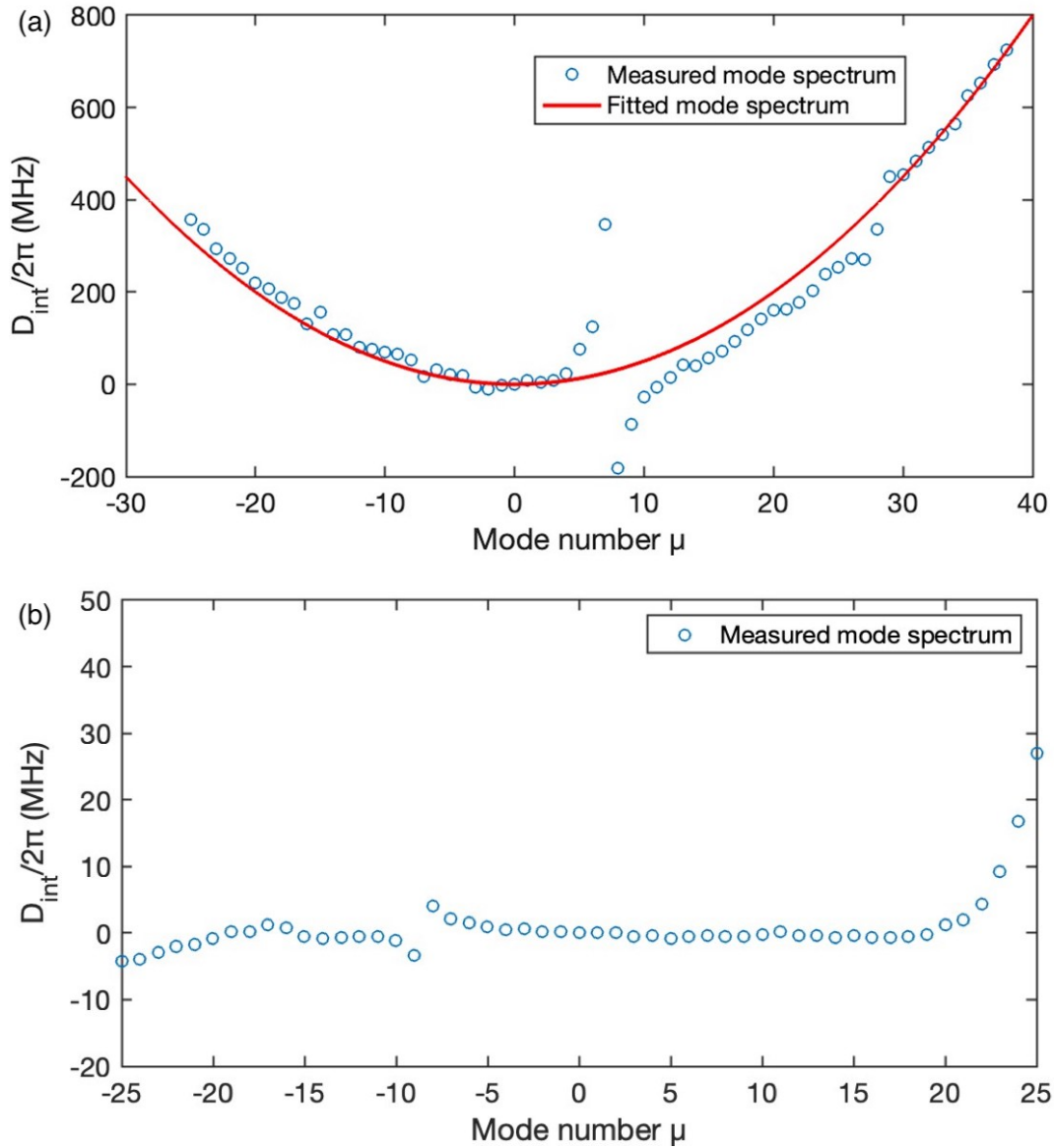
Figure 3.7: **Mode spectrum measurements with different methods.** (a) Mode spectrum of a SiN micro-ring resonator measured with laser scan method. $D_2/2\pi$ is estimated to be 1 MHz with parabolic fit. The FSR of the cavity is about 100 GHz. (b) Mode spectrum of a silica wedge resonator measured with EOM method. The FSR is about 22 GHz.

Chapter 4

Vernier frequency division with dual-microresonator solitons

4.1 Introduction

Dissipative Kerr solitons have been realized in microresonators[9, 10, 11] recently and have been studied intensively for their potential to miniaturize opitcal frequency combs, which have revolutionized metrology, time keeping and spectroscopy [3, 4, 5]. These solitary wave packets leverage Kerr nonlinearity to compensate cavity loss and to balance chromatic dispersion[64, 8, 9]. They output a repetitive pulse stream at a rate set by the resonator roundtrip time, which can range from GHz to THz [65, 66, 67]. The reduction of resonator mode volume increases the intracavity Kerr nonlinearity, lowers the operation pump power and extends the comb spectrum span. This has enabled demonstrations of battery-operated soliton combs at 194 GHz repetition rate[68], and octave-spanning soliton generation for self-referencing in a resonator with 1 THz free-spectral-range (FSR)[12]. High repetition rates (rep-rates) are also desired in many comb-based applications. For instance, the maximum acquisition speed in dual-comb spectroscopy[13, 20, 21], ranging [25, 24], and imaging [22, 23], all increase linearly with the comb repetition rate.

However, to detect the high repetition rate, a microresonator-based frequency comb

(microcomb) system has to include an auxiliary frequency comb whose repetition rate can be directly detected by a photodiode (PD). The detectable repetition frequency is then multiplied up optically through the equally-spaced comb lines to track the microcombs in action [6, 12]. This limits the miniaturization of microcomb system as the area occupied by the resonator scales inverse quadratically with the repetition rate. For the popular electrical K-band, the auxiliary resonator diameter has to exceed several millimeters [35, 62, 69, 70]. An approach to divide and detect microcomb repetition frequency beyond photodiode's bandwidth will be critical to eliminate this restriction, and will advance the frequency comb technology in terms of miniaturization, power consumption and ease of integration.

In this chapter, a Vernier frequency division method is introduced to detect soliton microcomb repetition rate well above the electrical bandwidth in use. In contrast to the conventional approaches, the Vernier frequency division does not require low-rate frequency combs. Instead, the rate of the auxiliary combs, f_{r2}, can be higher than that of the main combs, f_{r1}, and it can be free-running and stay unknown.

4.2   Dual-microresonator solitons generation

To overcome the thermal complexity[71] in soliton generation process and generate single soliton states in two microresonators on seperate chips, a rapid laser frequency sweeping method [72] can be implemented. The first electro-optic modulation (EOM) sideband from a continous wave (CW) laser followed by a phase modulator is used as a rapid-tuning pump laser. The phase modulator is driven by a voltage-controlled oscillator (VCO). The first sideband from the phase modulation is selected by an optical tunable bandpass filter (BPF). The sideband can also be obtained with single
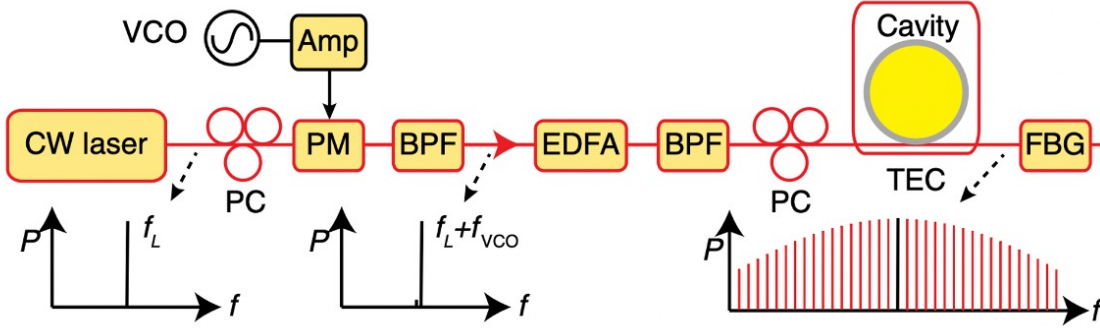
Figure 4.1: **Demonstration of soliton generation in a microresonator with electro-optic modulation sideband sweeping.** The first electro-optic modulation (EOM) sideband from a continous wave (CW) laser followed by a phase modulator is used as a rapid-tuning pump laser. The phase modulator is driven by a voltage-controlled oscillator (VCO). The first sideband from the phase modulation is selected by an optical tunable bandpass filter (BPF). An erbium-doped fiber amplifier (EDFA) is used to amplify the pump laser. Polarization controllers (PC) are used to align the polarization to the phase modulator and the bus waveguide mode. A fiber Bragg grating (FBG) is used to separate the pump and the comb.

sideband modulation through a QPSK modulator[73]. With the fast ramp voltage on the VCO, the pump laser scans at a speed of ~ 20 GHz/μs which is faster than the thermal effect in the microresonator. A 50/50 splitter after the BPF splits the pump laser equally into two erbium-doped fiber amplifiers (EDFAs). The polarization should be carefully adjusted by a polarization controller after each EDFA. The pump laser then is coupled into the bus waveguide by a lensed fiber. Single solitons are generated simultaneously in both microresonators by rapidly scanning the pump laser from the blue-detuned regime to the red-detuned regime. The single soliton existence detuning ranges of both microresonators are thermally tuned to overlap. In our case, each microresonator has a temperature controller with 0.01°C resolution. The resonant frequencies of the SiN micro-ring resonators are tuned ~ 2.5 GHz/°C. Dual-microcomb driven by one pump laser has been previously reported in two cascaded resonators[74], and in a single resonator by counter-propagating and co-propagating
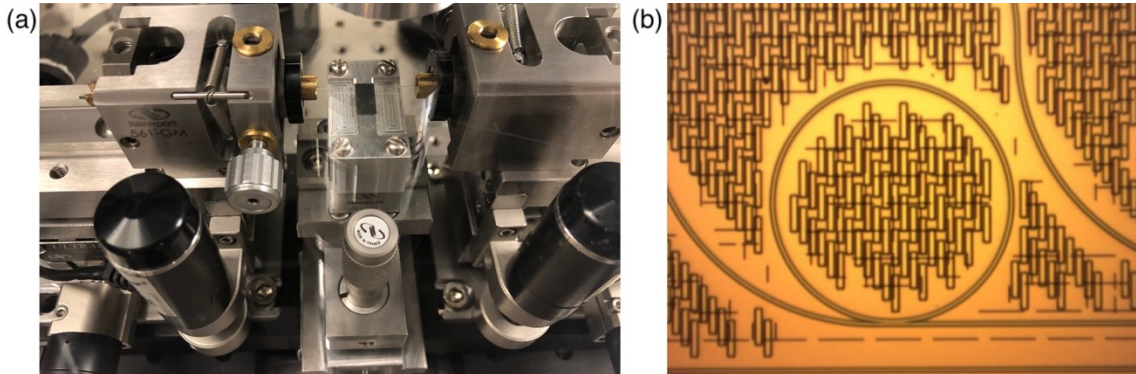
Figure 4.2: **An integrated photonic chip on a coupling stage.** (a) Light is coupled into and out of the bus waveguide on the integrated photonic chip through lensed fibers. (b) A microscopic photo of the SiN micro-ring resonator. Light is coupled to the resonator from the bus waveguide by evanescent field.

pump lasers[75, 76, 77].

4.3 Measuring repetition rates

In this section, the conventional electro-optic modulation (EOM) method and the Vernier division method are introduced.

4.3.1 EOM method

The EOM method configuration is shown in the purple panel in Fig. 4.5. An optical bandpass filter is used to select two adjacent comb lines from the main soliton, which are then amplified by an EDFA. They are then sent into an electro-optic phase modulator which is driven by VCO 2 at a frequency of f_{VCO2}. Modulation sidebands are created for both comb lines, and when the modulation is strong enough, a pair of sidebands will meet in the midpoint of the two comb lines [78]. This pair of sidebands is then optically filtered by a Bragg-grating filter, and is detected on a
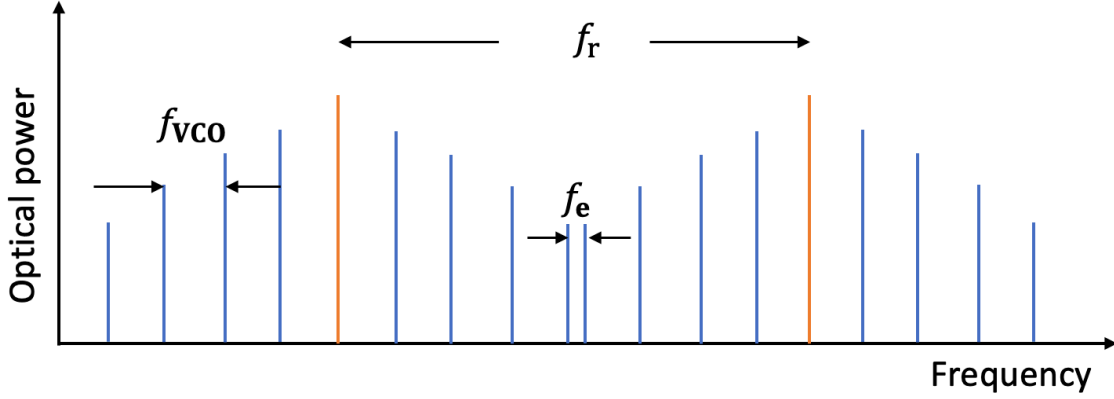
Figure 4.3: **Concept of EOM method to detection comb repetition rate.**
Modulation sidebands are created for both comb lines, and when the modulation is
strong enough, a pair of sidebands will meet in the midpoint of the two comb lines.
The repetition rate can be derived as $f_\mathrm{r} = f_\mathrm{e} + M \times f_\mathrm{VCO}$.

photodiode. Using this method, the repetition rate of the main soliton can be derived
as $f_\mathrm{r1} = f_\mathrm{e} + M \times f_\mathrm{VCO2}$, where M is the number of modulation sidebands between
the two adjacent comb lines and f_e is the beat frequency between the two sidebands
in the middle.

4.3.2 Concept of Vernier frequency division method

The concept is illustrated in Fig. 4.4. The main and Vernier soliton comb lines create
two free-running graduation markings on the optical frequency domain, and similar
to a Vernier caliper, these markings coarsely align periodically. Detectable frequency
beat notes can be created when the frequency of the N-th higher-rate comb line
catches up with that of the $(N + 1)$-th lower-rate comb line. These beat notes can
be utilized to divide the soliton repetition frequency through an electrical frequency
division followed by the subtraction of dual-comb repetition rate difference. Figure
4.4 presents one conceptual example, where the main soliton repetition rate divided
by N can be obtained from the sum of the first beat frequency Δ_1, and the N-th
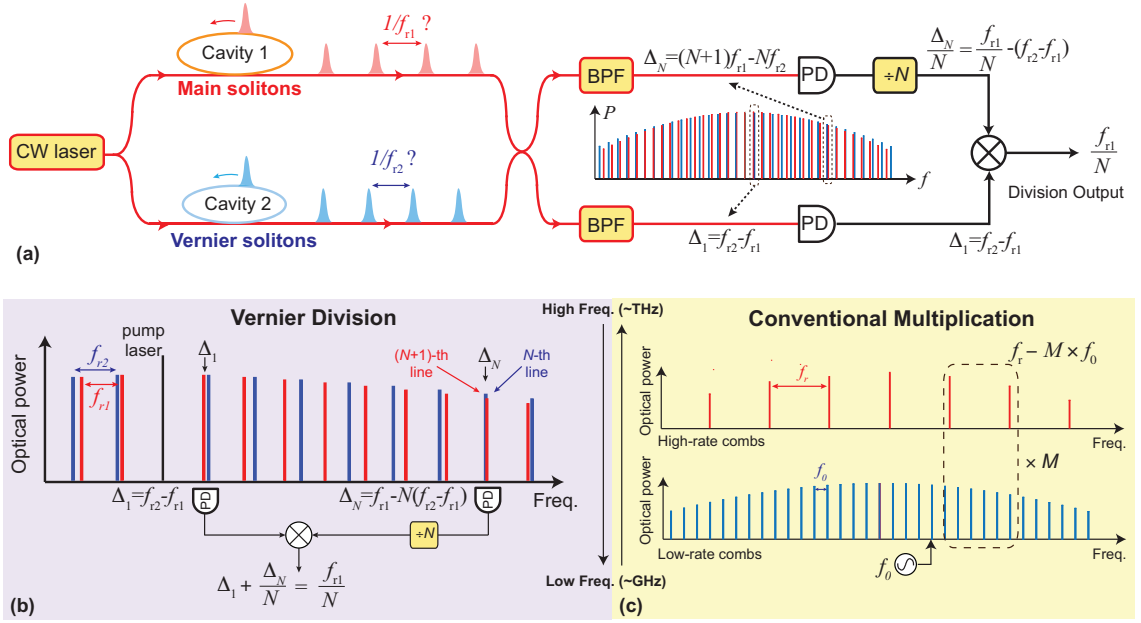
Figure 4.4: **Concept of Vernier dual-comb repetition rate division.** (a) To divide and detect the main soliton (red) repetition rate, a free-running higher rate microcomb (Vernier, blue) is generated to sample and divide down the main soliton rep-rate. Two pairs of low frequency dual-comb beat notes are selected by optical bandpass filters (BPFs) and detected on photodiodes (PDs) to extract the high repetition frequency. (b) The zoomed-in optical spectra to illustrate the Vernier division principle. When the Vernier soliton rep-rate is slightly higher than the main soliton rep-rate, the frequency of the N-th Vernier comb line can coarsely align with the $(N+1)$-th main soliton comb line. The corresponding beat frequency contains information of the absolute repetition rate (f_{r1}) and the repetition rate difference ($f_{r2} - f_{r1}$). The main soliton repetition rate can be divided down by N by electrically dividing Δ_N by N, and then adding it with Δ_1. (c) In comparison, conventional repetition rate detection methods require a low rep-rate comb to optically multiply a low frequency reference to a high frequency, which is then compared to the high repetition rate through heterodyne detection.

beat frequency Δ_N divided by N. Δ_N denotes the beat frequency between the N-th Vernier comb line and its nearest main soliton comb line.

More generally, Vernier frequency division method can use two pairs of comb lines in the overtaking regime, where the frequency of the N-th higher-rate comb line catches up with that of the $(N+1)$-th lower-rate comb line. Here, we use the N-th pair and the M-th pair of comb lines as an example, and $\Delta f_{N,M}$ denotes the frequency difference between the $N(M)$-th Vernier soliton comb line and its nearest main soliton comb line:

$$\Delta f_N = N f_{r2} - (N+1) f_{r1} = N(f_{r2} - f_{r1}) - f_{r1}, \tag{4.1}$$

$$\Delta f_M = M f_{r2} - (M+1) f_{r1} = M(f_{r2} - f_{r1}) - f_{r1}. \tag{4.2}$$

f_{r1} and f_{r2} are the rep-rates of the main solitons and Vernier solitons, respectively. Eq. (4.1)$/N$ subtracted by Eq. (4.2)$/M$ will yield

$$\left(\frac{1}{M} - \frac{1}{N}\right) f_{r1} = \frac{\Delta f_N}{N} - \frac{\Delta f_M}{M}, \tag{4.3}$$

where the repetition rate of the main solitons, f_{r1}, is now expressed by two measurable quantities. In the experiment, photodetecting the corresponding pair of comb lines produces RF signals at the frequency of $\Delta_{M,N}$, where $\Delta_{M,N} = |\Delta f_{M,N}|$. The "$\pm$" ambiguity in $\Delta f_{M,N} = \pm\Delta_{M,N}$ can be resolved by measuring the optical spectral of the main and Vernier solitons.

4.4 Measuring microcomb repetition rate

The Vernier division reduces the required electrical bandwidth for rep-rate detection from the soliton repetition rate to approximately the repetition rate difference between the main and Vernier solitons, which can be coarsely controlled in microfabrication. In this demonstration, the electrical bandwidth is reduced from 197 GHz to 20s GHz. The Vernier method directly applies to 100s GHz to THz rate soliton microcombs, which are common in many material systems, such as Si_3N_4[79, 80, 81, 82], silicon [83], AlN [84], and $LiNbO_3$ [85, 86, 87]. For a fixed electrical bandwidth and rep-rate difference, a higher main soliton rep-rate will demand a broader comb span in the Vernier method. This is because the number of comb lines required for the comb line frequency of Vernier solitons to overtake that of the main solitons increases linearly with the main soliton repetition rate. At 1 THz repetition rate, 50 comb lines on one side of the pump are needed for 20 GHz rep-rate difference, and this comb span has been reported previously [66, 67]. The Vernier division demonstrated in this manuscript could serve as a universal solution for repetition rate detection in various microcomb systems and applications.

In this experiment, the main and Vernier solitons are generated in bus-waveguide coupled Si_3N_4 microresonators [88], which have FSRs of 197 GHz and 216 GHz, intrinsic quality factors of 1.5×10^6 and 2.2×10^6, and loaded quality factors of 1.3×10^6 and 1.8×10^6, respectively. The complete experimental setup is shown in Fig. 4.5.

In our measurement, we select $N = 11$ and $M = 9$ for the Vernier frequency division. $\Delta_9 = 22.7$ GHz and $\Delta_{11} = 16.1$ GHz are obtained by photodetecting the corresponding pairs of comb lines. These two RF signals are then amplified to ~ 3 dBm to meet
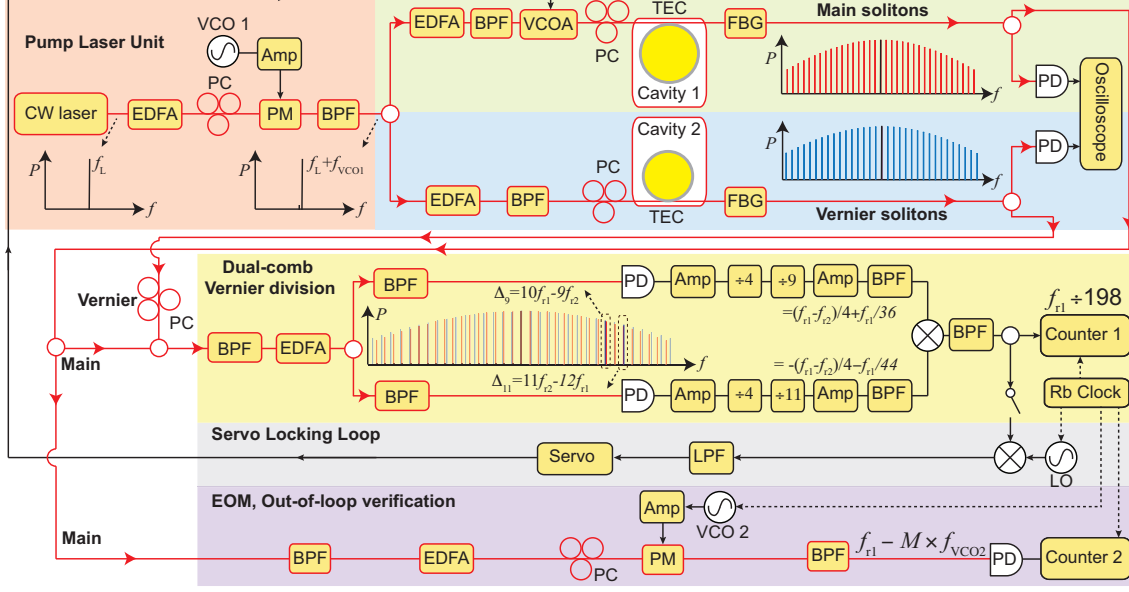
Figure 4.5: **Experimental setup for the Vernier frequency division experiment.** The main solitons and Vernier solitons are generated in two SiN resonators which are temperature controlled by thermoelectric coolers (TECs). The pump laser is the first modulation sideband of a phase modulated (PM) continuous wave (cw) laser, and the sideband frequency can be rapidly tuned by a voltage controlled oscillator (VCO) [72]. The frequencies of the cw laser and phase modulation are f_L and f_{VCO1}, respectively. The main and Vernier solitons are combined and then split to two paths, and two optical bandpass filters (BPFs) are used to select the 9-th and the 11-th pairs of comb lines in each path, respectively. Beat notes Δ_9 and Δ_{11} are generated by photodiodes (PDs) and they are electronically divided by 36 and 44, respectively. The sum of the two signals is created by a frequency mixer, and its frequency f_v is recorded on a counter. For stabilizing the rep-rate of main solitons, f_v is mixed with a rubidium-referenced local oscillator (LO) to servo control a voltage controlled optical attenuator (VCOA) for repetition rate tuning. For out-of-loop verification, electro-optics modulation (EOM) method is used and shown in the purple panel. Erbium-doped fiber amplifiers (EDFAs), polarization controllers (PCs), electrical amplifiers (Amps), low pass filters (LPFs) and rubidium (Rb) clock are also used in the experiment.

the minimum input power requirement of our frequency dividers. Both Δ_9 and Δ_{11} are first divided by 4 so that their frequencies are within the frequency bandwidth of the by-9 and by-11 dividers. The output frequencies after division are $\Delta_9/4/9 = 629$ MHz and $\Delta_{11}/4/11 = 366$ MHz, respectively. These two frequencies are then amplified to ~ 7 dBm and are frequency mixed on an RF mixer. An electrical tunable bandpass filter is used to select the sum of $\Delta_9/36$ and $\Delta_{11}/44$ at the mixer output port. According to eq. (4.3), this frequency is equal to $(1/4/9 - 1/4/11)f_{r1} = f_{r1}/198$.

The optical spectra of single soliton states for main (red) and Vernier (blue) resonators are shown in Fig. 4.6**a**. A zoomed-in panel shows the optical spectra where the frequency of the N-th Vernier soliton comb line coarsely aligns with that of the $(N + 1)$-th main soliton comb line. An electrical spectrum of the beat frequencies between the two combs is shown in Fig. 4.6**b**. Within the 26 GHz cut-off frequency of our electrical spectrum analyzer (ESA), four beat frequencies are observed: $\Delta_1 = 19.3639$ GHz, $\Delta_9 = 22.6815$ GHz, $\Delta_{10} = 3.3157$ GHz and $\Delta_{11} = 16.0449$ GHz. The strong VCO_1 beat note near 14 GHz is derived from the modulation of the cw laser, and can be removed by an optical or electrical filter.

Beat frequencies Δ_9 and Δ_{11} are selected for the main soliton rep-rate division. $\Delta_9(\Delta_{11})$ is the beat frequency between the 9 (11)-th Vernier soliton comb line and the 10 (12)-th main soliton comb line, where $\Delta_9 = 10f_{r1} - 9f_{r2}$, and $\Delta_{11} = 11f_{r2} - 12f_{r1}$. In the measurement, to avoid photodiodes being saturated by the comb lines not associated with Δ_9 and Δ_{11}, an optical bandpass filter is used to pass only comb lines between Δ_9 and Δ_{11}. These comb lines are then amplified by EDFAs and are photodetected to create beat note Δ_9 and Δ_{11} (see Fig. 4.5). In the measurement, after combining the main and Vernier solitons with a fiber coupler, a bandpass filter is used to pass the comb lines associated with Δ_9, Δ_{10}, and Δ_{11} for optical amplifi-

cation. Then a second fiber coupler splits the power into two optical paths, where in each path a bandpass filter is used to select the comb lines of Δ_9 or Δ_{11}, and the corresponding beat note is created on a photodiode. To divide the main soliton rep-rate, Δ_9 and Δ_{11} are divided by 36 and 44 in frequency, respectively, and sent to a RF mixer to produce their sum frequency, $f_v = \Delta_9/36 + \Delta_{11}/44 = f_{r1}/198$, which is the main soliton repetition rate divided by 198. The electrical spectra of $\Delta_9/36$, $\Delta_{11}/44$ and their sum f_v are shown in Fig. 4.6**c,d,e**. The complete experimental setup is shown in Fig. 4.5. More experimental details are included in Methods section. In principle, one can use the configuration in Fig. 4.4, where Δ_1 is mixed with Δ_N/N to generate f_{r1}/N. However, limited by the selection of electrical mixers in our lab, we do not have the capability to mix Δ_1 (~ 20 GHz) and Δ_N/N (~ 2 GHz for $N = 9, 11$), and thus we select Δ_9 and Δ_{11} instead.

To validate the Vernier method, a conventional method by using electro-optics modulation (EOM) frequency comb is implemented as an out-of-loop verification. In the conventional EOM method, two adjacent comb lines from the main solitons are phase modulated at the frequency of a VCO to produce modulation sidebands. The strong modulation results in a pair of sidebands near the midpoint of the two comb lines, and they can be optically filtered and detected [79, 78] (see Fig. 4.5, and Methods section: electro-optics modulation (EOM) comb method). The detected EOM beat note (Fig. 4.6**f**) has frequency of $f_e = f_{r1} - M \times f_{VCO2}$, where M is the number of modulation sidebands, and f_{VCO2} is the modulation frequency. M and f_{VCO2} are set to 11 and 17.897 GHz in this experiment, respectively. It is worth noting that the Vernier beat note f_v has much narrower linewidth than the EOM beat note f_e, which implies that the rep-rate of the main solitons is coherently divided down from 196.974 GHz to 994.82 MHz. It should be noted that $\Delta_9(\Delta_{11})$ are selected as their
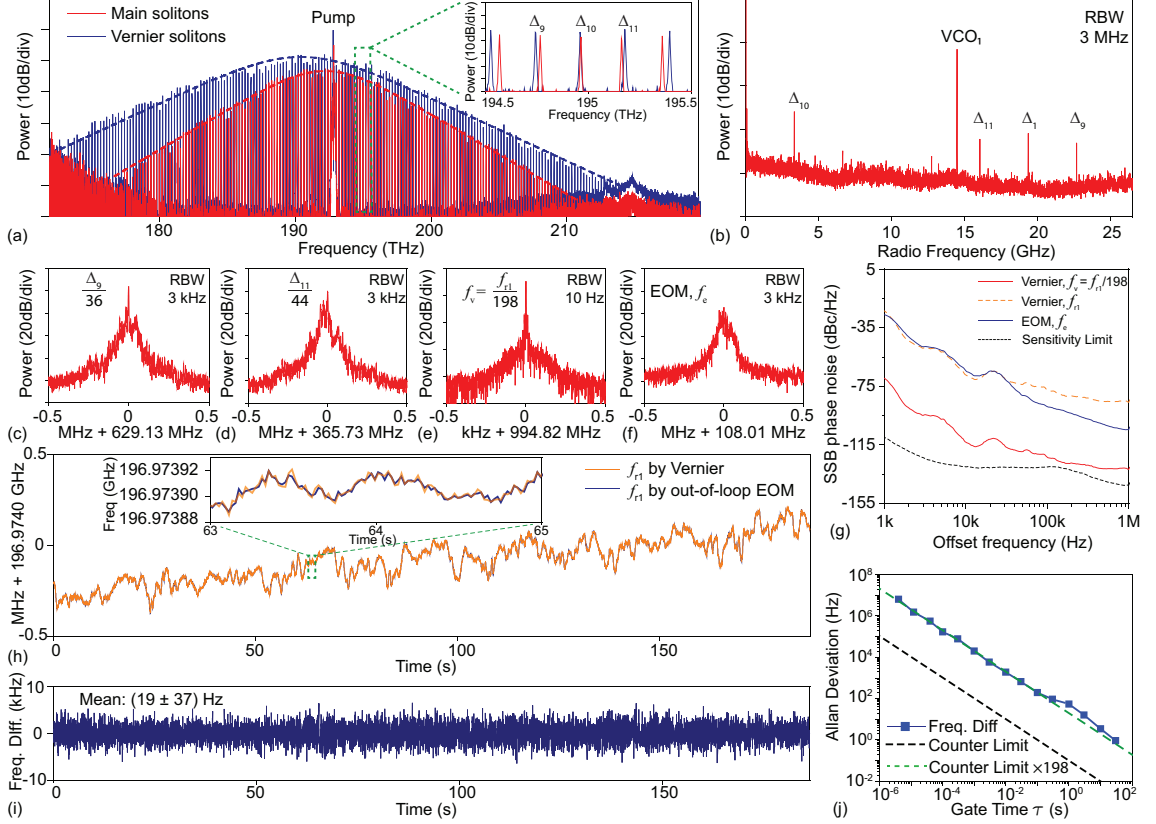
Figure 4.6: (a) Optical spectra of main solitons (red) and Vernier solitons (blue) with sech^2 envelopes (dashed lines). The 9-th and 11-th pairs of comb lines are shown in the zoomed-in panel. The pump laser is suppressed by Bragg-grating filters. (b) ESA spectra of dual-comb beat notes. Δ_1, Δ_9, Δ_{10}, and Δ_{11} are apparent. The strong VCO$_1$ beat note is derived from the pump laser unit, and can be filtered out optically or electronically. ESA spectrum of: (c) Δ_9 divided by 36, (d) Δ_{11} divided by 44, (e) $f_\mathrm{v} = f_{\mathrm{r}1}/198$ as the sum of $\Delta_9/36$ and $\Delta_{11}/44$, and (f) beat note f_e from out-of-loop EOM method. (g) Phase noise measurement of f_v (red) and f_e (blue). The phase noise of f_v multiplied by 198^2 matches that of $f_{\mathrm{r}1}$ measured by out-of-loop EOM method. (h) Rep-rate of the main solitons measured by Vernier method (orange) and EOM method (blue). Both main and Vernier solitons are free-running. The gate time is 10 ms. (i) The frequency difference between rep-rate measured with Vernier and EOM methods in panel (h). Mean value is concluded with a 95% confidence interval under normal distribution. (j) Allan Deviation of the frequency difference. The frequency difference agrees with the counter resolution limit for the Vernier method.

frequencies are relatively close and are compatible with the available RF mixer in our lab.

To show the coherent division in the Vernier dual-comb method, the phase noise of the Vernier beat note, f_v, and the out-of-loop EOM beat note, f_e, are measured with an ESA through direct detection technique (Fig. 4.6**g**). For coherent frequency division, the phase noise of f_v (red trace) should be 198^2 lower than the phase noise of the undivided rep-rate, which is measured through the EOM method (blue trace). This is verified in our measurement, as the phase noise of f_v multiplied by 198^2 (orange dash trace) agrees very well with the phase noise of f_e at offset frequency up to 30 kHz. Beyond 30 kHz offset frequency, the phase noise of f_v is comparable to the ESA sensitivity limit (black dash trace). At high offset frequency, our phase noise measurement might be affected by relative intensity noise (RIN). This is common for direct detection technique, as the RIN cannot be separated from the phase noise in the measurement.

The rep-rate of the main solitons can be derived by multiplying the Vernier beat note, f_v, by 198. A zero-dead-time frequency counter is used to record f_v. The main soliton rep-rate, $f_{r1} = 198 \times f_v$, is shown in Fig. 4.6**h** (orange trace). The free-running main solitons have repetition rate around 196.9740 GHz, and the rate is drifting due to temperature and pump laser frequency fluctuations. This rep-rate measurement is compared to the rep-rate measured with out-of-loop EOM method. The frequency of the EOM beat note f_e is recorded on a second zero-dead-time counter, and the rep-rate is derived as $f_{r1} = f_e + M \times f_{VCO2}$. The EOM-measured rep-rate is shown in Fig. 4.6**h** (blue trace), and it overlaps with the rep-rate measured by Vernier method perfectly. The frequency difference between the Vernier-measured rep-rate and EOM-measured rep-rate is calculated and shown in Fig. 4.6**i**, and it has a mean value of (19

$\pm$ 37) Hz with a 95% confidence interval under normal distribution. Figure 4.6**j** shows the Allan deviation of this frequency difference at various gate times, and it agrees with the counter resolution limit at the frequency of f_v (dash black trace) multiplied by 198 (green dash trace), which is the counter limit for $f_\text{r1} = 198 \times f_\text{v}$. This indicates that no frequency difference between the Vernier method and the EOM method can be detected within the sensitivity of our instruments. In all frequency measurements, the counters and VCOs are synchronized to a rubidium clock.

4.5 Phase-locking the repetition rate

The main soliton repetition rate can be stabilized by locking the Vernier beat note f_v to a radio-frequency reference. In this demonstration, f_v is locked to a rubidium-stabilized local oscillator through servo control of the pump power using an voltage-controlled optical attenuator (VCOA) to vary the main soliton repetition rate (see Fig. 4.5). Rep-rate measurement with the EOM method is utilized to verify the locking and the result is shown in Fig. 4.7**a**. To eliminate the relative frequency drifts of the electronic components, f_VCO1, f_VCO2, counter 1 and counter 2 are all synchronized to the same rubidium clock. Therefore, the error in the rubidium clock has been corrected, and the absolute stability of the reference will not affect our frequency readouts. We are characterizing the residual stability of our rep-rate, and the absolute stability of the reference will not affect our frequency readouts. This allows us to evaluate the servo locking loop without using high performance atomic clock reference. The locking is turned on at the time near 50 s, and the soliton rep-rate immediately stops drifting and is stabilized to 196,962,681,959 Hz (see Fig. 4.7**a**). The Allan deviations of the free-running (red) and stabilized (green) rep-rate

are calculated from the EOM-based rep-rate measurements and are presented in Fig. 4.7**b**. Above 0.3 ms gate time, the Allan deviation of the locked rep-rate scales as $1/\tau$, where τ is the gate time. Below 0.3 ms gate time, the Allan deviation of the rep-rate follows that of the free-running rep-rate. This behavior of the Allan deviation is expected for a phase-locked oscillator with $\sim$ kHz locking bandwidth. In general, to improve the residual Allan deviation for a phase-locked oscillator, one can (1) increase the servo bandwidth and (2) improve the overall system stability and thus the Allan deviation beyond the servo bandwidth. The first one can be accomplished by fast feedback control of the resonator temperature and thus the soliton rep-rate through an integrated heater on chip [74], and the latter one can be achieved by improving the temperature and mechanical stability of the system through packaging [89]. Ultimately, the absolute stability of the rep-rate is limited by the atomic clock reference. It is worth noting that the repetition rate of the Vernier solitons is not stabilized in the entire measurement.

4.6 Summary

In this chapter, We have introduced the dual-microresonator solitons generation method, the conventional EOM method and the Vernier division method for repetition rate detection. We demonstrated the Vernier frequency division method to detect and stabilize soliton repetition rate at 197 GHz with 20s GHz bandwidth photodiodes and electronics. The Vernier method shall be applicable for a wide range of repetition frequencies spanning from GHz to THz. For low repetition rate combs, our method can further reduce the required electrical bandwidth, and is only limited by the optical and electrical filtering capability to select the desired dual-comb beat
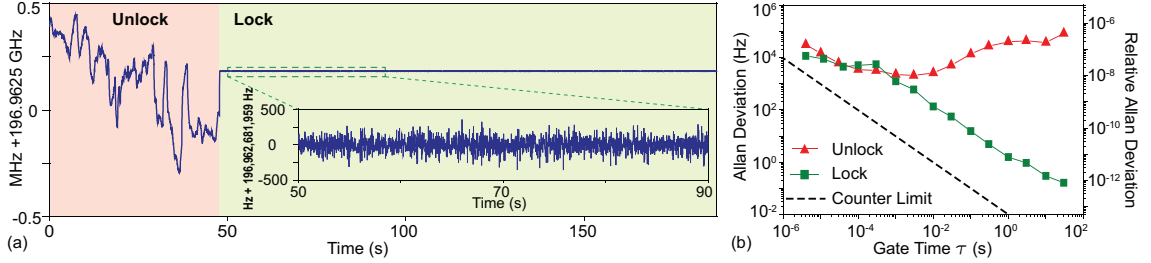
Figure 4.7: **Stabilization of main soliton repetition rate by using Vernier dual-comb method.** The rep-rate of the main solitons is stabilized by locking f_v to a Rb-referenced oscillator, and the locking is verified by using EOM method. **(a)** Rep-rate measurement using EOM method. The locking loop is engaged at the time near 50 s. The gate time (τ) is 10 ms. **(b)** Allan deviation calculated from the unlocked and locked repetition rates that are measured with the EOM method. The locking loop has $\sim$ kHz servo bandwidth. Within the servo bandwidth, the Allan deviation goes down as $1/\tau$. Beyond the servo bandwidth, the Allan deviation is similar to that of the free-running unlock rep-rate. The error in the rubidium clock has been corrected for the Allan deviation of the locked rep-rate. This is done by synchronizing the EOM and the soliton rep-rate to the same rubidium reference. In the entire measurement, the repetition rate of the Vernier solitons is not stabilized, and there is no feedback control of the laser-cavity detuning for the Vernier solitons.

frequencies. For a fixed electrical bandwidth and rep-rate difference, higher main soliton rep-rate will demand a broader comb span in the Vernier method. This is because the number of comb lines required for the comb line frequency of Vernier soliton to overtake that of the main soliton increases linearly with the main soliton repetition rate. At 1 THz repetition rate, 50 comb lines on one side of the pump is needed for 20 GHz rep-rate difference between main and Vernier solitons, and this comb span has been reported previously [66, 67].

It also applies to the case where the two frequency combs do not share the same pump frequency/center frequency. In this situation, one more pair of beat frequency should be detected. As this additional beat note and the two Vernier beat notes share the same offset frequency between the two pump lasers, the offset frequency can be eliminated by frequency subtraction. This will enable the Vernier method to be applied to

other types of high-rate combs, such as mode-locked semiconductor lasers [90]. The concept of Vernier dual combs could also be modified to assist carrier-envelope offset frequency (f_{CEO}) detection for self-referencing an octave-spanning microcomb. At 1 THz rep-rate, the f_{CEO} given by the f-$2f$ signal can range from 0 to 500 GHz, and it is challenging to keep this frequency in a detectable range as it is subject to small fabrication variations. However, if a Vernier comb is frequency doubled and beat against the main comb, a series of f-$2f$ beat frequencies can be created. Their spacing equals to the dual-comb rep-rate difference, and this can bring the f-$2f$ signal to a detectable frequency. Finally, the Vernier method has the potential to revolutionize optical and electrical frequency conversion by eliminating the need for a detectable repetition rate frequency comb, and it will have direct applications in optical clock [91], optical frequency division [92], and microwave frequency synthesis [70].

Chapter 5

Radio-frequency line-by-line Fourier synthesis

5.1 Introduction

Fourier analysis creates one-to-one mapping between the temporal and frequency profiles of a waveform. Arbitrary temporal waveforms can be generated through Fourier synthesis by manipulating the amplitude and phase in the spectrum domain. Optical spectral waveshaping, or optical line-by-line waveshaping, has been widely applied to optical arbitrary waveform generation [93, 94] (AWG), coherent control of quantum processes [95, 96, 97], and optical communications[98]. The broad optical bandwidth provides femtosecond temporal resolution in the Fourier synthesis[99] that is not attainable by conventional electronics.

Fourier synthesis in optical domain can be down-converted to microwave and mmWave frequencies [100, 101, 102, 103, 104, 105] through coherent dual-comb sampling method[106], and it could have wide applications in wireless communications, radar systems, and electronic testing[107, 108, 109].

When photomixing two optical frequency combs with different repetition rates on a photodiode, an RF frequency comb will be created, with its comb lines deriving

their amplitudes and phases from the dual optical combs. Line-by-line amplitude and phase control on optical frequency combs [110] can then be coherently mapped to the RF frequency comb for waveform synthesis, which has been shown recently with electro-optic frequency combs[100, 101, 102, 103, 104, 105]. Compared with other existing photonic methods for RF waveform generation[111, 112, 113, 114, 115, 116], which rely on optical delay structures to either provide enough dispersion for far-field frequency-to-time mapping, or route different replicas of a low repetition rate optical pulse to different arrival times on a photodiode, the Fourier synthesis method eliminates the need for long tunable optical delay lines and low repetition rate mode-locked lasers, and thus creates the potential for mass-scale integration on a photonic chip.

In this chapter, we demonstrate RF spectral line-by-line waveshaping and Fourier synthesis of RF waveforms by using optical dual-microresonator solitons [9, 79, 13, 10]. The high repetition rate of soliton microresonator-based frequency combs (microcombs) [10] enables line-by-line amplitude and phase control of individual optical comb lines [110]. Dual-comb coherent sampling is then used to coherently down-convert the waveshaped optical microcomb to RF frequencies by beating it with another soliton microcomb on a fast photodiode. A complete discrete Fourier series can be constructed for waveform synthesis by nullifying the carrier envelope offset frequency in the down-converted RF frequency comb. A series of temporal waveforms, including: tunable Gaussian, triangle, square, and "UVA"-like logo, are demonstrated to illustrate arbitrary waveform synthesis. All critical components in the dual-microcomb method, including soliton microcombs [10], wavelength multiplexer/demultiplexer[117], intensity and phase modulators [118], optical amplifier [119], and ultrafast photodiodes [120], are compatible with photonic integration. A discus-

sion of waveform quality and a comparison of the effective number of bits (ENOB) with electronic AWG are presented at the end of the manuscript.

5.2 Concept of line-by-line Fourier synthesis

The concept of dual-microcomb RF line-by-line waveshaping is illustrated in Fig. 5.1. Signal solitons with repetition rate of f_r, and local solitons with repetition rate of $f_r + \Delta f_r$, are generated in two Kerr microresonators pumped by the same laser [21, 121]. A radio-frequency (RF) comb with zero offset frequency and a comb spacing of Δf_r can be created by beating the signal and local solitons on a fast photodiode. The RF comb forms a Fourier series, with $V(t) = \sum_{n=0}^{\infty} A_n \cos\left(2\pi n\Delta f_r t + \varphi_n\right)$, where $V(t)$ is the voltage output of the photodiode, n is the comb line number, A_n and φ_n are the amplitude and phase of n-th comb line, respectively. As the amplitude and phase of the RF comb lines are fully derived from the amplitude and phase of the corresponding optical comb lines, the line-by-line optical waveshaping on the signal solitons can fully control the amplitude and phase of the RF comb. In principle, dynamic waveform synthesis is possible by using time varying modulations of A_n and φ_n through the use of electro-optic modulators. Here, an off-the-shelf optical waveshaper is used instead to demonstrate static, repetitive waveform synthesis.
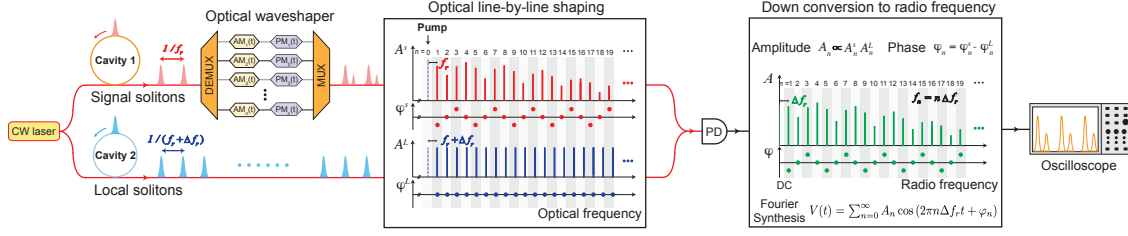
Figure 5.1: **Concept of RF line-by-line Fourier synthesis with dual-microresonator solitons.** A radio-frequency (RF) comb that is composed of a series of equidistant RF lines is created by photomixing two soliton microcombs with slightly different repetition frequencies on a photodiode (PD). The RF comb spacing is set by the repetition rate difference of the two soliton microcombs, and the RF comb offset frequency is nullified by using a common pump laser to drive both optical solitons. To implement line-by-line amplitude (A_n) and phase (φ_n) control of the RF comb lines, one of the optical microcomb (signal solitons) goes through optical line-by-line waveshaping, and optical amplitude modulations (AMs) and phase modulations (PMs) are down-converted to the RF frequency comb through dual-microcomb coherent sampling. As the RF frequency comb forms a complete Fourier series, arbitrary temporal waveforms can be synthesized.

5.3 Demonstration of an arbitrary RF waveform generator with Fourier synthesis

For Fourier synthesis of arbitrary RF waveforms, the signal and local solitons are generated in SiN micro-ring resonators[88] with intrinsic quality factors of 7.7×10^6 and 4.3×10^6, respectively. The radii of the signal and local soliton resonators are set to 228.65 μm and 228.30 μm, respectively, which introduces a 150 MHz repetition rate offset (Δf_r) between the two solitons. To create an RF comb with zero offset frequency, both optical solitons are generated using the same pump laser[21, 121]. Thermoelectric coolers (TECs) are placed beneath microresonators to coarsely align the resonance frequencies of the two resonators at the pump laser wavelength. The thermal tuning of the resonant frequency is ~2.5 GHz/°C, and the TEC has a resolution of 0.01°C. A rapid laser frequency scanning method that leverages the

single-sideband suppressed-carrier (SSB-SC) modulator[72] is used to generate single soliton states in both resonators simultaneously[121]. The pump frequency is controlled by the voltage-controlled oscillator (VCO) that drives the SSB-SC modulator, which scans over ∼3 GHz in 150 ns from shorter to longer wavelength. Fig. 5.2**a** illustrates the simplified experimental setup. The optical spectra of signal (red) and local (blue) solitons are shown in Fig. 5.2**b**. No active locking technique is used in our experiments for stabilization..

An optical line-by-line waveshaper[110] is used to control the phase of each comb line in the signal solitons (φ_n^S). The signal and local solitons are then combined in a fiber coupler, and a second waveshaper is followed to control the amplitudes of each comb line pair (A_n^S, A_n^L). An erbium-doped fiber amplifier (EDFA) is used to amplify the solitons, and a high-speed, high-power photodiode converts the optical dual solitons into a zero offset RF frequency comb. The dual-comb optical spectrum after EDFA is measured on an optical spectrum analyzer, and an oscilloscope with 4 GHz bandwidth is used to characterize the RF temporal waveform, the spectrum of the RF comb, and the phase of the RF comb. Fig. 5.2 c presents the measurements when no phase or power adjustment are added by the waveshapers, except compensating the dispersion introduced by optical fibers. This can serve as a reference point for line-by-line waveshaping in the RF domain. In our experiment, we purposely select a small RF comb spacing, $\Delta f_r = 150$ MHz, such that the analog bandwidth of the RF comb will not exceed the 4 GHz bandwidth limit of our oscilloscope. The analog bandwidth in our experiment is limited by the oscilloscope, not by the Nyquist frequency of coherent dual-comb sampling method[106] or the speed of the photodiode.

To illustrate line-by-line waveshaping in the RF domain, four types of Gaussian based temporal waveforms are demonstrated in Fig.5.2 d to Fig.5.2 g. The fundamental
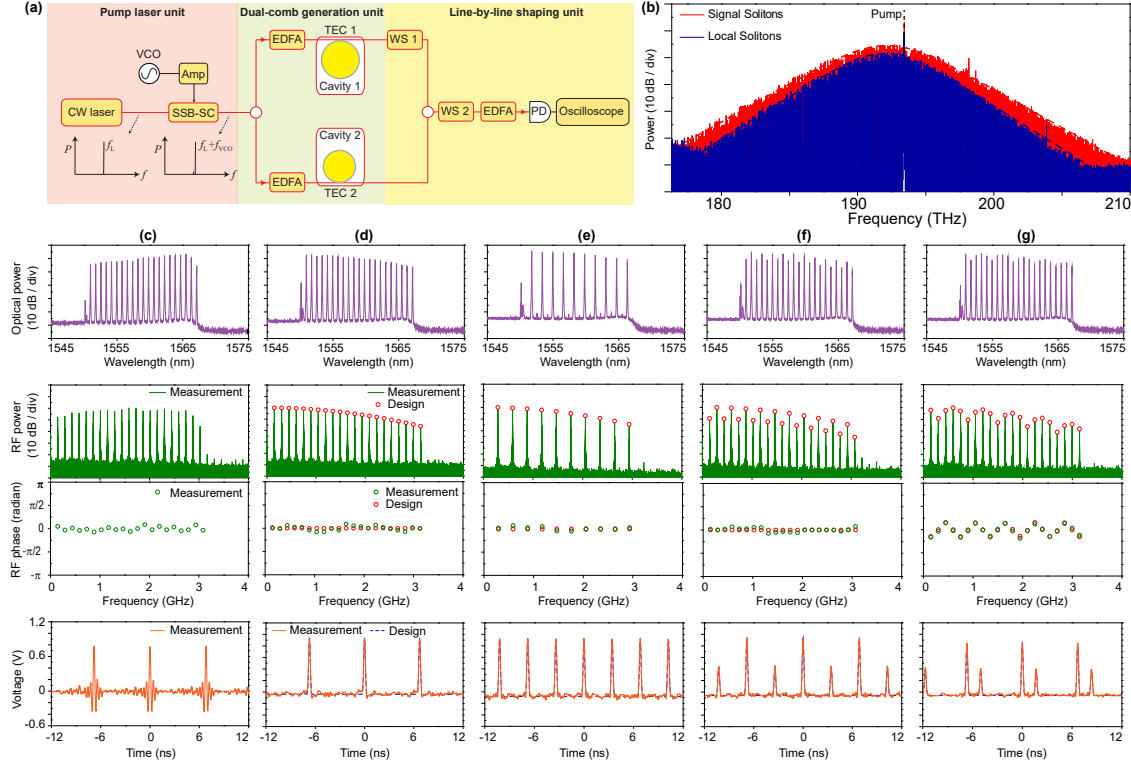
Figure 5.2: **Line-by-line waveshaping of RF Gaussian waveforms.** (a) Simplified experimental setup. The pump laser frequency is derived from the frequency of a continuous-wave (cw) laser, f_L, and the voltage-controlled oscillator (VCO), f_{VCO}. (b) Optical spectra of the signal (red) and local (blue) microresonator solitons. Sech^2 envelope fittings are shown in dash lines. The waveform synthesis is shown in panel (c) to (g) to illustrate the line-by-line control of amplitude and phase of the RF comb. (c) The reference dual-microcomb waveforms with only dispersion compensation. (d) Amplitude control of the RF comb lines to shape temporal waveforms into Gaussian pulses with 235 ps pulse width. (e) Further amplitude control to add an equidistant Gaussian pulse and double the RF comb repetition frequency. (f) Adjust the relative Gaussian amplitudes through comb line amplitude control. (g) Combined amplitude and phase control of the RF comb to tune the relative position of the two Gaussian pulses. From the top to bottom rows are: (i) the optical spectra of soliton dual-microcomb after waveshaping, (ii) the down-converted RF spectra, (iii) the phase of RF comb lines, and (iv) the temporal waveforms. Designed comb line powers and phases are shown in red circles, and the designed temporal waveforms are shown in dashed blue lines.
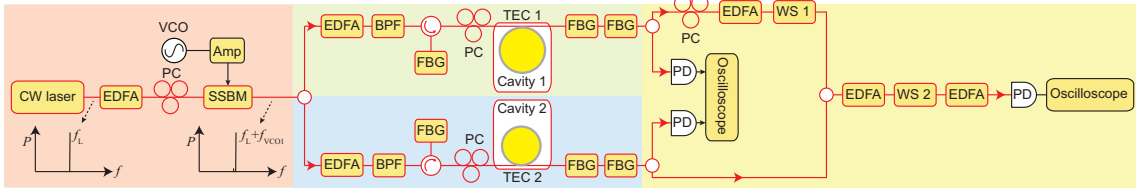
Figure 5.3: **Complete experimental setup for radio-frequency line-by-line Fourier synthesis.** A rapid laser frequency scanning method is realized by the single-sideband modulator (SSBM) that is driven by a voltage controlled oscillator (VCO). The modulated pump then goes through a 50/50 splitter and splits into the signal resonator and local resonator paths. In each path, the pump goes through an erbium doped fiber amplifer (EDFA), a band pass filter (BPF), a fiber bragg grating (FBG) and a polarization controller before it couples into the cavity. The BPF and FBG are for suppressing the amplified spontaneous emission (ASE) noise from the EDFA. Two FBGs after the cavity are for separating the pump and comb with a combined rejection ratio of about 30 dB. Waveshaper (WS) 1 and 2 are for phase and amplitude control respectively. A photodiode (PD) is used to convert the optical frequencies to rf frequencies.

Gaussian waveform is shown in Fig.5.2 d, which has a Gaussian envelope with flat phase in both frequency and temporal domains. The power and phase of the generated RF comb match the designed ones very well, which are shown in red circles. The corresponding temporal waveform is a Gaussian pulse train with a time period of 6.71 ns, peak voltage of 0.94 Volt, and pulse width of 235 ps. No electrical amplifier after the photodiode is used in this work. The number of pulses in one period can be doubled by knocking out half of the RF comb lines (Fig.5.2 e). This is equivalent to adding an equidistant Gaussian pulse with the same amplitude in one temporal period. The amplitude of the added Gaussian pulse can be adjusted by changing the amplitude of the RF comb (Fig.5.2 f). Finally, the temporal position of the added Gaussian pulse can be shifted by modifying both the amplitude and the phase of the RF comb lines (Fig. 5.2 g). The demonstration of these four Gaussian waveforms illustrates the full control of amplitude and phase in our RF line-by-line shaping method.
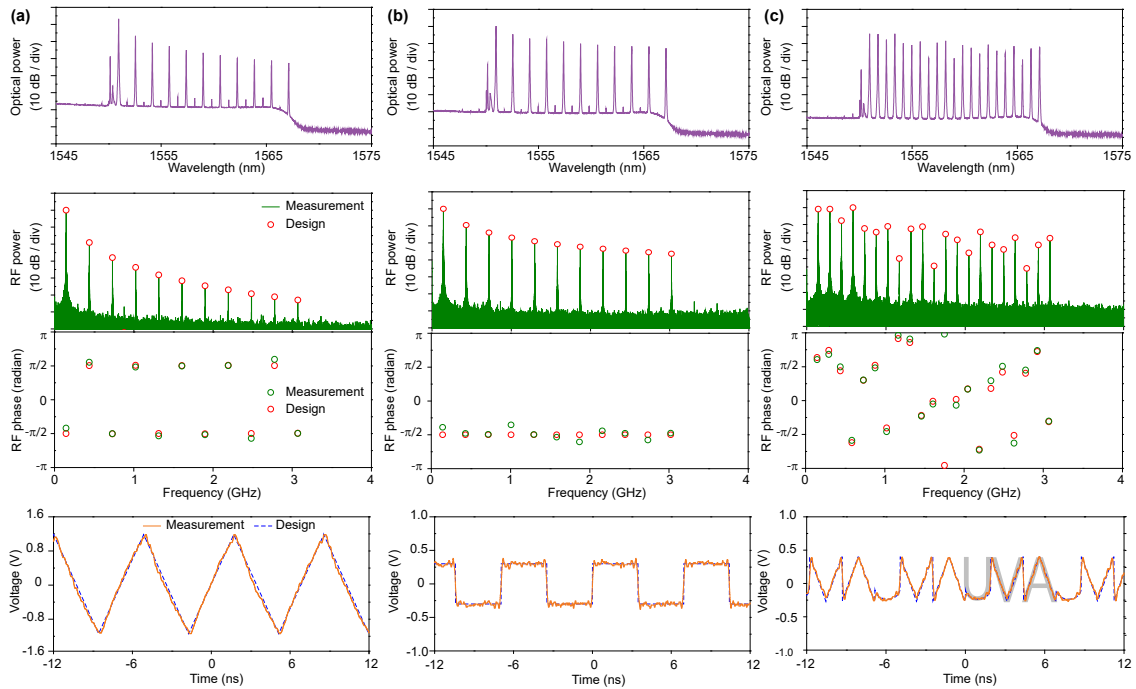
Figure 5.4: **Arbitrary waveform generation by using dual-microcomb RF Fourier synthesis.** (a) Triangle waveform. (b) Square waveform. (c) "UVA"-like waveform. The corresponding (i) optical spectra, (ii) RF spectra, (iii) comb line phases, and (iv) temporal waveforms are shown from top to bottom in each panel. Designed comb line powers and phases are shown in red circles, and the designed temporal waveforms are shown in dashed blue lines.

One direct application of line-by-line waveshaping is arbitrary waveform generation. Three representative waveforms, including triangle, square, and "UVA"-like waveforms, are demonstrated here. For each temporal waveform, the corresponding amplitude and phase of each comb line can be derived by discrete Fourier transform of the temporal waveform. The Fourier transform of the triangle waveform is $x_{tr}(t) = \sum_{j=1}^{\infty} n^{-2} \cos\left(2\pi n\Delta f_r t + (-1)^j \pi/2\right)$, where j is integer number, and $n = 2j + 1$. The triangle waveform only has comb lines with odd number n, where the phase of the comb line alternates between $-\pi/2$ and $\pi/2$, and the amplitude decays quadratically with the line number n. These features are well reproduced in the power and phase spectra (Fig.5.4 a), and a triangle wave with period of 6.84 ns and 2.4 V peak to peak voltage is generated. Similarly, the square waveform is composed of comb lines with odd number: $x_{sq}(t) = \sum_{j=1}^{\infty} n^{-1} \cos\left(2\pi n\Delta f_r t - \pi/2\right)$. Fig.5.4 b shows the measurements of the square waveform. Finally, a "UVA"-shaped waveform is shown in Fig.5.4 c to illustrate that the waveform construction in our method is arbitrary. All three demonstrated waveforms agree very well with the designed waveforms.

5.4 Arbitrary RF waveform repetition period tuning

As the RF waveform repetition period is set by the repetition rate difference between the signal and local solitons, it can be tuned directly by adjusting the repetition rate of one of the solitons. Small range tuning of repetition period can be achieved by adjusting the temperature of the local soliton microresonator. Fig.5.5 a presents the RF comb repetition rate versus the temperature of the local soliton microresonator and a tuning rate of ~ 30 MHz/°C is measured. The spectra and temporal profiles

58
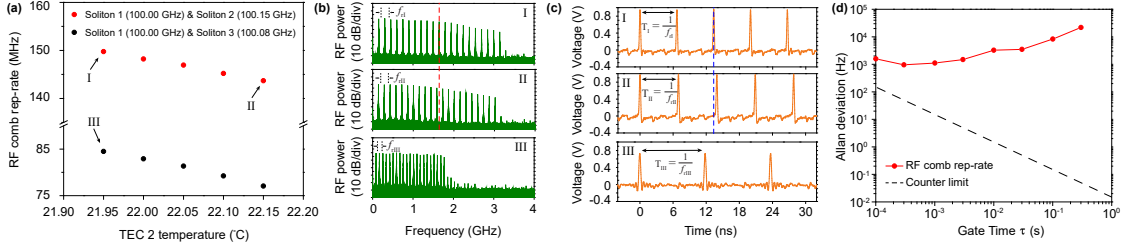
Figure 5.5: **Tuning the repetition frequency of the RF comb and temporal waveforms.** (a) The RF comb repetition frequency is tuned by adjusting the rep-rate of local solitons. Small range tuning is realized by tuning the temperature of the local soliton microresonator with a thermoelectric cooler (TEC). Large range tuning is accomplished by generating local solitons in a microresonator with a slightly different radius. Soliton repetition rates are indicated in the figure legend. Panel (b) and panel (c) show the electrical spectra and corresponding temporal waveforms at three different operating points indicated in panel (a). (d) Allan deviation of RF comb repetition rate at point I in panel (a).

of two Gaussian waveforms at (I) 21.95 °C and (II) 22.15 °C are shown in Fig.5.5 b and Fig.5.5 c, where a difference of 0.29 ns in the waveform repetition periods can be seen. Large change of waveform period can be achieved by generating local solitons in a microresonator with slightly different radius. The RF comb rep-rate changes from $\sim$ 150 MHz to $\sim$ 85 MHz when the radius of local soliton microresonator is varied from 228.30 μm to 228.53 μm. Finally, Fig.5.5 d presents the Allan deviation of the RF-comb repetition rate, which is subject to the pump laser frequency drift and environment temperature fluctuations in our free running system.

5.5   Resolution of the RF waveforms

5.5.1   Effective number of bits (ENOB)

An important figure of merit for RF arbitrary waveform generation is the effective number of bits (ENOB) [122], which can be used to evaluate the waveform quality

or the effective resolution of the waveforms. For our dual-comb AWG method, the fundamental limit of its ENOB is set by the optical power of the frequency combs. The fundamental limit of the ENOB in the dual-comb AWG method can be calculated using the ratio of signal voltage to the root-mean-square noise voltage fluctuations, and it is defined as: $2^{\text{ENOB}} = V_p/\sqrt{2}V_\sigma$, where V_p is the time domain peak voltage, and V_σ^2 is the voltage noise variance. As harmonic distortion is not observed in our experiments, it is not included in our ENOB calculation. The digital quantization noise is not included either for our analog system. It should be noted that the widely used ENOB expression for sinusoidal waveforms [122] agrees with our definition when excluding harmonic distortion and digital quantization noise.

The optical field of an N-pair dual-comb can be expressed as:

$$E = \sum_{n=1}^{N} \sqrt{P_n^S} \exp[-i(w_n^S t - \varphi_n^S)] + \sum_{n=1}^{N} \sqrt{P_n^L} \exp[-i(w_n^L t - \varphi_n^L)], \qquad (5.1)$$

where $\omega_n^{S,L}$, $P_n^{S,L}$ and $\varphi_n^{S,L}$ are the n-th comb line's frequency, power, and phase of the signal (S) and local (L) combs. The photocurrent generated at the photodiode can be expressed as:

$$
\begin{aligned}
I_{ph} &= R|E|^2 + \Delta I_S + \Delta I_T \\
&= R\sum_{n=1}^{N}(P_n^S + P_n^L) + 2R\sum_{n=1}^{N} \sqrt{P_n^S P_n^L} \cos[2\pi n\Delta f_r t + (\varphi_n^S - \varphi_n^L)] + \Delta I_S \qquad (5.2) \\
&\quad + \Delta I_T + \cdots,
\end{aligned}
$$

where R is the responsivity of the photodiode, and $2\pi n\Delta f_r = \omega_n^L - \omega_n^S$ are the frequency differences of n-th lines of signal combs and local combs. ΔI_S and ΔI_T are

the current fluctuations caused by the shot noise and thermal noise, respectively. In our experiments, the dark current noise can be neglected (10 nA for our PD, Finisar VPDV2120). The first term in the second line corresponds to the DC photocurrent, and the second term corresponds to the AC photocurrent for the down-converted RF comb. Higher frequency terms beyond the Nyquist bandwidth [106], such as harmonics of comb repetition frequency, are neglected. For analysis of signal-to-noise ratio (SNR) and effective number of bit (ENOB) [122], we assume a flat spectrum for the dual-comb for simplicity, i.e., $P_n^S = P_n^L = P_0$. The AC voltage output is then given by:

$$V_{AC} = 2R_{load} \cdot RP_0 \sum_{n=1}^{N} \cos[2\pi n \Delta f_r t + (\varphi_n^S - \varphi_n^L)], \tag{5.3}$$

where R_{load} (50 Ω) is the load resistor. For the sinc-shaped waveform, we will have $\varphi_n^S = \varphi_n^L$, and the peak voltage will occur when $t = M/\Delta f_r$, where M is an integer number. The peak voltage can be expressed as:

$$V_p = 2R_{load} \cdot R \cdot NP_0. \tag{5.4}$$

The variances from shot noise and thermal noise, and their total variance are given by:

$$\sigma_S^2 = 2e \cdot I_{DC} \cdot f_{\text{BW}}, \tag{5.5}$$

$$\sigma_T^2 = k_B T / R_{load} \cdot f_{\text{BW}}, \tag{5.6}$$

$$\sigma^2 = \sigma_S^2 + \sigma_T^2, \tag{5.7}$$

where e is the charge of an electron, $I_{DC} = 2R \cdot NP_0$ is DC photocurrent, f_{BW} is the bandwidth of photodiode (or the total bandwidth, assuming photodiode bandwidth is equal to or larger than the Nyquist bandwidth), k_B is the Boltzmann constant, and T is the temperature (300 K in the lab enviroment).

The effective number of bits (ENOB) of the demonstrated waveform can be calculated using the ratio of signal voltage to the root-mean-square noise voltage fluctuations [122]:

$$\frac{V_p/\sqrt{2}}{V_\sigma} = 2^{\text{ENOB}} \Leftrightarrow \text{ENOB} = \log_2\left(\frac{V_p/\sqrt{2}}{R_{load} \cdot \sigma}\right), \tag{5.8}$$

where we have used $V_\sigma = R_{load} \cdot \sigma$. By inserting equations (5.4 - 5.6) to equation (5.8), the expression of ENOB is given by:

$$\text{ENOB} = \frac{1}{2}\log_2\left[\frac{2R^2 \cdot N^2 P_0^2}{\sigma^2}\right] = \frac{1}{2}\log_2\left[\frac{2R^2 \cdot N^2 P_0^2}{(4e \cdot R \cdot NP_0 + k_B T/R_{load}) \cdot f_{\text{BW}}}\right]. \tag{5.9}$$

The ENOB increases with the number of comb pairs N and comb line power P_0, and decreases with electrical bandwidth.

Our definition of ENOB agrees with the common ENOB definition in electronic AWG for sinusoidal waveform, which is given by[122]:

$$\text{ENOB} = \frac{\text{SINAD} - 1.76}{6.02}, \tag{5.10}$$
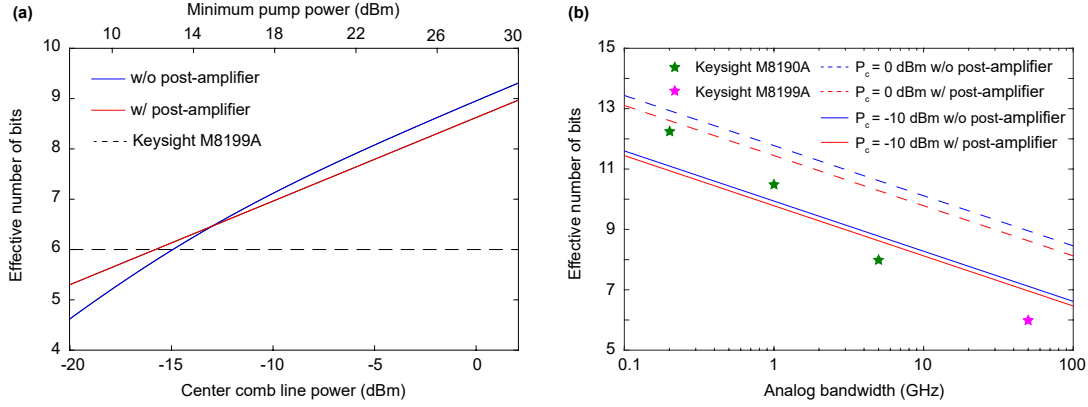
Figure 5.6: **Theoretical analysis of effective number of bits (ENOB).** (a) The theoretical limit of dual-comb AWG ENOB versus the comb line power for 50 GHz analog bandwidth. The minimum pump power required to achieve such comb line power in the single soliton microcomb state is also shown. In this calculation, we assume 3 dB loss between the microresonators and the photodiode, and 4 dB noise figure for the optical post-amplifier. (b) ENOB comparison of dual-comb AWG and state-of-the-art commercial electronic AWG.

where $\text{SINAD} = P_{signal}/(P_{noise} + P_{distortion})$ is the signal-to-noise and distortion ratio, and $1.76/6.02 \approx 0.29$ comes from the quantization error in an ideal digital-to-analog converter (DAC) / analog-to-digital converter (ADC). When exclucding the effect of harmonics distortion and digital quantization error, equation (5.10) becomes:

$$\text{ENOB} = \frac{\text{SNR}}{6.02} = \frac{10 \log_{10}(V_{sig-rms}/V_\sigma)^2}{20 \log_{10} 2} = \log_2(V_{sig-rms}/V_\sigma) = \log_2(V_p/\sqrt{2}V_\sigma),$$

(5.11)

which is the same as our ENOB definition in equation (5.11).

5.5.2 ENOB and soliton microcomb power

For bright dissipative Kerr cavity solitons, the center comb line power can be expressed[9, 62] as a function of cavity second-order dispersion D_2 and external coupling rate κ_{ext}:

$$P_c = \frac{\hbar\omega_0}{4g}\kappa_{ext}D_2 = \frac{\pi n_0 S_{eff}}{2\omega_0 n_2 D_1}\kappa_{ext}D_2, \qquad (5.12)$$

where $g = \hbar\omega_0^2 c n_2/n_0^2 V_{eff}$ is the Kerr nonlinear coefficient and $V_{eff} = 2\pi c S_{eff}/n_0 D_1$ is the effective cavity mode volume. $\hbar$, ω_0, c, n_0, n_2, S_{eff}, D_1 are the plank constant, cavity mode angular frequency, speed of light, refractive index, Kerr nonlinear refractive index, effective mode area and free spectral range, respectively. P_c increases with the product of κ_{ext} and D_2. For a given soliton pulse width τ_s, the minimum pump power for the soliton state is given by [62]:

$$P_{pump,min} = -\frac{2c}{\pi}\frac{S_{eff}\beta_2}{\omega_0 n_2 D_1}\frac{\kappa^2}{\kappa_{ext}}\frac{1}{\tau_s^2} = \frac{2}{\pi}\frac{n_0 S_{eff}}{\omega_0 n_2}\frac{D_2}{D_1^3}\frac{(\kappa_0 + \kappa_{ext})^2}{\kappa_{ext}}\frac{1}{\tau_s^2}, \qquad (5.13)$$

where $\beta_2 = -n_0 D_2/c D_1^2$ is the group velocity dispersion, and κ_0 is the cavity intrinsic loss rate.

Combining eq. (5.12) and eq. (5.13), the center comb line power can be expressed as a function of the minimum pump power:

$$P_c = \left(\frac{\eta\pi D_1\tau_s}{2}\right)^2 P_{pump,min}, \qquad (5.14)$$

where we have used resonator-waveguide coupling strength coefficient $\eta = \kappa_{ext}/(\kappa_0 + \kappa_{ext})$. For the sech^2-shaped soliton microcomb, its comb power spectral envelope is

given by:

$$P(\Delta\omega) = P_c \cdot \text{sech}^2\left(\frac{\pi\tau_s}{2}\Delta\omega\right), \tag{5.15}$$

where $\Delta\omega$ is the comb tooth frequency relative to the comb center frequency. Assuming that within 3-dB spectral bandwidth there are N single-sided comb lines, we can then obtain:

$$\text{sech}^2\left(\frac{\pi\tau_s}{2}ND_1\right) = \frac{1}{2} \Leftrightarrow \frac{\pi D_1 \tau_s}{2} = \frac{0.8814}{N}. \tag{5.16}$$

Therefore, equation (5.14) can be expressed as:

$$P_c = \left(\frac{0.8814\eta}{N}\right)^2 P_{pump,min}, \tag{5.17}$$

In our experiment, these N comb lines can be used for line-by-line Fourier synthesis. For sinc-shaped waveform, the power of each comb line is set to the weakest comb line power, i.e., 3 dB lower than that of the center comb line. Also, considering the total insertion loss of optical components (such as wavelength demultiplexer/multiplexer, phase/intensity modulators) between microresonators and photodiodes, the actual comb line power received by the photodiode can be expressed as:

$$P_0 = \alpha \times \frac{P_c}{2}, \tag{5.18}$$

where α is the efficiency from resonators to detectors. By plugging eqs. (5.17)-(5.18) into equation (5.9), ENOB can be expressed as:

$$\begin{aligned}
\text{ENOB} &= \frac{1}{2}\log_2\left[\frac{R^2 \cdot \alpha^2 N^2 P_c^2}{2(2e \cdot R \cdot \alpha N P_c + k_B T/R_{load}) \cdot f_{\text{BW}}}\right] \\
&= \frac{1}{2}\log_2\left[\frac{(0.8814\eta)^4 \cdot R^2 \cdot \alpha^2 P_{pump,min}^2}{2[2(0.8814\eta)^2 \cdot e \cdot R \cdot \alpha P_{pump,min}/N + k_B T/R_{load}]N^2 \cdot f_{\text{BW}}}\right].
\end{aligned} \tag{5.19}$$

Equation (5.19) is used for plotting ENOB without amplifier in Fig.5.6 (a) and Fig.5.6 (b).

5.5.3 ENOB after optical amplification

If an optical amplifier, i.e. erbium-doped fiber amplifier (EDFA), is placed before the photodiode for amplifying the comb line power, the output optical power per comb line P_{0A} is given by:

$$P_{0A} = P_0 G, \tag{5.20}$$

where G is the gain of the amplifier and we assume it is constant over the entire amplifier bandwidth. The spectral density of amplified spontaneous emission (ASE) noise is given by [123, 124, 125, 126]:

$$S_{ASE} = \frac{1}{2}(F_n G - 1)h\nu, \tag{5.21}$$

where F_n is the amplifier noise figure, h is the Planck constant, and ν is the frequency of input signal. Given that the amplifier bandwidth ($\Delta\nu$) is much smaller than the frequency of light ($\Delta\nu \ll \nu$), the spectral density of ASE noise can be treated as a constant, i.e., $S_{ASE} = 1/2 \times (F_n G - 1)h\nu_0$, where ν_0 is the center frequency of the

amplifier operating band. The total power of ASE noise over the entire amplifier bandwidth $\Delta\nu$ is given by:

$$P_{ASE} = 2 \times S_{ASE} \times \Delta\nu = (F_n G - 1)h\nu_0 \times \Delta\nu, \qquad (5.22)$$

where the factor of 2 includes both orthogonal polarization modes supported in a single-mode fiber. When dividing the ASE bandwidth $\Delta\nu$ into K bins[127, 128, 126] and each bin has a bandwidth of $\delta\nu = \Delta\nu/K$, we can express the optical field of the ASE noise as:

$$E_{ASE} = (S_{ASE}\delta\nu)^{1/2} \sum_{k=1}^{K} \exp[-i(\omega_k t - \varphi_k)]. \qquad (5.23)$$

The photocurrent generated at the photodiode can be modified as:

$$I_{ph} = R|\sqrt{G}E + E_{ASE}|^2 + \Delta I_S + \Delta I_T. \qquad (5.24)$$

While the thermal noise variance σ_T^2 remains the same as before, the shot noise variance of the amplified light now becomes:

$$\sigma_S^2 = \sigma_{S_{comb}}^2 + \sigma_{S_{ASE}}^2 = 2e \cdot R(2NP_0 G + P_{ASE}) \cdot f_{\text{BW}}, \qquad (5.25)$$

which has optical power contributed from both the amplified comb signals and the ASE noise. Besides the shot noise, from equation (5.24), the ASE noise field can also induce extra noise current I_{ASE}, which includes the ASE field photomixing with the

amplified signal (I_{sig-sp}), and ASE field photomixing with itself (I_{sp-sp}):

$$I_{ASE} = I_{sig-sp} + I_{sp-sp}, \tag{5.26}$$

$$
\begin{aligned}
I_{sig-sp} &= R(\sqrt{G}EE^*_{ASE} + \sqrt{G}E^*E_{ASE}) \\
&= 2R\sqrt{G}(S_{ASE}\delta\nu)^{1/2} \sum_{k=1}^{K}\left(\sum_{n=1}^{N} A_n^S \cos[(\omega_n^S - \omega_k)t + \varphi_k - \varphi_n^S] \right. \\
&\quad \left. + \sum_{n=1}^{N} A_n^L \cos[(\omega_n^L - \omega_k)t + \varphi_k - \varphi_n^L] \right) \\
&= 2R\sqrt{G}A_0(S_{ASE}\delta\nu)^{1/2} \sum_{k=1}^{K}\left(\sum_{n=1}^{N} \cos[(\omega_n^S - \omega_k)t + \varphi_k - \varphi_n^S] \right. \\
&\quad \left. + \sum_{n=1}^{N} \cos[(\omega_n^L - \omega_k)t + \varphi_k - \varphi_n^L] \right),
\end{aligned}
\tag{5.27}
$$

$$
\begin{aligned}
I_{sp-sp} &= R \cdot E_{ASE}E^*_{ASE} \cdot 2 \\
&= 2RS_{ASE}\delta\nu \sum_{k=1}^{K} \exp[-i(\omega_k t - \varphi_k)] \sum_{l=1}^{K} \exp[i(\omega_l t - \varphi_l)] \\
&= 2RS_{ASE}\delta\nu \sum_{k=1}^{K}\sum_{l=1}^{K} \cos[(\omega_k - \omega_l)t + \varphi_l - \varphi_k],
\end{aligned}
\tag{5.28}
$$

where the factor of 2 in I_{sp-sp} includes both two orthogonal polarization modes. Note that only terms with their frequencies within the photodiode bandwidth should be kept in the calculation, i.e., $|\omega_n^{S(L)} - \omega_k| \leq f_{\text{BW}}$ and $|\omega_k - \omega_l| \leq f_{\text{BW}}$. To derive the variances, we can first calculate the average values of I_{sig-sp}, I_{sp-sp}:

$$< I_{sig-sp} >= 0, \tag{5.29}$$

$$< I_{sp-sp} >= 2RS_{ASE}\delta\nu K = 2RS_{ASE}\Delta\nu = R \cdot P_{ASE}, \qquad (5.30)$$

where we have considered the phase of ASE noise $\varphi_{k(l)}$ fluctuates with time. The expected values of I^2_{sig-sp}, I^2_{sp-sp} are given by:

$$< I^2_{sig-sp} >= 4R^2 P_0 G S_{ASE}\delta\nu \overline{\left[\sum_{k=1}^K \left(\sum_{n=1}^N \cos[(\omega_n^S - \omega_k)t + \varphi_k - \varphi_n^S] + \sum_{n=1}^N \cos[(\omega_n^L - \omega_k)t + \varphi_k - \varphi_n^L]\right)\right]^2}$$

$$= 4R^2 P_0 G S_{ASE}\delta\nu \times \left(\frac{2f_{BW}}{\delta\nu} \cdot 2N \cdot \frac{1}{2}\right) = 4R^2 \cdot (2N P_0 G) S_{ASE} \cdot f_{BW},$$

$$(5.31)$$

$$< I^2_{sp-sp} >= 4R^2 S_{ASE}^2 \delta\nu^2 \overline{\left(\sum_{k=1}^K \sum_{l=1}^K \cos[(\omega_k - \omega_l)t + \varphi_l - \varphi_k]\right)^2}$$

$$= 4R^2 S_{ASE}^2 \delta\nu^2 \times \left[K \cdot \frac{2f_{BW}}{\delta\nu} - \frac{f_{BW}}{\delta\nu}\left(\frac{f_{BW}}{\delta\nu} - 1\right)\right] \times \frac{1}{2} + 4R^2 S_{ASE}^2 \delta\nu^2 \times K^2$$

$$\approx 4R^2 S_{ASE}^2 \delta\nu^2 \times \left[2K \cdot \frac{f_{BW}}{\delta\nu} - \left(\frac{f_{BW}}{\delta\nu}\right)^2\right] \times \frac{1}{2} + 4R^2 S_{ASE}^2 \delta\nu^2 \times K^2 \qquad (5.32)$$

$$= 4R^2 S_{ASE}^2 \cdot f_{BW}(\Delta\nu - f_{BW}/2) + 4R^2 S_{ASE}^2 \Delta\nu^2,$$

where $f_{BW}/\delta\nu$ represents the number of frequency bins within PD bandwidth. $2f_{BW}/\delta\nu \cdot 2N$ is the number of terms whose frequencies fall within PD bandwidth for I^2_{sig-sp}. $K \cdot 2f_{BW}/\delta\nu - (f_{BW}/\delta\nu)(f_{BW}/\delta\nu + 1)$ and K^2 are the numbers of terms whose frequencies fall within PD bandwidth for I^2_{sp-sp} when $k \neq l$ and when $k = l$, respectively. As a result, the variances can be expressed as[127, 128, 126]:

$$\sigma^2_{sig-sp} = < I^2_{sig-sp} > - < I_{sig-sp} >^2 = 8R^2 N P_0 G S_{ASE} \cdot f_{BW}, \qquad (5.33)$$

$$\sigma^2_{sp-sp} = < I^2_{sp-sp} > - < I_{sp-sp} >^2 = 4R^2 S^2_{ASE} \cdot f_{\text{BW}}(\Delta\nu - f_{\text{BW}}/2). \qquad (5.34)$$

The total noise variance after optical amplification is:

$$\sigma^2_A = \sigma^2_S + \sigma^2_{sig-sp} + \sigma^2_{sp-sp} + \sigma^2_T. \qquad (5.35)$$

The ENOB after amplification can be expressed as:

$$\text{ENOB}_A = \frac{1}{2} \log_2 \frac{2R^2 \cdot N^2 P_0^2 G^2}{\sigma^2_A}$$

$$= \frac{1}{2} \log_2 \frac{2R^2 \cdot N^2 P_0^2 G^2}{[4eRNP_0G + R(F_nG-1)h\nu_0(2e\Delta\nu + 4RNP_0G + R(F_nG-1)h\nu_0(\Delta\nu - f_{\text{BW}}/2)) + k_BT/R_{load}] \cdot f_{\text{BW}}}.$$

$$(5.36)$$

To simplify this expression, three noise terms can be neglected with confidence. The first is the shot noise of ASE, since the optical power of ASE is usually much smaller than the optical power of amplified comb lines. The second is the photomixing of ASE field with itself, which can be significantly suppressed using optical filters. The last term is the shot noise of amplified comb lines, as it is found to be always much smaller than the noise contributed from the photomixing of the ASE field and the amplified signal field:

$$\sigma^2_{S,comb} = 4eRNP_0G \cdot f_{\text{BW}} \ll 4\eta_{pd} \cdot eRNP_0G(F_nG - 1) \cdot f_{\text{BW}} = \sigma^2_{sig-sp}, \qquad (5.37)$$

where we have used amplifier gain $G \gg 1$, and the expression of responsivity $R =$

$\eta_{pd} \cdot e/h\nu$, η_{pd} is the quantum efficiency of the photodiode. The amplifier noise figure F_n is usually bigger than 2 (3 dB in log scale). Then the remaining noise sources only include the thermal noise, and the noise from the photomixing between the ASE field and the amplified signal field. Equation (5.36) can be reduced to:

$$
\begin{aligned}
ENOB_A &\approx \frac{1}{2} \log_2 \left[\frac{2R^2 \cdot N^2 P_0^2 G^2}{[4\eta_{pd} \cdot eR(F_n G - 1)NP_0 G + k_B T/R_{load}] \cdot f_{\mathrm{BW}}} \right] \\
&\approx \frac{1}{2} \log_2 \left[\frac{2R^2 \cdot N^2 P_0^2 G^2}{[4\eta_{pd} \cdot eRF_n G^2 NP_0 + k_B T/R_{load}] \cdot f_{\mathrm{BW}}} \right].
\end{aligned}
\tag{5.38}
$$

Plugging eqs. (5.17,5.18,5.20) into eq. (5.38), ENOB after amplification can be expressed as:

$$
\begin{aligned}
ENOB_A &= \frac{1}{2} \log_2 \left[\frac{R^2 \cdot \alpha^2 N^2 P_c^2 G^2}{2[2\eta_{pd} \cdot eRF_n G^2 \alpha N P_c + k_B T/R_{load}] \cdot f_{\mathrm{BW}}} \right] \\
&= \frac{1}{2} \log_2 \left[\frac{(0.8814\eta)^4 \cdot R^2 \cdot \alpha^2 P_{pump,min}^2 G^2}{2[2(0.8814\eta)^2 \eta_{pd} \cdot eR \cdot F_n G^2 \cdot \alpha P_{pump,min}/N + k_B T/R_{load}]N^2 \cdot f_{\mathrm{BW}}} \right].
\end{aligned}
\tag{5.39}
$$

Equation (5.39) is used for plotting ENOB with amplifier in Fig. 5**a** and Fig. 5**b**.

5.6 Summary

In this chapter, we have demonstrated arbitrary RF waveform generation through spectral line-by-line shaping with optical dual-microresonator solitons. The ultra-high analog bandwidth has been the key advantage of photonic AWG systems. 60 GHz analog bandwidth has been achieved previously using frequency-to-time map-

ping[111] and direct time-domain synthesis[115]. The analog bandwidth of the dual-comb Fourier synthesis method is ultimately limited by the Nyquist frequency of optical coherent sampling[106], i.e., half of the optical frequency comb repetition rate, and the bandwidth of the photodiode. The Nyquist frequency of dual-microcomb can range from a few GHz up to a few hundred GHz [65, 66]. The high Nyquist frequency has been applied to increase the bandwidth or sampling rate in dual-microcomb spectroscopy [13, 21], Lidar[24, 25] and imaging[23, 22]. In terms of photodiodes, bandwidth exceeding 100s GHz has been demonstrated, and has been combined with soliton microcombs to generate RF signals with exceptional performance in power [129], phase noise[130, 131] and time jitter [132]. It is thus possible to extend the analog bandwidth of dual-microcomb AWG beyond 100 GHz. In addition, all the critical components in dual-microcomb Fourier synthesis, including laser, Kerr microresonators, multiplexers/demultiplexers, modulators, amplifiers, and ultrafast photodiodes, have all been shown to be compatible with silicon photonics integration. Also, it eliminates the need of low-rate mode-locked lasers and long tunable delay lines required by the previous proposed on-chip solutions[111, 115, 116], and has the potential of mass-production on a photonic chip. Finally, the time-bandwidth product (TBWP) of our current static arbitrary waveform demonstration is limited by the number of comb lines, which gives a maximum TBWP of 20. In contrast, a TBWP of 600 has been demonstrated by combining frequency-to-time mapping and optical interferometry[112]. In the future, the TBWP of our method can be increased dramatically by replacing the static waveshaper with phase and amplitude modulators for dynamic line-by-line phase and amplitude control [118, 98, 104], and the the time aperture of the waveforms will be directly set by the time aperture of modulation signals.

In our experiment, the analog bandwidth of the waveform is 3 GHz, which is set purposely such that the waveform bandwidth will not exceed our oscilloscope bandwidth. The waveform analog bandwidth in our dual-microcomb method can be conveniently increased by adjusting the FSR difference between the two soliton microresonators, which can be precisely controlled in microfabrication. In addition, although the demonstrated waveform generation is periodic and static, dynamic waveform generation can be implemented by using time varying amplitude and phase modulation of the optical comb lines through integrated photonic modulators [118, 98, 104].

Chapter 6

Background of quantum optics

6.1   Introduction

We have covered some introductions of the physics of microcombs in the classic regime in the previous chapters. In this chapter, the concept of quantum optics will be briefly introduced before we move to the quantum experiments in microresonators. Detailed introduction of quantum optics can be found in found in references[133, 134, 135].

6.2   Quantization of the eletctromagnetic field

The quantization of the electromagnetic field is essential to explore the quantum properties of the light. To get started, it is more convenient to describe the field constrained to a certain volume and in a discrete form consists of the cavities mode[135], which leads to the mode expansion form of electric field

$$\mathbf{E}(\mathbf{r}, t) = i \sum_k \sqrt{\frac{\hbar \omega_k}{2\epsilon_0}} [a_k \mathbf{u}_k(\mathbf{r}) e^{-i\omega_k t} - a_k^\dagger \mathbf{u}_k^*(\mathbf{r}) e^{i\omega_k t}], \tag{6.1}$$

where $\mathbf{u}_k$ are a series of discrete orhtogonal mode functions which represent the electric fields in the certain volume, ω_k is the frequency of mode k and a_k is the complex Fourier amplitude and are dimensionless. Quantization of the electromagnetic field

can be accomplished by choosing annihilation operator $\hat{a}_k$ and creation operator $\hat{a}_k^\dagger$ that satisfy the boson commutation relations

$$[\hat{a}_k, \hat{a}'_k] = [\hat{a}_k^\dagger, \hat{a}_k'^\dagger] = 0, \quad [\hat{a}_k, \hat{a}_k'^\dagger] = \delta_{kk'}. \tag{6.2}$$

The Hamiltonian of the electromagnetic field in the volume can be written as

$$\hat{H} = \frac{1}{2} \int (\epsilon_0 \mathbf{E}^2 + \mu_0 \mathbf{H}^2) d\mathbf{r} = \sum_k \hbar\omega_k (\hat{a}_k^\dagger \hat{a}_k + \frac{1}{2}). \tag{6.3}$$

The Hamiltonian is the sum of the photon number times the energy per photon in each cavity mode, plus the energy of half a photon which represents the vacuum fluctuations in each mode. This can be understood as an analogy to the harmonic oscillator.

Define Hermitian operators $\hat{P}$ and $\hat{Q}$ that are observables in experiments,

$$\hat{Q} = \frac{\hat{a} + \hat{a}^\dagger}{\sqrt{2}}, \tag{6.4}$$

$$\hat{P} = -i\frac{\hat{a} - \hat{a}^\dagger}{\sqrt{2}}, \tag{6.5}$$

They satisfy the commutation relation and the Heisenberg uncertainty principle

$$[\hat{Q}, \hat{P}] = i, \tag{6.6}$$

$$\Delta \hat{Q} \Delta \hat{P} \geq \frac{1}{2}. \tag{6.7}$$

6.3   Time evolution

Quantum systems can evolve with time. Different approaches are used to mathematically describe the dynamics of the system. These approaches are called dynamical pictures, including the Schrödinger picture, the Heisenberg picture and the interaction picture.

6.3.1   Schrödinger picture

In the Schrödinger picture, the operators stay constant and the quantum state evolves with time. The evolution in the Schrödinger picture is given by

$$\frac{d|\psi(t)\rangle}{dt} = -\frac{i}{\hbar} \hat{H} |\psi(t)\rangle, \tag{6.8}$$

where $|\psi\rangle$ is the quantum state vector or wave function and $\hat{H}$ is the Hamiltonian of the quantum system. The evolution of the quantum state from time t_0 to t can be written as

$$|\psi(t)\rangle = U(t, t_0)|\psi(t_0)\rangle, \tag{6.9}$$

where $U(t, t_0)$ is the time-evolution operator. If the Hamiltonian commutes with itself at different times, the time-evolution operator can be written as

$$U(t, t_0) = e^{-\frac{i}{\hbar} \int_{t_0}^{t} \hat{H}(t') dt'}. \tag{6.10}$$

The expectation value of an observable $\hat{O}(t)$ can be obtained as

$$\langle \hat{O}(t) \rangle = \langle \psi(t) | \hat{O}(t) | \psi(t) \rangle. \tag{6.11}$$

6.3.2 Heisenberg picture

In the Heisenberg picture, the operators evolve with time while the quantum state stay constant. The expectation value of an operator should stay the same no matter which picture it is described in

$$\begin{aligned} \langle \hat{O} \rangle &= \langle \psi(t) | \hat{O} | \psi(t) \rangle \\ &= \langle \psi(t_0) | U(t, t_0)^\dagger \hat{O} U(t, t_0) | \psi(t_0) \rangle \\ &= \langle \psi(t_0) | \hat{O}(t) | \psi(t_0) \rangle. \end{aligned} \tag{6.12}$$

This can be understood as the wave function remains constant and the operator evolves from time t_0 to t as

$$\hat{O}(t) = U(t, t_0)^\dagger \hat{O} U(t, t_0). \tag{6.13}$$

The equation of motion of an operator in the Heisenberg picture is given by

$$\frac{d\hat{O}(t)}{dt} = -\frac{i}{\hbar}[\hat{O}(t), \hat{H}]. \tag{6.14}$$

This is known as the Heisenberg equation.

6.3.3 Interaction picture

In the interaction picture, both the operators and quantum state evolve with time. We can write the Hamiltonian of the quantum system as

$$\hat{H} = \hat{H}_0 + \hat{V}, \tag{6.15}$$

where $\hat{H}_0$ is the free part of the Hamiltonian that doesn't interaction between the sub-systems and $\hat{V}$ is the interaction Hamiltonian that describes the coupling between the sub-systems. $\hat{H}_0$ can be understood as an analogy to the kinetic energy of a series of particles and $\hat{V}$ can be understood as an analogy to the potential energy among those particles. We can include the time-dependent terms in $\hat{V}$ and leave $\hat{H}_0$ constant. The evolution operator under the Hamiltonian $\hat{H}_0$ can be obtained through Eq. (6.10) as

$$\hat{U}_0(t) = e^{-\frac{i\hat{H}_0(t-t_0)}{\hbar}}. \tag{6.16}$$

Define an operator in the interaction picture

$$\hat{O}_I(t) = \hat{U}_0(t)\hat{O}\hat{U}_0(t)^\dagger. \tag{6.17}$$

Take time derivative of Eq. (6.17), we obtain

$$\frac{d\hat{O}_I(t)}{dt} = \frac{i}{\hbar}[\hat{O}_I, \hat{H}_0] + \hat{U}_0 \frac{d\hat{O}_H}{dt} \hat{U}_0^\dagger. \tag{6.18}$$

We can derive from the Heisenberg equation that

$$\hat{U}_0 \frac{d\hat{O}_H}{dt} \hat{U}_0^\dagger = -\frac{i}{h}([\hat{O}_I, \hat{H}_0] + [\hat{O}_I, \hat{V}]). \tag{6.19}$$

Substituting this equation into the time derivative Eq. (6.18) leads to

$$\frac{d\hat{O}_I(t)}{dt} = -\frac{i}{h}[\hat{O}_I, \hat{V}]. \tag{6.20}$$

The expectation value of the operator $\hat{O}$ at time t should remain the same in the interaction picture as in other two pictures,

$$\begin{aligned}
\langle \hat{O} \rangle &= \langle \psi(t)_I | \hat{O}_I | \psi(t)_I \rangle \\
&= \langle \psi_I(t) | \hat{U}_0(t) \hat{U}(t, t_0)^\dagger \hat{O} \hat{U}(t, t_0) \hat{U}_0^\dagger(t) | \psi_I(t) \rangle \\
&= \langle \psi(t_0) | U(t, t_0)^\dagger \hat{O} U(t, t_0) | \psi(t_0) \rangle,
\end{aligned} \tag{6.21}$$

where $\psi_I(t)$ is the wave function defined in the interaction picture. To satisfy the last equation to preserve the expectation value among different dynamical pictures, the wave function $\psi_I(t)$ should satisfy

$$|\psi_I(t)\rangle = \hat{U}_0 |\psi(t_0)\rangle. \tag{6.22}$$

This indicates that the wave function in the interaction picture only evolves with the

free part of Hamiltonian $\hat{H}_0$. The time derivative of Eq. (6.22) gives the equation of motion

$$\frac{d|\psi_I(t)\rangle}{dt} = -\frac{i}{\hbar}|\psi(t_0)\rangle. \tag{6.23}$$

6.4 Quantum states

In this section, we will briefly introduce the states in quantum optics.

6.4.1 Fock state

Fock states are eigenstates of the photon number operator $\hat{N} = \hat{a}^\dagger \hat{a}$ and the wave functions $|n\rangle$ are their eigenvectors, where we have

$$\hat{a}^\dagger|n\rangle = \sqrt{n+1}|n+1\rangle, \tag{6.24}$$

$$\hat{a}|n\rangle = \sqrt{n}|n-1\rangle, \tag{6.25}$$

$$\hat{N}|n\rangle = n|n\rangle, \tag{6.26}$$

$$\hat{H}|n\rangle = (n+\frac{1}{2})|n\rangle. \tag{6.27}$$

Note that in the specific fock state where $n = 0$, it is called the vacuum state. We

can calculate the expectation values and deviations of the quadrature operators $\hat{Q}$ and $\hat{P}$

$$
\begin{aligned}
\langle\hat{Q}\rangle &= \langle n|\hat{Q}|n\rangle = \frac{1}{\sqrt{2}}\langle n|\hat{a} + \hat{a}^{\dagger}|n\rangle = 0, \\
\langle\hat{P}\rangle &= \langle n|\hat{P}|n\rangle = -\frac{i}{\sqrt{2}}\langle n|\hat{a} - \hat{a}^{\dagger}|n\rangle = 0,
\end{aligned}
\tag{6.28}
$$

In a similar way, we can get

$$
\begin{aligned}
\langle\hat{Q}^2\rangle &= \langle n|\hat{Q}^2|n\rangle = n + \frac{1}{2}, \\
\langle\hat{P}^2\rangle &= \langle n|\hat{P}^2|n\rangle = n + \frac{1}{2},
\end{aligned}
\tag{6.29}
$$

The deviations are then given by

$$
\begin{aligned}
\Delta Q &= \sqrt{\langle\hat{Q}^2\rangle - (\langle\hat{Q}\rangle)^2} = \sqrt{n + \frac{1}{2}}, \\
\Delta P &= \sqrt{\langle\hat{P}^2\rangle - (\langle\hat{P}\rangle)^2} = \sqrt{n + \frac{1}{2}}.
\end{aligned}
\tag{6.30}
$$

In the vacuum state, which is the minimum uncertainty state, we have the Heisenberg uncertainty relation taking the equals sign

$$
\Delta\hat{Q}\Delta\hat{P} = \frac{1}{2}.
\tag{6.31}
$$

The deviations of quadrature operators are constant in a given fock state and are

independent of quadrature angle. The expectation values of quadrature operators are zero. The quantum state appears as a circle that centers at the origin in the phase space with a radius of $\sqrt{n + \frac{1}{2}}$.

6.4.2 Coherent state

Coherent states $|\alpha\rangle$ are eigenstates of the annihilation operators $\hat{a}$,

$$\hat{a}|\alpha\rangle = \alpha|\alpha\rangle. \tag{6.32}$$

Coherent states can be describe as classical electromagnetic waves. The annihilation operator $\hat{a}$ is usually not hermitian and its eigenvalue α is a complex number that can be written as

$$\alpha = |\alpha|e^{i\theta}, \tag{6.33}$$

where $|\alpha|$ and θ are the amplitude and phase of the eigenvalue α. A stable optical field that is above the parametric threshold can be treated as a coherent state. The coherent state can be written in the photon number basis as

$$|\alpha\rangle = e^{-\frac{|\alpha|^2}{2}} \sum_{n=0}^{\infty} \frac{\alpha^n}{\sqrt{n!}}|n\rangle. \tag{6.34}$$

The expectation value and deviation of the photon number are given by

$$\langle \hat{N} \rangle = \langle \alpha | \hat{N} | \alpha \rangle = |\alpha|^2,$$

$$\Delta \hat{N} = |\alpha|. \tag{6.35}$$

The expectation values and deviations of the quadrature operators $\hat{Q}$ and $\hat{P}$ are given by

$$\langle \hat{Q} \rangle = \frac{1}{\sqrt{2}}(\alpha + \alpha^*),$$

$$\langle \hat{P} \rangle = -\frac{i}{\sqrt{2}}(\alpha - \alpha^*), \tag{6.36}$$

$$\Delta \hat{Q} = \frac{1}{\sqrt{2}},$$

$$\Delta \hat{P} = \frac{1}{\sqrt{2}}. \tag{6.37}$$

The coherent state is also a minimum uncertainty state. Unlike the vacuum state where it appears as a circle that centers at the origin in the phase space, the coherent state centers at a distance to the origin that equals to $\sqrt{\hat{N}}$.

6.4.3   Squeezed state

In a squeezed state, one of the quadrature operators has smaller deviation than that of the vacuum state, while the deviation of the other quadrature operator is larger than that of the vacuum state. The Heisenberg uncertainty relation is still satisfied.

In the rest of the introduction, we will particularly focus on the squeezed vacuum state which mathematically can be obtained by applying a squeezing operator on a vacuum state. The squeezing operator can be written as

$$\hat{S}(\gamma) = e^{\frac{\gamma^*}{2}\hat{a}^2 - \frac{\gamma}{2}\hat{a}^{\dagger 2}},\tag{6.38}$$

where $\gamma = re^{i\phi}$. r is the squeezing parameter which is related to the squeezing generation process, such as nonlinear optics process. ϕ is related to the angle of the squeezed state in the phase space. In the Heisenberg picture, by applying the squeezing operator to the quantum state, we obtain the annihilation and creation operators as

$$\hat{a}(t) = \hat{S}(\gamma)^{\dagger}\hat{a}\hat{S}(\gamma) = \hat{a}\cosh r - \hat{a}^{\dagger}e^{i\phi}\sinh r,$$
$$\hat{a}(t)^{\dagger} = \hat{S}(\gamma)^{\dagger}\hat{a}^{\dagger}\hat{S}(\gamma) = \hat{a}^{\dagger}\cosh r - \hat{a}^{\dagger}e^{-i\phi}\sinh r \tag{6.39}$$

These two equations are known as the Bogoliubov transformation. The expectation value and deviation of the photon number operator in a squeezed vacuum state is given by

$$\langle\hat{N}(t)\rangle = \langle 0|\hat{S}^{\dagger}(\gamma)\hat{N}\hat{S}(\gamma)|0\rangle = \sinh^2 r,$$
$$\Delta\hat{N}(t) = \sqrt{\Delta[\hat{N}(t)]^2 - [\Delta\hat{N}(t)]^2} = \frac{1}{\sqrt{2}}|\sinh 2r|. \tag{6.40}$$

The generalized quadrature operator can be defined as

$$\hat{A}_\theta = \hat{Q}cos\theta + \hat{P}sin\theta. \tag{6.41}$$

The expectation value and deviation of $\hat{A}_\phi$ are given by

$$\langle\hat{A}_\theta\rangle = 0,$$
$$\Delta\hat{A}_\theta = \frac{1}{\sqrt{2}}\sqrt{cos(2\theta - \phi)sinh2r + cosh2r}. \tag{6.42}$$

When $\phi = 0$, the equation above reduces to the form

$$\Delta\hat{A}_\theta = \sqrt{(\Delta\hat{Q})^2cos^2\theta + (\Delta\hat{P})^2sin^2\theta} = \frac{1}{\sqrt{2}}\sqrt{e^{2r}cos^2\theta + e^{-2r}sin^2\theta}. \tag{6.43}$$

In the more general case when $\phi \neq 0$, we can get $\Delta\hat{A}_\theta(\theta = \phi/2) = e^r/\sqrt{2}$. Therefore the phase term ϕ in the squeezing parameter represents twice the angle of the squeezed state in the phase space.

6.5   Squeezing in nonlinear optics

Squeezed states can be generated in nonlinear optics processes, such as parametric down-conversion and four-wave mixing. In this section, we will introduce the generation of single-mode squeezed state and two-mode squeezed state in nonlinear optics. The calculations will be performed in the interaction picture.

6.5.1 Single-mode squeezed state

A single-mode squeezed state is a quantum state where only one frequency mode is involved in the squeezing quadrature operators. Consider the interaction Hamiltonian in the parametric down-conversion process

$$\hat{H}_{int} = i\hbar\frac{g}{2}(\hat{a}^{\dagger 2}\hat{a}_p - \hat{a}^2\hat{a}_p^\dagger) = i\hbar\frac{g}{2}(\hat{a}^{\dagger 2}\alpha_p - \hat{a}^2\alpha_p^*), \tag{6.44}$$

where $\hat{a}_p$ and $\hat{a}$ are the annihilation operators of the pump mode and the half-frequency mode respectively,g is the interaction rate. The strong pump laser light $\hat{a}_p$ can be approximate to the coherent field, and operator $\hat{a}_p$ and $\hat{a}^\dagger$ can be substituted by complex number α_p and α_p^*.

The equations of motion of the quadrature operators can be obtained through the interaction picture as

$$\begin{aligned}
\frac{d\hat{Q}}{dt} &= \gamma\hat{Q}, \\
\frac{d\hat{P}}{dt} &= -\gamma\hat{P}.
\end{aligned} \tag{6.45}$$

where we defined $\gamma = \frac{g}{2}\alpha_p$. The equations of motion show squeezing and anti-squeezing of the quadrature operators.

6.5.2 Two-mode squeezed state

A two-mode squeezed state is a quantum state where two frequency modes are involved in the squeezing quadrature operators. Consider the interaction Hamiltonian

in the four-wave mixing process

$$\hat{H}_{int} = \sum_n \hbar g(\hat{a}_p \hat{a}_p \hat{a}_n^\dagger \hat{a}_{-n}^\dagger + \hat{a}_p^\dagger \hat{a}_p^\dagger \hat{a}_n \hat{a}_{-n}) = \sum_n \hbar g(\alpha_p^2 \hat{a}_n^\dagger \hat{a}_{-n}^\dagger + \alpha_p^{*2} \hat{a}_n \hat{a}_{-n}), \qquad (6.46)$$

where g is the interaction rate, n is mode number relative to the mode being pumped, and $\hat{a}_p$ is the annihilation operator of the pump light. The strong pump laser light can be approximate to the coherent field, and operator $\hat{a}_p$ and $\hat{a}^\dagger$ can be substituted by complex number α_p and α_p^*, respectively. We can define quadrature operators for different frequency modes as

$$\hat{Q}_k = \frac{\hat{a}_k + \hat{a}_k^\dagger}{\sqrt{2}},$$
$$\hat{P}_k = \frac{\hat{a}_k - \hat{a}_k^\dagger}{i\sqrt{2}}, \qquad (6.47)$$
$$[\hat{Q}_k, \hat{P}_k] = i,$$

where $\hat{Q}_k$ and $\hat{P}_k$ are quadrature operators of frequency mode k. The equations of motion through the interaction picture are given by

$$\frac{d}{dt}(\hat{Q}_n + \hat{Q}_{-n}) = \gamma(\hat{Q}_n + \hat{Q}_{-n}),$$
$$\frac{d}{dt}(\hat{Q}_n - \hat{Q}_{-n}) = -\gamma(\hat{Q}_n - \hat{Q}_{-n}),$$
$$\frac{d}{dt}(\hat{P}_n + \hat{P}_{-n}) = -\gamma(\hat{P}_n + \hat{P}_{-n}), \qquad (6.48)$$
$$\frac{d}{dt}(\hat{P}_n - \hat{P}_{-n}) = \gamma(\hat{P}_n - \hat{P}_{-n}),$$

where we have used $\gamma = g|\alpha_p|^2$, and $\alpha_p = |\alpha_p|e^{i\pi/4}$ as a rotation operation. This set of equations of motion clearly shows that $(\hat{Q}_n - \hat{Q}_{-n})$ and $(\hat{P}_n + \hat{P}_{-n})$ are squeezed. Note that this calculation does not include the effects of cavity dissipation, waveguide-cavity coupling, laser-cavity detuning, Kerr self/cross phase modulation or resonator dispersion. The modelling of the squeezing generation considering those effects will be introduced in the next chapter.

Chapter 7

Two-mode squeezed microcomb

7.1 Introduction

In this chapter, we will introduce the concept and theory of two-mode squeezed states generation through Kerr effect (four-wave mixing) in a microresonator, detection approaches of the squeezed states and the first demonstration of two-mode squeezed optical frequency comb in a microresonator.

Optical microresonators employ the Kerr nonlinearity [34] to provide broadband parametric gain through four-wave mixing (FWM) among cavity resonance modes, where pairs of pump photons can be annihilated to generate signal and idler photons at lower and higher frequencies. The Kerr parametric process has been used to demonstrate microresonator-based frequency combs (microcombs)[6, 7] and dissipative Kerr cavity solitons[8, 9, 10, 11], which have revolutionized a wide range of applications from metrology [12] to spectroscopy[13]. The quantum aspects of microcomb have been studied recently [14, 15, 16, 17, 18, 19] for its capability of providing hundreds of frequency multiplexed quantum channels from a single microresonator. Access to individual quantum channels is possible through off-the-shelf wavelength-division-multiplexing filters thanks to microcombs' large free-spectral-ranges (FSRs), which range from a few GHz to 1 THz [65, 66] as opposed to the finer FSRs of fiber or bulk resonator-based combs. When combined with integrated photonic circuits, quantum

microcombs have the potential to revolutionize photonic quantum information processing.

So far, experiments of quantum microcombs have been limited to the probabilistic regime[15, 16, 17, 18], where entanglement is measured between randomly emitted photon pairs with postselecting, coincidence detection. The photon coincidence rate suffers from exponential decrease with the increase of photon number in a quantum state. Quantum architectures built upon probabilistic quantum states are not scalable without quantum memory, which allows repeat-until-success strategies[136, 137]. In contrast, a quantum microcomb in the deterministic regime, where the entanglement among different frequency modes can be deterministically generated and detected, will be a significant step forward towards the scalable quantum architecture on photonic chips.

One approach to constructing deterministic quantum microcombs is to leverage two-mode squeezing and create unconditional entanglement between the optical fields in optical frequency combs[138, 139, 140]. Squeezed light[141], with quantum uncertainty below than that of the vacuum field, has broad applications in science and technology, ranging from enhancing the gravitational wave detection sensitivity in LIGO[142], Gaussian boson sampling[143, 144], to continuous-variable-based quantum computing (CVQC) [145, 146, 147, 148]. The unconditional entanglement created by two-mode squeezing is between continuous optical fields, which can serve as quantum modes (qumodes) to encode quantum information through continuous-variable-based (CV) approaches[149] for applications in universal quantum computing[145, 146, 148], unconditional quantum teleportation[150], quantum dense coding[151], quantum secret sharing[152], and quantum key distribution[153]. Unlike probabilistic photonic qubit approaches, the unconditional entanglement in CV ap-

proaches enables the number of entangled quantum modes (qumodes) in a quantum state to be deterministically scaled up through frequency[138, 139, 154], time [155, 156, 157], or spatial multiplexing[158], which provides a scalable physical platform for continuous-variable quantum computing[149]. Squeezing is conventionally generated through nonlinear optics in bulk optical systems, such as optical parametric oscillators (OPOs)[159, 141], or atomic vapor[160, 161]. Squeezed quantum microcombs, when combined with integrated photonic circuits, Gaussian and non-Gaussian measurements, can serve as simple and compact building bricks for CV universal quantum computing[162], entanglement-assisted spectroscopy[163], and quantum networking for distributed quantum sensing[164]. While the generation[165, 166, 167, 168, 169, 170, 171, 27, 28, 29] and detection[172] of one or two squeezed frequency qumodes, and the generation of 8 spatial qumodes[144] have been shown in miniaturized platforms recently, a squeezed microcomb has not been reported yet.

7.2 Two-mode squeezed states generation in a microresonator

In this section, we will introduce the concept and theory of two-mode squeezed states generation and detection in a microresonator. We will also discuss the factors that may impact the squeezing detection such as optical loss and phase noise.

7.2.1 Concept of two-mode squeezed microcomb

The Kerr parametric (four-wave mixing) process generates unconditional Einstein-Podolsky-Rosen (EPR) entanglement, i.e., two-mode squeezing, between the optical
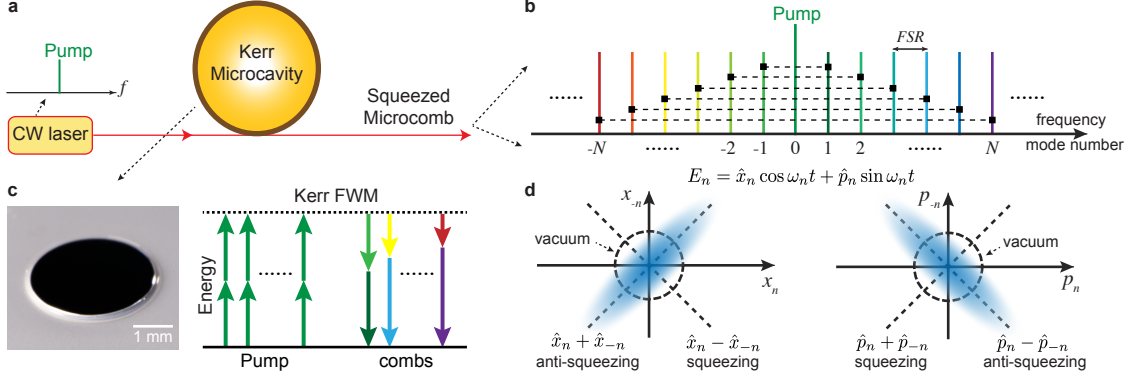
Figure 7.1: **Generation of deterministic, two-mode squeezed quantum microcombs on a chip.** **(a)** A continuous-wave (cw) pump laser is coupled to a microresonator, which has thousands of longitude resonance modes with their frequencies separated by the resonator free-spectral-range (FSR), as shown in panel **(b)**. **(c)** The $\chi^{(3)}$ Kerr nonlinearity in the microresonator creates broadband parametric gain as the pump photon pairs (green) can be converted into signal and idler photons at lower and higher frequency modes. This non-classical correlation creates two-mode vacuum squeezing and thus unconditional EPR entanglement of the optical quadrature fields between frequency modes n and $-n$, which are connected by dashed black lines in the optical spectrum in panel (b). Also shown is the image of a silica microresonator on a silicon chip used in this work. **(d)** Conceptual illustration of the two-mode squeezing wavefunctions in position (left) and momentum (right) basis, where ($\hat{x}_n$ - $\hat{x}_{-n}$) and ($\hat{p}_n$ + $\hat{p}_{-n}$) have uncertainty level below the vacuum fluctuation (dashed circle). The electrical field of the n-th optical mode is $E_n = \hat{x}_n \cos \omega_n t + \hat{p}_n \sin \omega_n t$, where $\hat{x}_n$ and $\hat{p}_n$ are the in-phase and out-of-phase quadrature amplitudes of the mode at frequency ω_n.

quadrature fields of the qumode pairs in the microresonator[14, 28]. The concept is demonstrated in Fig. 7.1. The Kerr microresonator is pumped by a continuous-wave laser. Through the four-wave mixing process, two pump photons are converted to a signal photon and an idler photon simultaneously. This process satisfies energy and momentum conservation, and the sum frequency of the signal and idler photons equals that of the two pump photons. As a result, entanglement is established between the signal mode and the idler mode.

7.2.2 Evolution of the annihilation and creation operators

In Section 6.5.2, we calculated the two-mode squeezed state generation in the four-wave mixing process in a simple way. Here we will include the effects of cavity dissipation, waveguide-cavity coupling, laser-cavity detuning, Kerr self/cross phase modulation or resonator dispersion. When taken all effects into account, the Hamiltonian in the interaction picture can be written as[173, 174, 14]

$$
\begin{aligned}
\hat{H}_{\text{int}} = -\,\hbar g \Big[& (\hat{a}_n^\dagger \hat{a}_{-n}^\dagger \hat{a}_p \hat{a}_p + \hat{a}_n \hat{a}_{-n} \hat{a}_p^\dagger \hat{a}_p^\dagger) + 2(\hat{a}_p^\dagger \hat{a}_n^\dagger \hat{a}_p \hat{a}_n + \hat{a}_p^\dagger \hat{a}_{-n}^\dagger \hat{a}_p \hat{a}_{-n} + \hat{a}_n^\dagger \hat{a}_{-n}^\dagger \hat{a}_n \hat{a}_{-n}) \\
& + \frac{1}{2} \sum_{j=p,\pm n} (\hat{a}_j^\dagger \hat{a}_j^\dagger \hat{a}_j \hat{a}_j) \Big].
\end{aligned}
\tag{7.1}
$$

With the effect of dispersion, external coupling, cavity dissipation and laser-cavity detuning, the quantum Langevin equations are given in the following forms:

$$
\begin{aligned}
\frac{d\hat{a}_p}{dt} =& -(\kappa + i\delta_p)\hat{a}_p + ig\left[(\hat{a}_p^\dagger \hat{a}_p + 2\hat{a}_n^\dagger \hat{a}_n + 2\hat{a}_{-n}^\dagger \hat{a}_{-n})\hat{a}_p + 2\hat{a}_p^\dagger \hat{a}_n \hat{a}_{-n}\right] \\
& + \sqrt{2\kappa_c}\hat{a}_{\kappa_c,p} + \sqrt{2\kappa_0}\hat{a}_{\kappa_0,p}, \\
\frac{d\hat{a}_n}{dt} =& -(\kappa + i\delta_n)\hat{a}_n + ig\left[(2\hat{a}_p^\dagger \hat{a}_p + \hat{a}_n^\dagger \hat{a}_n + 2\hat{a}_{-n}^\dagger \hat{a}_{-n})\hat{a}_n + \hat{a}_p^2 \hat{a}_{-n}^\dagger\right] \\
& + \sqrt{2\kappa_c}\hat{a}_{\kappa_c,n} + \sqrt{2\kappa_0}\hat{a}_{\kappa_0,n}, \\
\frac{d\hat{a}_{-n}}{dt} =& -(\kappa + i\delta_{-n})\hat{a}_{-n} + ig\left[(2\hat{a}_p^\dagger \hat{a}_p + 2\hat{a}_n^\dagger \hat{a}_n + \hat{a}_{-n}^\dagger \hat{a}_{-n})\hat{a}_{-n} + \hat{a}_p^2 \hat{a}_n^\dagger\right] \\
& + \sqrt{2\kappa_c}\hat{a}_{\kappa_c,-n} + \sqrt{2\kappa_0}\hat{a}_{\kappa_0,-n},
\end{aligned}
\tag{7.2}
$$

where we have transformed into the relative frequency frame (rotating frame, or equidistant frequency frame) by replacing $\hat{a}_n$ with $\hat{a}_n e^{-i\Omega_n t}$. The frequency Ω_n is defined as $\Omega_n = \omega_p + D_1$, where D_1 is the free-spectral-range (FSR) of the microres-

onator. $\delta_n \equiv \omega_n - \Omega_n$ is the frequency detuning between the cavity resonant frequency ω_n and the equidistant frequency. κ_0 is the cavity dissipation rate, κ_c is the external coupling rate, $\hat{a}_{\kappa_0}$ and $\hat{a}_{\kappa_c}$ are the vacuum fluctuation operators associated with the cavity dissipation rate and external coupling rate respectively, and $\kappa = \kappa_0 + \kappa_c$ is the total dissipation rate. The interaction rate g can be linked with the normalized Kerr parametric oscillation threshold to photon number, $\overline{P}_{th} = P_{th}/\hbar\omega$, as $g = \frac{\kappa}{\overline{P}_{th}}$ [174, 175, 40]. By doing Fourier transform on the fluctuation operators $\hat{a}_{\kappa_0,\pm n}$ and $\hat{a}_{\kappa_c,\pm n}$, in the frequency domain $\hat{\tilde{a}}_{\kappa_0,\pm n}$ and $\hat{\tilde{a}}_{\kappa_0,\pm n}$ have the following correlation relations,

$$
\begin{aligned}
\langle \hat{\tilde{a}}_{m,n}(\omega)\hat{\tilde{a}}_{m',n'}(\omega')^{\dagger}\rangle &= \delta_{m,m'}\delta_{n,n'}\delta(\omega - \omega'), \\
\langle \hat{\tilde{a}}_{m,n}(\omega)^{\dagger}\hat{\tilde{a}}_{m',n'}(\omega')\rangle &= 0, \\
\langle \hat{\tilde{a}}_{m,n}(\omega)\hat{\tilde{a}}_{m',n'}(\omega')\rangle &= \langle \hat{\tilde{a}}_{m,n}(\omega)^{\dagger}\hat{\tilde{a}}_{m',n'}(\omega')^{\dagger}\rangle = 0,
\end{aligned}
\tag{7.3}
$$

where m indicates "κ_0" or "κ_c", $\delta_{i,j}$ is the Kronecker delta and δ is the Dirac delta function. When the pump power is below the the parametric oscillation threshold, the annihilation operators can be linearized as,

$$
\begin{aligned}
\hat{a}_p &= \alpha_p + \delta\hat{a}_p, \\
\hat{a}_n &= \delta\hat{a}_n, \\
\hat{a}_{-n} &= \delta\hat{a}_{-n},
\end{aligned}
\tag{7.4}
$$

where α_p is a complex number. In our experiment, the pump mode is in steady state, and thus we have $\frac{d\hat{a}_p}{dt} = 0$. The resonator mode frequency can be expressed as $\omega_n = \omega_0 + D_1 n + \frac{1}{2}D_2 n^2 + ...$, where D_2 term represents group velocity dispersion. The results with higher orders of the dispersion can be derived in exactly the same way. When neglecting the higher order dispersion terms, we can have $\delta_n = \delta_{-n}$. Through the linearization process, neglecting higher order terms that are small, the quantum

Langevin equations in (7.2) become,

$$0 = -(\kappa + i\delta_p)\alpha_p + ig\left|\alpha_p\right|^2\alpha_p + \sqrt{2\kappa_c}\alpha_{in,p}, \quad \alpha_{in,p} = \sqrt{\frac{P_{in}}{\hbar\omega_p}},$$

$$\frac{d\delta\hat{a}_n}{dt} = -(\kappa + i\delta_n)\delta\hat{a}_n + ig\alpha_p^2\delta\hat{a}_{-n}^\dagger + \sqrt{2\kappa_c}\hat{a}_{\kappa_c,n} + \sqrt{2\kappa_0}\hat{a}_{\kappa_0,n},$$

$$\frac{d\delta\hat{a}_{-n}}{dt} = -(\kappa + i\delta_n)\delta\hat{a}_{-n} + ig\alpha_p^2\delta\hat{a}_n^\dagger + \sqrt{2\kappa_c}\hat{a}_{\kappa_c,-n} + \sqrt{2\kappa_0}\hat{a}_{\kappa_0,-n},$$

(7.5)

where P_{in} is the pump laser power in the waveguide/tapered fiber before coupling into the microresonator. Take $A = -(\kappa + i\delta_n) + i2g\left|\alpha_p\right|^2$, $B = ig\alpha_p^2$, the last two equations can be written as,

$$\frac{d\delta\hat{a}_n}{dt} = A\delta\hat{a}_n + B\delta\hat{a}_{-n}^\dagger + \sqrt{2\kappa_c}\hat{a}_{\kappa_c,n} + \sqrt{2\kappa_0}\hat{a}_{\kappa_0,n},$$

$$\frac{d\delta\hat{a}_{-n}^\dagger}{dt} = A^*\delta\hat{a}_{-n}^\dagger + B^*\delta\hat{a}_n + \sqrt{2\kappa_c}\hat{a}_{\kappa_c,-n}^\dagger + \sqrt{2\kappa_0}\hat{a}_{\kappa_0,-n}^\dagger.$$

(7.6)

The equations in (7.6) are relatively easy to solve in the frequency domain. Through the Fourier transform,

$$F\left[\hat{a}(t)\right] = \frac{1}{\sqrt{2\pi}}\int_{-\infty}^{\infty}\hat{a}(t)e^{i\omega t}dt \equiv \hat{\tilde{a}}(\omega),$$

$$F\left[\hat{a}^\dagger(t)\right] = \frac{1}{\sqrt{2\pi}}\int_{-\infty}^{\infty}\hat{a}^\dagger(t)e^{i\omega t}dt = \left[\hat{\tilde{a}}(-\omega)\right]^\dagger \equiv \hat{\tilde{a}}(-\omega)^\dagger,$$

(7.7)

the equations (7.6) can be expressed in the following forms in the frequency domain,

$$\mathbf{C}(\omega)\begin{pmatrix}\delta\hat{\tilde{a}}_n(\omega) \\ \delta\hat{\tilde{a}}_{-n}(-\omega)^\dagger\end{pmatrix} = \sqrt{2\kappa_c}\begin{pmatrix}\hat{\tilde{a}}_{\kappa_c,n}(\omega) \\ \hat{\tilde{a}}_{\kappa_c,-n}(-\omega)^\dagger\end{pmatrix} + \sqrt{2\kappa_0}\begin{pmatrix}\hat{\tilde{a}}_{\kappa_0,n}(\omega) \\ \hat{\tilde{a}}_{\kappa_0,-n}(-\omega)^\dagger\end{pmatrix},$$

$$\text{where } \mathbf{C}(\omega) \equiv \begin{pmatrix}-i\omega - A & -B \\ -B^* & -i\omega - A^*\end{pmatrix}.$$

(7.8)

To calculate the amount of squeezing and anti-squeezing in the output waveguide, the output annihilation operator, $\delta\hat{\bar{a}}_{out,n}$, can be expressed by the input-output relations,

$$
\begin{aligned}
\delta\hat{\bar{a}}_{out,n} &= -\sqrt{2\kappa_c}\delta\hat{\bar{a}}_n + \hat{\bar{a}}_{\kappa_c,n}, \\
\delta\hat{\bar{a}}^\dagger_{out,-n} &= -\sqrt{2\kappa_c}\delta\hat{\bar{a}}^\dagger_{-n} + \hat{\bar{a}}^\dagger_{\kappa_c,-n},
\end{aligned}
\tag{7.9}
$$

Then we have the annihilation operators on the output of the Kerr resonator,

$$
\begin{aligned}
\begin{pmatrix} \delta\hat{\bar{a}}_{out,n}(\omega) \\ \delta\hat{\bar{a}}_{out,-n}(-\omega)^\dagger \end{pmatrix} &= (\mathbf{I} - 2\kappa_c\mathbf{C}^{-1}(\omega)) \begin{pmatrix} \hat{\bar{a}}_{in,n}(\omega) \\ \hat{\bar{a}}_{in,-n}(-\omega)^\dagger \end{pmatrix} \\
&\quad - 2\sqrt{\kappa_0\kappa_c}\mathbf{C}^{-1}(\omega) \begin{pmatrix} \hat{\bar{a}}_{loss,n}(\omega) \\ \hat{\bar{a}}_{loss,-n}(-\omega)^\dagger \end{pmatrix}.
\end{aligned}
\tag{7.10}
$$

The annihilation operators are not observables. In experiment, we measure the quadrature operators instead, more specifically, the variances of the quadrature operators. The quadrature operators are defined as,

$$
\begin{aligned}
\delta\hat{X}_{out,\pm}(t) &= \frac{1}{\sqrt{2}}\left[\frac{1}{\sqrt{2}}(\delta\hat{a}_{out,n} + \delta\hat{a}^\dagger_{out,n}) \pm \frac{1}{\sqrt{2}}(\delta\hat{a}_{out,-n} + \delta\hat{a}^\dagger_{out,-n})\right], \\
\delta\hat{Y}_{out,\pm}(t) &= \frac{1}{\sqrt{2}}\left[\frac{1}{i\sqrt{2}}(\delta\hat{a}_{out,n} - \delta\hat{a}^\dagger_{out,n}) \pm \frac{1}{i\sqrt{2}}(\delta\hat{a}_{out,-n} - \delta\hat{a}^\dagger_{out,-n})\right],
\end{aligned}
\tag{7.11}
$$

and their variances are,

$$V_{X,\pm} = \langle \delta \hat{X}^{\dagger}_{out,\pm}(t) \delta \hat{X}_{out,\pm}(t) \rangle,$$
$$V_{Y,\pm} = \langle \delta \hat{Y}^{\dagger}_{out,\pm}(t) \delta \hat{Y}_{out,\pm}(t) \rangle. \tag{7.12}$$

We can get an explicit expression of the frequency components of the quadrature variances,

$$V_{X,\pm} = \langle \delta \hat{X}^{\dagger}_{out,\pm}(t) \delta \hat{X}_{out,\pm}(t) \rangle = \frac{1}{\sqrt{2\pi}} \int_{-\infty}^{\infty} d\omega \frac{S_{X,\pm}(\omega)}{\sqrt{2\pi}}, \tag{7.13}$$

where $S_{X,\pm}$ is the quadrature variance in the frequency domain, also known as the squeezing spectrum:

$$S_{X,\pm} = 4\kappa_c \kappa \left[\left| C_{11}^{-1}(\omega) \right|^2 + \left| C_{12}^{-1}(-\omega) \right|^2 \right] \pm 8\kappa_c \kappa Re \left[C_{11}^{-1}(\omega) C_{12}^{-1}(-\omega) \right]$$
$$- 4\kappa_c Re \left[C_{11}^{-1}(\omega) \pm C_{12}^{-1}(-\omega) \right] + 1. \tag{7.14}$$

$C_{11}^{-1}(\omega)$ and $C_{12}^{-1}(\omega)$ are the components of $\mathbf{C}^{-1}(\omega)$, and

$$\mathbf{C}^{-1}(\omega) = \begin{pmatrix} C_{11}^{-1}(\omega) & C_{12}^{-1}(\omega) \\ C_{21}^{-1}(\omega) & C_{22}^{-1}(\omega) \end{pmatrix}, \tag{7.15}$$

where

$$C_{11}^{-1}(\omega) = \frac{-i(\omega + A^*)}{|A|^2 + i2\omega Re(A) - \omega^2 - |B|^2}, \quad C_{12}^{-1}(\omega) = \frac{B}{|A|^2 + i2\omega Re(A) - \omega^2 - |B|^2},$$
$$C_{22}^{-1}(-\omega) = C_{11}^{-1}(\omega)^*, \quad C_{21}^{-1}(\omega) = C_{12}^{-1}(-\omega)^*. \tag{7.16}$$

The squeezing spectrum of the Y quadrature $S_{Y,\pm}$ can be derived in the same way.

7.2.3   Detection of the squeezed state

The optical field of the squeezed state is too small to be directly detected with phodiodes. In experiment, the variances of the quadrature operators can be measured with balanced homodyne detection[138], which can be understood as a linear amplification of the quadrature operators.

Frist consider a simple case to demonstrate the balance homodyne detection. In a single-mode squeezed state, the squeezed vacuum field $\hat{a}$ and the local oscillator (LO) field $\hat{b} = \beta e^{i\theta}$ are mixed by a 50/50 beam splitter or fiber coupler, where we used coherent state approximation for the LO field and β is the amlitude of the LO field, θ is the relative phase difference between the signal and LO in the rotation frame. The two output fields $\hat{c}_{\pm}$ from the beam splitter are given by

$$\hat{c}_{\pm} = \frac{1}{\sqrt{2}}(\hat{a} \pm \hat{b}). \tag{7.17}$$

The two outputs are sent to a balanced photodiodes, and the photocurrent is proportional to the photon number. The photon numbers on the photodiodes are given by

$$\begin{aligned}
\hat{N}_{\pm} = \hat{c}_{\pm}^{\dagger}\hat{c} &= \frac{1}{2}\hat{a}^{\dagger}\hat{a} \pm \frac{1}{2}\beta^2 + \beta(\hat{a}e^{-i\theta} + \hat{a}^{\dagger}e^{i\theta}) \\
&= \frac{1}{2}\hat{a}^{\dagger}\hat{a} + \frac{1}{2}\beta^2 \pm \frac{1}{\sqrt{2}}\beta(\hat{Q}cos\theta + \hat{P}sin\theta).
\end{aligned} \tag{7.18}$$

A balanced homodyne detector outputs the difference between the two photocurrents to cancel the noise introduced by the LO photon number term β^2 which is generally much larger than the vacuum noise. The different photocurrent is proportional to

the difference in photon numbers

$$\hat{N}_+ - \hat{N}_- = \sqrt{2}\beta(\hat{Q}cos\theta + \hat{P}sin\theta). \tag{7.19}$$

With balanced homodyne detection, a detector consists of regular photodiodes can detect the quantum signal that is amplified by the LO amplitude β. By changing the phase difference θ between the quantum signal and LO, difference quadrature operators, or the generalized quadrature operator at different phases can be detected.

For detection two-mode squeezed states, a bichromatic local oscillator can be used in the balanced homodyne detection. The optical fields of the quantum signal $\hat{a}$ and the LO $\hat{b}$ are given by

$$\begin{aligned}
\hat{a} &= \hat{a}_n e^{-i\omega_n t} + \hat{a}_{-n} e^{-i\omega_{-n} t}, \\
\hat{b} &= \beta(e^{-i\omega_n t + i\theta_n} + e^{-i\omega_{-n} t + i\theta_{-n}}),
\end{aligned} \tag{7.20}$$

where θ_n and θ_{-n} are the phase differences between the quantum signal and LO at the signal mode and idler mode respectively. Here we assumed that the LO amplitudes are the same at two modes.

In the experiment, the photocurrent is measured with an electrical spectrum analyzer (ESA), which measures the power of the photocurrent. Since in the squeezed vacuum state, the expectation value of the photocurrent is zero, the power of the photocurrent equals to its variance. The variance of the generalized quadrature operator is thus proportional to the ESA measurement of the photocurrent i at different LO phases, which is given by

$$\langle \Delta i(\theta_n, \theta_{-n})^2 \rangle \propto \alpha^2 \langle (e^{i\theta_n} \hat{a}_n^\dagger + e^{i\theta_{-n}} \hat{a}_{-n}^\dagger + e^{-i\theta_n} \hat{a}_n + e^{-i\theta_{-n}} \hat{a}_{-n})^2 \rangle$$

$$= \alpha^2 \langle e^{i2\theta_n} \hat{a}_n^{\dagger 2} + e^{i(\theta_n + \theta_{-n})} \hat{a}_n^\dagger \hat{a}_{-n}^\dagger + \hat{a}_n^\dagger \hat{a}_n + e^{i(\theta_n - \theta_{-n})} \hat{a}_n^\dagger \hat{a}_{-n}$$

$$+ e^{i(\theta_n + \theta_{-n})} \hat{a}_{-n}^\dagger \hat{a}_n^\dagger + e^{i2\theta_{-n}} \hat{a}_{-n}^{\dagger 2} + e^{i(\theta_{-n} - \theta n)} \hat{a}_{-n}^\dagger \hat{a}_n + \hat{a}_{-n}^\dagger \hat{a}_{-n}$$

$$+ \hat{a}_n \hat{a}_n^\dagger + e^{i(\theta_{-n} - \theta_n)} \hat{a}_n \hat{a}_{-n}^\dagger + e^{-i2\theta_n} \hat{a}_n^2 + e^{-i(\theta n + \theta_{-n})} \hat{a}_n \hat{a}_{-n}$$

$$+ e^{i(\theta_n - \theta_{-n})} \hat{a}_{-n} \hat{a}_n^\dagger + \hat{a}_{-n} \hat{a}_{-n}^\dagger + e^{-i(\theta_n + \theta_{-n})} \hat{a}_{-n} \hat{a}_n + e^{-i2\theta_{-n}} \hat{a}_{-n}^2 \rangle.$$

$$(7.21)$$

With the results from equations (7.3) and (7.10), 8 of the 16 terms in equation (7.21) are zero and (7.21) in the frequency domain becomes,

$$\langle \Delta i(\omega, \theta_n, \theta_{-n})^2 \rangle \propto \alpha^2 \langle (e^{i\theta_n} \hat{\tilde{a}}_{out,n}^\dagger + e^{i\theta_{-n}} \hat{\tilde{a}}_{out,-n}^\dagger + e^{-i\theta_n} \hat{\tilde{a}}_{out,n} + e^{-i\theta_{-n}} \hat{\tilde{a}}_{out,-n})^2 \rangle$$

$$= \alpha^2 \langle \hat{\tilde{a}}_{out,n} \hat{\tilde{a}}_{out,n}^\dagger + e^{-i(\theta_n + \theta_{-n})} \hat{\tilde{a}}_{out,n} \hat{\tilde{a}}_{out,-n} + \hat{\tilde{a}}_n^\dagger \hat{\tilde{a}}_{out,n}$$

$$+ e^{i(\theta_n + \theta_{-n})} \hat{\tilde{a}}_{out,n}^\dagger \hat{\tilde{a}}_{out,-n}^\dagger + e^{-i(\theta_n + \theta_{-n})} \hat{\tilde{a}}_{out,-n} \hat{\tilde{a}}_{out,n}$$

$$+ \hat{\tilde{a}}_{out,-n} \hat{\tilde{a}}_{out,-n}^\dagger + e^{i(\theta_n + \theta_{-n})} \hat{\tilde{a}}_{out,-n}^\dagger \hat{\tilde{a}}_{out,n}^\dagger + \hat{\tilde{a}}_{out,-n}^\dagger \hat{\tilde{a}}_{out,-n} \rangle$$

$$= \langle \Delta i(\omega, \theta_n + \theta_{-n})^2 \rangle.$$

$$(7.22)$$

In both equations (7.21) and (7.22), we used the fact that $(e^{i\theta_n} \hat{a}_n^\dagger + e^{i\theta_{-n}} \hat{a}_{-n}^\dagger + e^{-i\theta_n} \hat{a}_n + e^{-i\theta_{-n}} \hat{a}_{-n})$ and its Fourier transform $(e^{i\theta_n} \hat{\tilde{a}}_{out,n}^\dagger + e^{i\theta_{-n}} \hat{\tilde{a}}_{out,-n}^\dagger + e^{-i\theta_n} \hat{\tilde{a}}_{out,n} + e^{-i\theta_{-n}} \hat{\tilde{a}}_{out,-n})$ are Hermitian. While the time domain expression is always Hermitian, its Fourier transform is only Hermitian in the absence of odd order dispersion terms, because of the rules described in Eq.(7.7). In the cases with odd order dis-
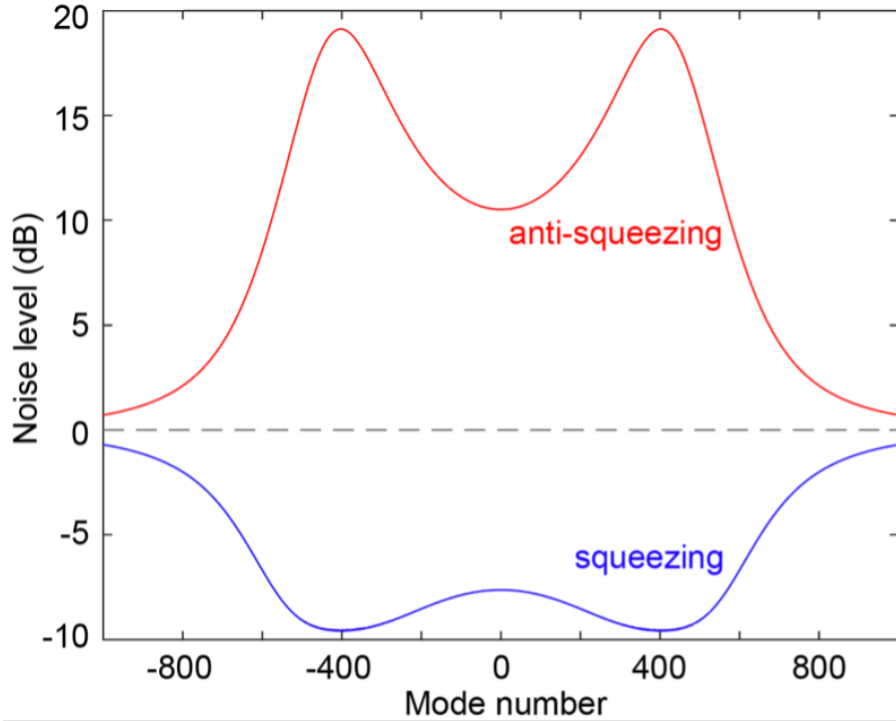
Figure 7.2: **Numerical calculation of squeezing and anti-squeezing versus cavity mode number for a SiN microresonator.** The numerical calculation is based on Eq. (7.10) and Eq. (7.22) by choosing $\theta_1 + \theta_2$ to get the variances of the squeezing and anti-squeezing quadrature operators. Following parameters are used: 10 GHz FSR, dispersion D2/2 $=$ 10 kHz, loaded cavity linewidth of 1 GHz, 90% escape efficiency, pump power that is 1 dB below the parametric oscillation threshold, and no optical loss.

person terms, the ESA measuurement of the photocurrent should be calculated by multiplying the operators with their Hermitian conjugates and follow Eq.(7.7).

It should be noted that $\langle \Delta i^2 \rangle$ is not sensitive to the relative phase $\theta_n - \theta_{-n}$ between the two local oscillators. It only depends on the sum of their phases $\theta_n + \theta_{-n}$. Thus the noise spectrum measurement can only identify squeezing/anti-squeezing, but cannot distinguish if the squeezing belongs to $\hat{x}_n - \hat{x}_{-n}$ or $\hat{p}_n + \hat{p}_{-n}$. Squeezing and anti-squeezing values with different parameters can be numerically calculated by substituting Eq. (7.10) in to Eq. (7.22).

7.2.4   Effect of optical loss and phase noise

Factors such as optical loss and phase noise will directly affect the amount of squeezing detected. The effect of optical loss can be calculated in a beam splitter model, where the quantum signal couples in from one of the paths and vacuum state couples in from the other path. The generalized quadrature operator with optical loss $\hat{A}_{\theta,detected}$ is given by,

$$\hat{A}_{\theta,detected} = \sqrt{\eta}\hat{A}_\theta + \sqrt{1-\eta}\hat{A}_{vacuum}, \tag{7.23}$$

where η is the optical power detection efficiency, i.e. the percentage of optical power detected after optical losses, $\hat{A}_\theta$ is the generalized quadrature operator of the quantum signal and $\hat{A}_{vacuum}$ is the generalized quadrature operator of the vacuum state. The variance of the generalized quadrature operator can be obtained as,

$$\Delta\hat{A}_{\theta,detected} = \eta\Delta\hat{A}_\theta + (1-\eta), \tag{7.24}$$

where we have normalized the variance of the quadrature operators in a vacuum state to 1. This equation shows that any optical loss will degrade the squeezing level. Optical loss includes factors like insertion loss, reflection, absorption, mode mismatch and photo detection efficiency. Since the squeezing is smaller than 1 and anti-squeezing is usually much larger than 1, compared to the anti-squeezing level, the squeezing level is more prone to optical loss.

Phase noise on the other hand doesn't change the optical field physically, but will affect the detection of the quantum signal. The effect of the phase noise can be understood as an averaging between the squeezing and anti-squeezing. Balanced

homodyne detection measures the linearly amplified generalized quadrature operator. With the presence of phase noise, the detected generalized quadrature operator can be written as

$$\hat{N}_+ - \hat{N}_- = \sqrt{2}|\beta| \left[\hat{Q}cos(\theta + \phi(t)) + \hat{P}sin(\theta + \phi(t)) \right], \qquad (7.25)$$

where $\phi(t)$ is the phase noise term which acts as a jitter in the total phase. Assume $\hat{Q}$ is the squeezed quadrature. Because of this phase jitter, when the squeezed quadrature $\hat{Q}$ is supposed to be detected with $\theta = 0$, a fraction of $\hat{P}$ is coupled into this detection,

$$(\hat{N}_+ - \hat{N}_-)_{\theta=0} = \sqrt{2}\beta \left[\hat{Q}cos(\phi(t)) + \hat{P}sin(\phi(t)) \right]. \qquad (7.26)$$

The variance of this detection is given by,

$$\begin{aligned} \Delta\hat{A}_{\theta=0} &\propto \langle \left[\hat{Q}cos(\phi(t)) + \hat{P}sin(\phi(t)) \right]^\dagger \left[\hat{Q}cos(\phi(t)) + \hat{P}sin(\phi(t)) \right] \rangle \\ &= \Delta\hat{Q}cos^2(\delta\phi) + \Delta\hat{P}sin^2(\delta\phi) \end{aligned} \qquad (7.27)$$

where $\delta\phi = \sqrt{\langle\phi(t)^2\rangle}$ is the root mean square phase jitter which can be achieved by calculating the area under the curve in the power spectral density plot of the phase noise. By taking time average, cross terms in the last equation go to zero. The result is equivalent to coupling anti-squeezing to squeezing. Larger the phase jitter and anti-squeezing level, larger the effect of phase noise degrades the squeezing level detected.

Optical loss changes the annihilation operator of the optical field, and phase noise

affects how this optical field is being detected. Therefore, in the case when both optical loss and phase noise are taken into account, we should apply the effect of optical loss before applying the effect of phase noise.

7.3 Demonstration of a two-mode squeezed microcomb

In this section, we will introduce the experimental demonstration of a two-mode squeezed microcomb.

7.3.1 Experimental setup

The experimental setup is shown in Fig. 7.3(a). A continuous-wave (cw) laser (New Focus, TLB-6700) at 1550.5 nm is used to drive both the squeezed microcomb and the local oscillators (LOs). For the squeezed microcomb generation, the cw laser is amplified by an erbium-doped fiber amplifier (EDFA) to pump the Kerr microresonator. A fiber-Bragg grating (FBG) filter is used to filter out the amplified spontaneous emission (ASE) noise from the EDFA. The amplified pump laser is then coupled into the microresonator through a single-mode tapered fiber. At the through port of the tapered fiber, another FBG filter is used to separate light at the pump laser wavelength from light at all other wavelengths. The transmitted squeezed microcomb from the FBG is sent to a 50/50 fiber coupler to be combined with the local oscillators for balanced homodyne detection. In the experiment, the Pound–Drever–Hall (PDH) locking technique is used to lock the pump laser frequency to the resonator mode frequency by servo control of the cw laser frequency. This is implemented by phase
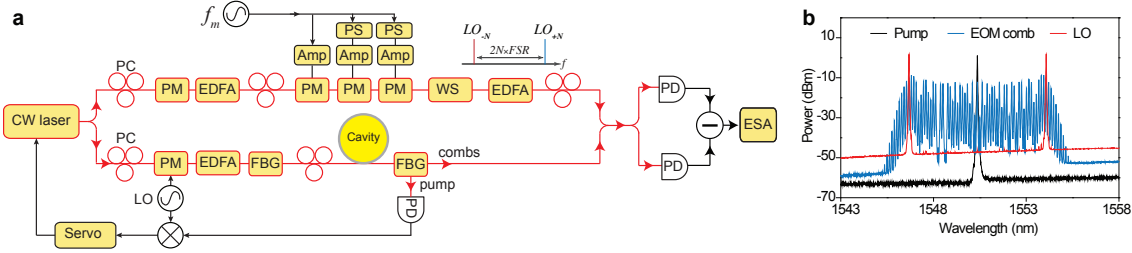
Figure 7.3: **Experimental setup and optical spectrum of local oscillators. (a)** Optical and microwave components are colored in red and black boxes, respectively. A continuous-wave (cw) laser drives both the squeezed microcomb and the local oscillators. Part of the cw laser is amplified by an erbium-doped fiber amplifier (EDFA) to pump the silica microresonator. A fiber-Bragg grating (FBG) filter is used at the microresonator through-port to separate the pump light and the squeezed light. The local oscillators are derived from an electro-optic modulation (EOM) frequency comb, which is driven by the same cw laser. The cw laser is phase modulated by three tandem phase modulators (PMs) at frequency f_m. A programmable waveshaper (WS) is used to select a pair of comb lines to be the local oscillators. The LOs and the squeezed microcomb are combined and detected on the balanced photodetectors (PDs). The noise variance is characterized by an electrical spectrum analyzer (ESA). Polarization controller (PC), electrical amplifier (Amp), and phase shifter (PS) are also included in this figure. **(b)** Optical spectra of the pump laser (black), the EOM frequency comb (blue), and the local oscillators (red) for qumodes (-21, 21).

modulating the pump laser before the EDFA with an electro-optic phase modulator (PM), and then photodetecting the pump laser after the second FBG filter. The phase modulation frequency is set to 80 MHz, much higher than the resonator linewidth. It should be noted that the Brillouin scattering does not affect the squeezing process in our resonator, as the resonator FSR is designed to be completely out of the Brillouin gain bandwidth [35]. Raman scattering in silica has its peak gain at 13 THz away from the pump, and the peak Raman gain is smaller than the Kerr parametric gain in microresonators with anomalous dispersion[34]. As the optical span of the quantum microcomb is only ± 0.5 THz around the pump, the Raman gain within our microcomb span is only $\sim 2\%$ of the peak Raman gain, and it has a negligible effect in our current experiment (Fig. 7.4).

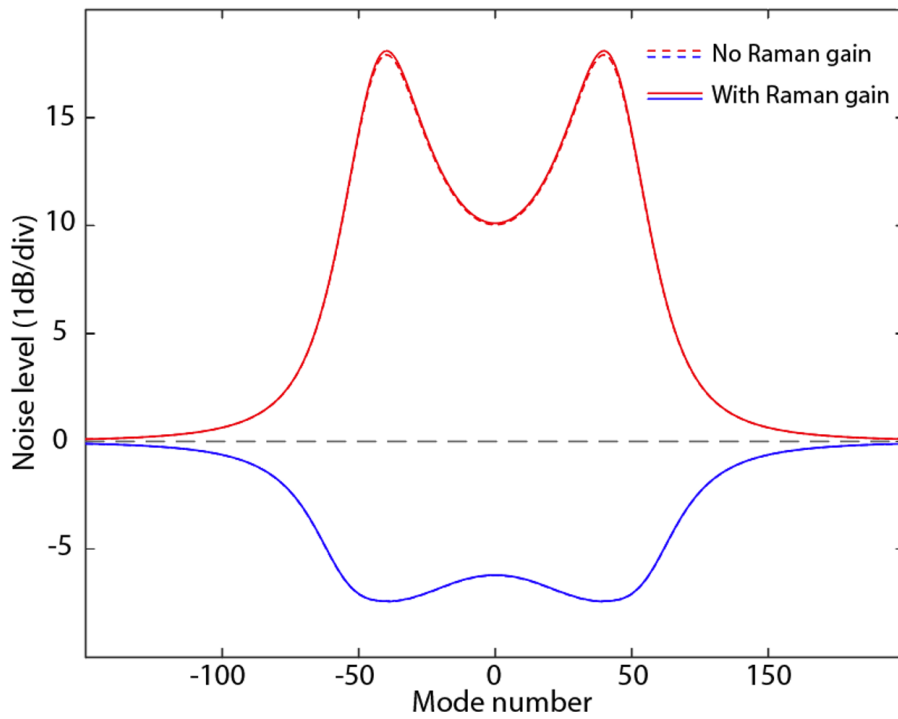Figure 7.4: **Calculation of squeezing level with and without Raman gain.** The numerical calculation is based on solving the quantum Langevin equation Eq. (7.4) with Raman terms $g_R|\alpha_p|^2\delta\hat{a}_n$ and $g_R|\alpha_p|^2\delta\hat{a}_{-n}$ in the second and third equations, where g_R is the Raman gain rate. The calculation uses our silica resonator parameters, 83% escape efficiency and assumes no optical loss.

7.3.2   Squeezed qumode pairs

The quadrature noise variances of 20 sets of comb pairs (40 qumodes) are measured by means of balanced homodyne detection. To measure the quadrature noise variance of qumodes $(-N, N)$, the EOM comb modulation frequency f_m and the programmable waveshaper are adjusted to precisely match the frequencies of LO pairs to $\omega_p \pm N \times D_1$, where N is the relative mode number from the mode being pump ($N = 0$), and $D_1/2\pi = 21.95258$ GHz is the FSR of the resonator at 1550.5 nm wavelength. In each measurement, the phase of the LOs is ramped to yield varying quadrature variances. Figure 7.5(b) shows a representative quadrature noise variance (blue) relative to the shot noise (red) for qumodes (-4,4). A 30-point moving average is used to smooth out the fluctuations in the noise variance measurement. The raw squeezing of 1.6 $\pm$ 0.2 dB and anti-squeezing of 5.5 $\pm$ 0.1 dB are directly observed, and they are obtained by averaging the displayed extrema. The uncertainty is concluded with a 95% confidence interval under t-distribution. The quadrature noise variances of all 40 qumodes are shown in Fig. 7.5(c), and squeezing/anti-squeezing are observed for all 40 qumodes. The number of measurable qumodes is limited by the 1 THz optical span of the EOM comb. All measurements are taken at 2.7 MHz frequency, 100 kHz resolution bandwidth, and 100 Hz video bandwidth on an electrical spectrum analyzer (ESA). The noise levels of qumodes (-1,1) to (-3,3) are not presented here as their measurements are affected by the transmitted ASE noise from the EDFA near the pump frequency. This can be addressed in the future by using a filter with bandwidth much smaller than the FSR of the resonator, or by increasing the intrinsic quality factor of the cavity and reducing the parametric oscillation threshold to eliminate the need for the EDFA. Finally, as shown in Fig. 7.5(d), no quantum correlation (two-mode squeezing) is observed for uncorrelated comb pairs. This serves as a critical

check for our two-tone homodyne detection.

The raw squeezing and anti-squeezing levels of all 40 qumodes are summarized in Fig. 7.6(a). The raw squeezing in our experiment is primarily limited by the 83% cavity escape efficiency, 1.7 dB optical loss, and approximately 89% photodiode quantum efficiency. The total efficiency after the tapered fiber is 60%. Our 1.6 $\pm$0.2 dB raw squeezing is among the highest raw squeezing measured for miniaturized Kerr optical parametric oscillators (OPOs)[29], while the highest squeezing ever achieved is 15 dB in a bulk $\chi^{(2)}$ OPO[176]. 6 dB single-mode squeezing was reported earlier in an integrated waveguide [171], which indicates that high squeezing is possible in integrated photonic platforms. Recent theoretical studies have suggested that quantum error correction and fault-tolerant quantum computing is possible in photonic CV-based approaches [148] when squeezing reaches 10 dB[177].

The anti-squeezing levels near qumodes (-10,10), and from (-17,17) to (-23,23) are observed to be smaller than that of other qumodes. It is caused by to the best of our knowledge the spatial-mode interaction between different transverse mode families in the resonator, which not only modifies local dispersion[178] but provides a path to dissipate optical fields from the squeeze-generating mode to another spatial mode[58]. The spatial-mode-interaction can be identified by measuring the frequency spectrum of a resonator. The relative mode frequencies of the resonator, $\Delta\omega_N = \omega_N - \omega_0 - N \times D_1$, are measured with sideband spectroscopy method[179] and presented in Fig. 7.6(b), where ω_N is the resonance frequency of relative mode number N. An avoided mode crossing[178] was found near mode -8, and resonance frequencies below mode -18 and above mode 19 are observed to change abruptly. These are caused by the spatial-mode interaction and hybridization between two transverse cavity modes. The mode numbers that are affected by spatial-mode-interaction in the mode spectrum coarsely
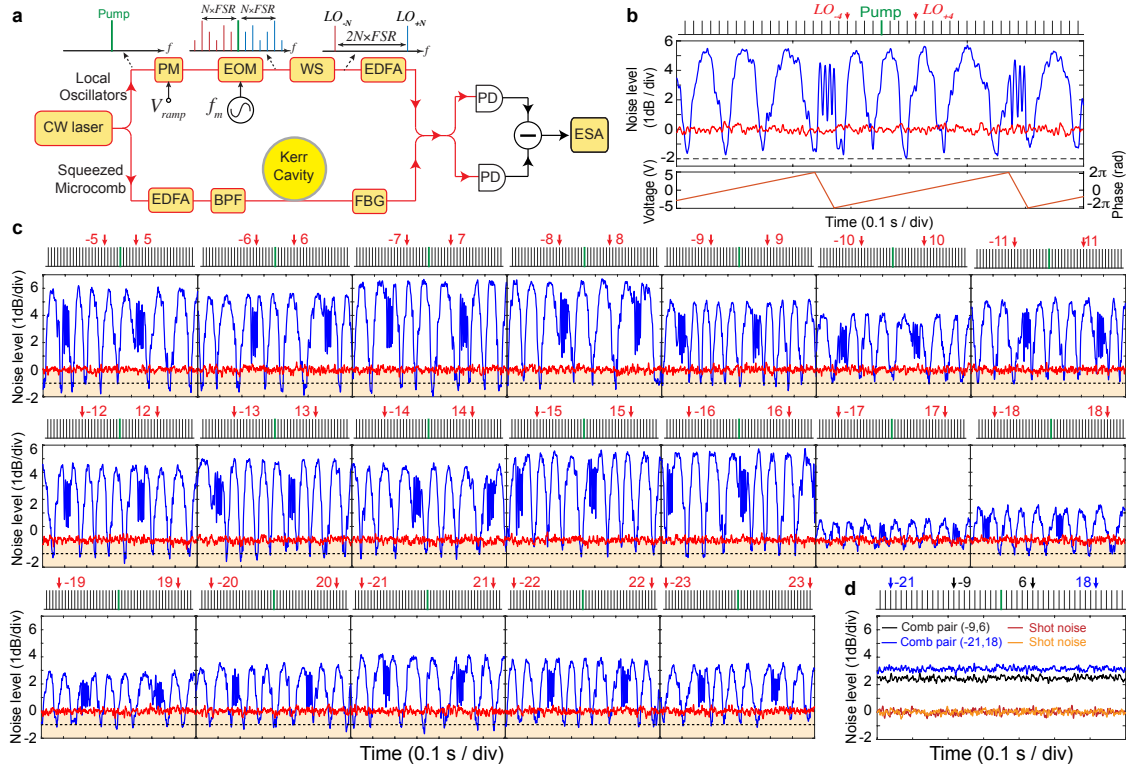
Figure 7.5: **(a)** Simplified experimental schematic. A continuous-wave (cw) laser is split to pump the resonator and drive the local oscillators (LOs). The LOs are derived from an electro-optic modulation (EOM) frequency comb, with a comb spacing (modulation frequency) of f_m. A line-by-line waveshaper (WS) is used to select a pair of comb lines as the bichromatic local oscillators. The phase of the LOs can be tuned by a phase modulator (PM). The LOs and the squeezed microcombs are combined by a 50/50 coupler and are detected on balanced photodiodes (PDs). The noise level is characterized on an electrical spectrum analyzer (ESA). In the squeezed microcomb path, a fiber Bragg grating (FBG) filter is used to block the strong pump light. Erbium-doped fiber amplifiers (EDFAs) and optical bandpass filter (BPF) are also shown in the figure. **(b)** Representative quadrature noise variance (blue) relative to shot noise (red) as a function of time for qumodes -4 and 4 (indicated with red arrows). The lower panel illustrates the ramp waveform applied to the phase modulator to ramp the phase of the LOs periodically with time. 1.6 dB squeezing and 5.5 dB anti-squeezing are directly observed. A dashed black line indicates 2 dB below shot noise level. **(c)** Quadrature noise variance (blue) relative to shot noise (red) of all 40 qumodes. The qumodes measured are marked by the red arrows. The regime below the shot noise limit is colored in orange, and a dashed black line indicates 1 dB below the shot noise level. (d) Quantum correlation check: noise variances show no quantum correlation between uncorrelated comb pairs for qumodes (-9, 6) and (-21, 18). All measurements are taken at 2.7 MHz frequency, 100 kHz resolution bandwidth, and 100 Hz video bandwidth.
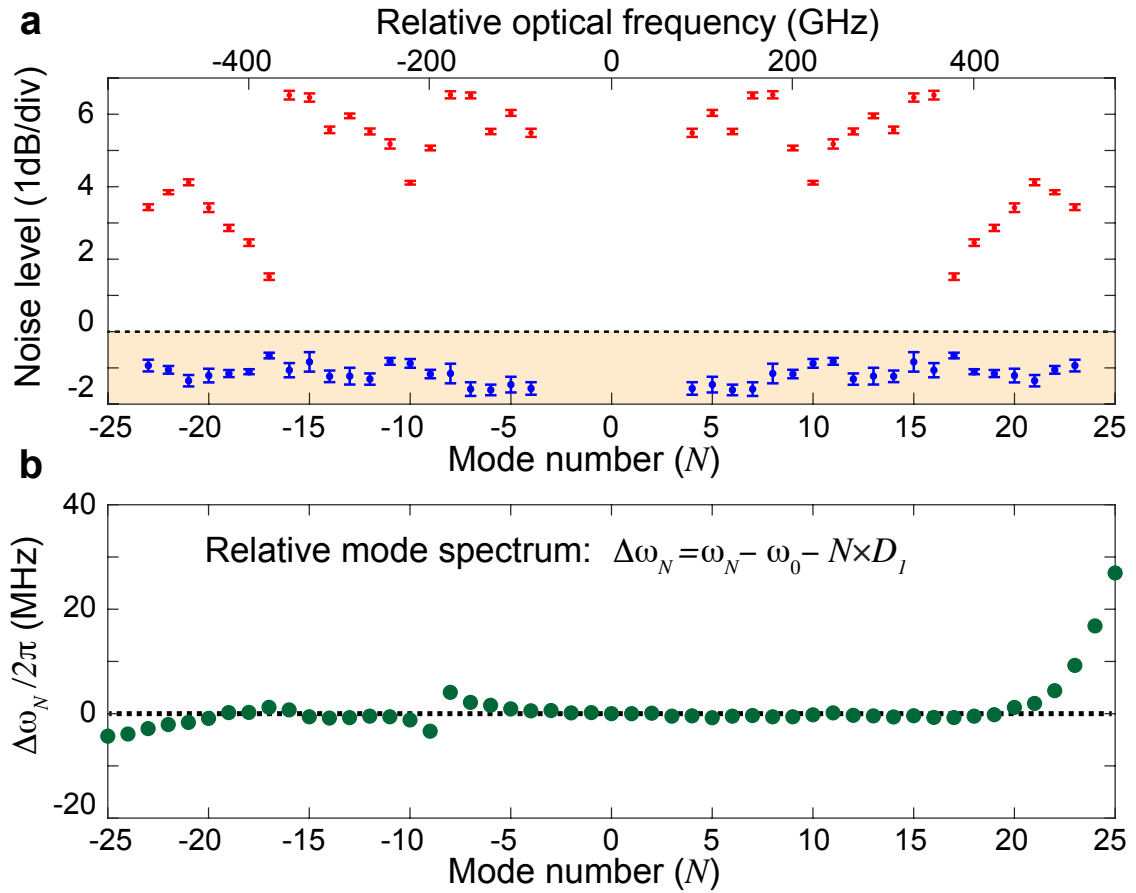
Figure 7.6: **Summary of squeezing and anti-squeezing levels and resonator mode spectrum.** **(a)** Squeezing (blue) and anti-squeezing (red) levels versus mode number. The regime below the shot noise level is colored in orange. It should be noted that the noise level at qumode N or $-N$ represents the two-mode noise level of comb pair $(-N, N)$. The error bars are concluded with a 95% confidence interval under t-distribution. **(b)** The cold resonator mode spectrum ($\Delta\omega_N$, relative mode frequency). The degradation of squeezing/anti-squeezing level of certain qumodes is likely caused by the avoided mode crossing induced by spatial-mode-interaction in the microresonator.

align with that of the dips in anti-squeezing measurement. We have performed more systematic studies both in theory and experiments to understand the mechanism of how the cavity mode dispersion affects squeezing and anti-squeezing, which will be in the future publications. Finally, the impact of spatial-mode interaction can be eliminated in the future by using a microresonator with a single transverse mode family [180, 69] and the dispersion can be tailored through dispersion engineering introduced in Chapter 3.

7.3.3 Characterization of the bichromatic local oscillators

The local oscillators in this experiment are derived from an electro-optic modulation (EOM) frequency comb [181]. The EOM comb is convenient to create coherent local oscillators which are hundreds of GHz apart from the pump laser frequency. In our EOM comb, the cw laser is amplified by an EDFA to 200 mW and is phase modulated by three cascaded electro-optic phase modulators at frequency f_m, which is provided by a signal generator (Keysight, PSG E8257D). The modulators are driven by amplified electrical signals that are synchronized by electrical phase shifters (PSs). The output power of the electrical amplifiers (Amps) is $\sim$ 33 dBm. As the EOM comb and the microresonator share the same pump laser, the local oscillators derived from the EOM comb are inherently coherent with the squeezed microcomb. A typical EOM comb spectrum is shown in Fig. 7.3(b) (blue line), and the cw pump laser spectrum (black) is also shown as a reference. The EOM comb is then sent to a programmable line-by-line waveshaper (Finisar 1000A, filter bandwidth setting resolution: ±5 GHz), which can control the amplitude and phase of each EOM comb line. To measure the noise variance of qumodes $(-N, N)$, the waveshaper is set to only pass the comb lines whose frequencies are $\pm N \times$FSR apart from the pump

laser. As an example, the local oscillators for qumodes (-21,21) are shown in Fig. 7.3(b) (red line). Finally, the LOs are amplified to ~ 17 mW and are combined with the squeezed microcomb for balanced homodyne detection. It should be noted that the relative phase between the local oscillator and the squeezed field could be different from the phase shift applied by the PM in the LO optical path. This is because environmental fluctuations, e.g., ambient temperature, can cause phase variations in fibers in both LO and squeezed light paths. Finally, the electrical amplifiers in the EOM comb cut off at 18 GHz, which is smaller than the FSR of the resonator (represented by f_r). As a result, the EOM modulation frequency, f_m, is set to $n/m \times f_r$, such that the frequency of the m-th EOM comb line can align with that of the n-th resonator mode. The modulation frequencies used in the experiment are: $f_m = 3/4 \times f_r = 16.464438$ GHz for mode pairs $\pm 6, \pm 9, \pm 12, \pm 15, \pm 18, \pm 21$; $f_m = 2/3 \times f_r = 14.635056$ GHz for mode pairs $\pm 4, \pm 8, \pm 14, \pm 16, \pm 20$. For mode pairs of $\pm 5, \pm 7, \pm 11, \pm 13, \pm 17, \pm 19, \pm 22, \pm 23$, modulation frequencies of: $5/7 \times f_r = 15.680417$ GHz, $7/9 \times f_r = 17.074232$ GHz, $11/15 \times f_r = 16.098562$ GHz, $13/17 \times f_r = 16.787270$ GHz, $17/23 \times f_r = 16.225823$ GHz, $19/25 \times f_r = 16.683964$ GHz, $22/29 \times f_r = 16.653684$ GHz, and $23/29 \times f_r = 17.410670$ GHz are used, respectively.

The phase noise of the signal generator that drives the EOM comb contributes to the phase fluctuation of the local oscillator, which could potentially affect squeezing measurement [182]. Here, we estimate its impact on our experiments. The root mean square (RMS) of phase jitter from the signal generator can be calculated from its single-sideband (SSB) phase noise by integrating the phase noise from the electrical spectrum analyzer (ESA) video bandwidth (VBW) used in the squeezing measurement (100 Hz), to the bandwidth of our balanced photodetection circuit (250 MHz). The RMS of phase jitter $(\widetilde{\theta})$ is calculated to be 0.0024 rad (0.14°) for comb
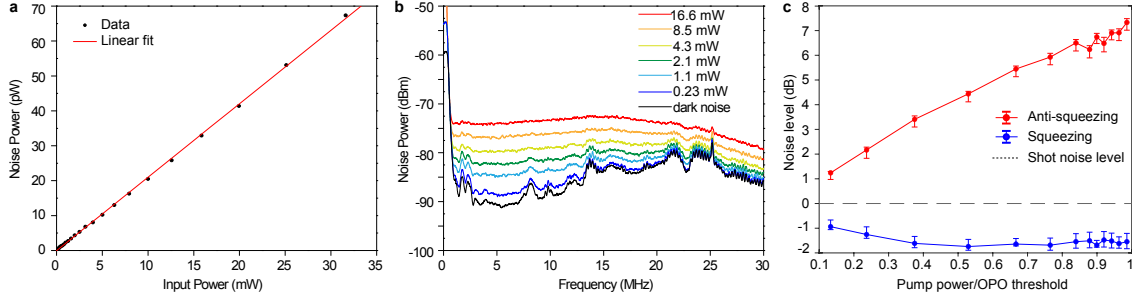
112

Figure 7.7: **(a)** Noise power vs. the optical power of local oscillators sent into the PDs. The noise power is measured at 2.7 MHz frequency, and the dark noise from the PDs has been subtracted from the noise power. The linear trend indicates the balanced photodiodes are operated in the shot noise-limited regime. **(b)** Electrical spectra of the balanced PD outputs at different local oscillator powers. All measurements in this figure are taken at 100 kHz resolution bandwidth. **(c)** Measurement of squeezing and anti-squeezing versus pump power for qumode (-4,4). The error bars are concluded with a 95% confidence interval under t-distribution.

mode 1 ($\sim$ 22 GHz), and is 0.055 rad (3.2°) for comb mode 23 ($\sim$ 0.5 THz). After taking account of this phase fluctuation, the observable level of squeezing[182] is $R'_{\mathrm{S}} \approx R_{\mathrm{S}} \cos^2 \widetilde{\theta} + R_{\mathrm{AS}} \sin^2 \widetilde{\theta}$, where R_{S} and R_{AS} are the variance of output squeezing and anti-squeezing, respectively. For the current experimental condition, assuming 2 (7) dB squeezing (anti-squeezing) at mode 4, and 1 (5) dB squeezing (anti-squeezing) at mode 23 after optical losses, the phase fluctuation will cause the measured squeezing (R'_{S}) to be 0.003 dB and 0.04 dB lower than the actual squeezing (R_{S}) at mode 4 and mode 23, respectively. It should be noted that the N-th comb line in the EOM comb has N times the RMS phase jitter of the 1st comb line in the EOM comb. Therefore, when scaling up the number of comb lines in an EOM comb through supercontinuum generation[183] for squeezing measurement, the phase noise of the signal generator should be improved accordingly to maintain the low phase fluctuation of the local oscillators. A possible way to obtain exceptional phase noise performance for the EOM comb is through electro-optical frequency division, where the signal generator is synchronized to stable optical references[78].

7.3.4 Characterization of the balanced PD

In the two-mode squeezing noise variance measurement, the balanced photodiodes (JDSU, ETX 300T) are operated in the shot noise limited regime. The electrical circuit for balancing the photodiodes is home-built[139], and a common-mode rejection ratio of 31 dB is measured. The shot noise limited regime is verified by the linear relationship between the noise power of the balanced photodiodes and the optical input power, which is shown in Fig. 7.7(a). The measurement is done at 2.7 MHz with 100 kHz resolution bandwidth (RBW). The electrical spectra from the balanced photodiodes at different optical input powers are shown in Fig. 7.7(b). The resonance peaks in the dark noise are likely caused by the electrical circuits in the balanced photodiodes. At 16.6 mW input power, the electrical spectrum is relatively flat. The spectra roll-off is around 20 MHz.

7.3.5 Dependence of squeezing on optical pump power

The dependence of squeezing and anti-squeezing on optical pump power is measured for qumode (-4,4) and is presented in Fig. 7.7(c). Ideally, when there is no optical loss, vacuum squeezing should increase with the pump power until the pump power reaches the OPO threshold. However, as the amount of squeezing in our experiment is primarily limited by optical losses, the increase of squeezing can no longer be observed when the pump power is roughly above half of the OPO threshold. On the other hand, the anti-squeezing increases with the pump power. This observation is consistent with measurements in previous reports[28].

7.3.6 Improvement to the original two-mode squeezed micro-comb

By improving the detection efficiency such as reducing the optical loss and increasing the quantum efficiency of the photodiodes, we can further increase the amount of squeezing detected. Also with a narrow bandpass filter before the cavity, it enables the measurements on qumode pairs $(-3, 3)$ nad $(-2, 2)$.

We generated two-mode squeezed states in the same microresonator with the improved experimental setup. The resonator is overcoupled to achieve large escape efficiency of 82%. The pump power is set to 112 mW, which is below the parametric threshold of 144 mW. The quadrature noise variances of 22 comb pairs (44 qumodes) are shown in Fig. 7.8. A maximum raw squeezing of 2.1 dB and maximum anti-squeezing of 6 dB are obtained for mode $(-4, 4)$ by averaging the displayed extrema. The squeezing levels in all other modes are improved to above 1 dB. The raw squeezing value in our experiment is primarily limited by the 82% cavity escape efficiency, 1.3 dB optical loss, and approximately 95% photodiode quantum efficiency. The total efficiency after the tapered fiber is 70%. A corresponding 3.4 dB squeezing at the output waveguide can be inferred after correcting system losses. The number of measurable qumodes is limited by the 1 THz optical span of the EOM comb.

7.4 Spectroscopy characterization of the squeezed microcomb

In this section, we will introduce a qumode spectroscopy method to characterize the frequency equidistance of squeezed qumodes, a prerequisite of frequency combs.
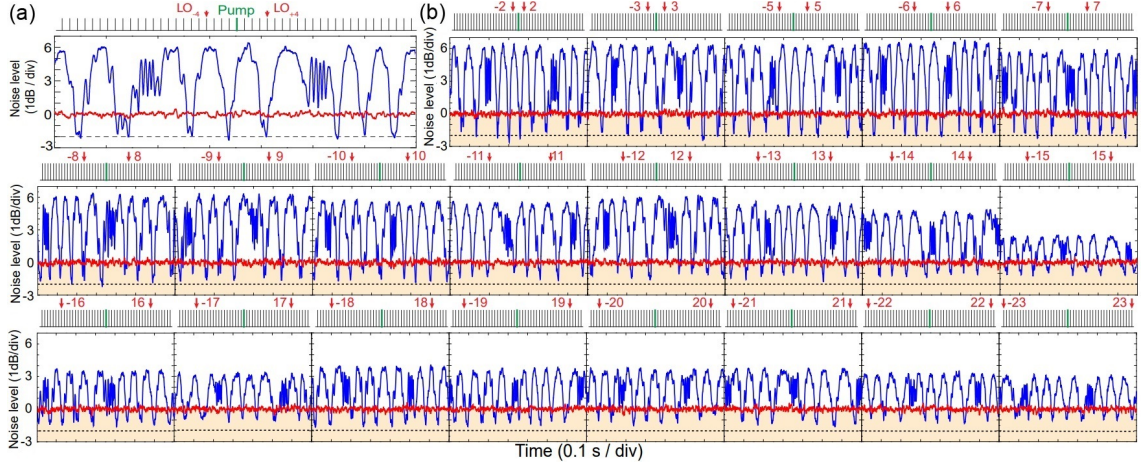
Figure 7.8: **A squeezed microcomb with improved experimental setup.**
(a) Representative quadrature noise variance (blue) relative to shot noise (red) for
qumodes -4 and 4. **(b)** Quadrature noise variance (blue) relative to shot noise (red)
of other 21 qumode pairs.

Similar to the classical cavity mode spectrum, we can define the relative qumode
spectrum as $\Delta\omega_N^Q = \omega_N^Q - \omega_0 - N \times D_1$, where ω_N^Q is the optical frequency center of
the N-th qumode. The relative qumode spectrum represents the qumode frequency
deviation from equidistance. To identify the relative qumode spectrum, the two-sided
squeezing/anti-squeezing spectral line shape is measured for each pair of qumodes, and
the center frequency of the spectral line shape yields the relative qumode frequency. In
the measurement, the $\pm N$-th LO frequencies are detuned by $\pm\delta$ from the equidistant
frequencies, $\pm N\times$FSR, and noise variances are measured at each detuning point
for qumodes $(-N,N)$. For each pair of qumodes, the detuning (δ) is varied from -
30 MHz to + 30 MHz with an interval of 5 MHz, which sets the resolution of the
line shape measurement. Measurements of qumodes (-4,4) at $\delta = -20, -10, 0, 10, 20$
MHz are shown as examples in Fig. 7.9(b). At each detuning point, squeezing
and anti-squeezing levels can be extracted by averaging the extrema. We plot the
squeezing/anti-squeezing levels versus detuning (δ) for all qumodes in Fig. 7.9(c),
which manifest the two-sided spectral line shape of the qumodes. The squeezing/anti-

squeezing extraction below 0.5 dB has relatively poor accuracy, but this does not affect the overall qumode spectrum envelopes.

The relative frequencies of the qumodes, i.e., relative qumode spectrum, can be obtained by identifying the centers of the anti-squeezing line shapes via Lorentzian fitting. The average root mean square deviation of the fitting is only 0.15 dB, showing an excellent agreement between fitting and measurements. $\Delta\omega_N^Q$ of all the qumodes are plotted in Fig. 7.9(d), and their deviations from equidistant are within the 5 MHz spectroscopy resolution limit for the entire 1 THz optical span of the quantum microcomb. The qumode spectrum overlaps well with the two-sided averaged cold cavity mode spectrum, $-(\Delta\omega_N + \Delta\omega_{-N})/2$ (will be discussed in the next section), which represents the averaged deviation from equidistant of the cold cavity mode N and $-N$. It should be noted that in the qumode spectrum measurement, the cavity is pumped by > 100 mW power, which could alter the cavity mode spectrum through thermo-optic effect and self/cross-phase modulation effects. Further study in the future is necessary to understand the requirement for perfectly equidistant frequencies of qumodes. In this measurement, the cavity escape efficiency is adjusted to 77% to achieve a more stable coupling condition as the entire measurement spans over 18 hours. As a result, the amount of squeezing/anti-squeezing at $\delta = 0$ MHz is different from that in the Fig. 7.5. In this experiment, the escape efficiency is adjusted by varying the relative position between the microresonator and the tapered fiber[184]. The stability of the escape efficiency can be dramatically improved by packaging the microresonator systems[185], or by integrating the coupling waveguide and the resonator on the same chip[69].
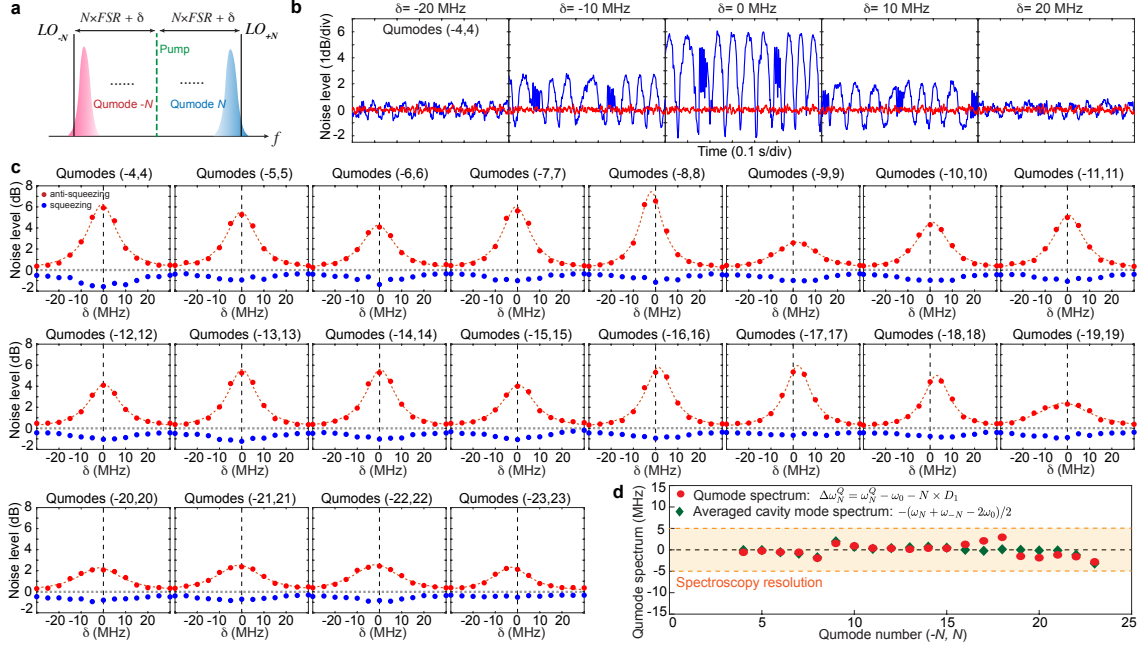
Figure 7.9: **Spectroscopy characterization of qumodes in the squeezed quantum microcomb. (a)** Illustration of spectroscopy measurement of qumode (-N,N). The frequencies of the N-th LOs can be detuned by δ away from the equidistant frequencies, $\pm N \times$FSR, and the amount of squeezing and anti-squeezing are measured at each detuning point, δ. **(b)** Noise variance measurement of qumodes (-4,4) at detuning δ = -20, -10, 0, 10, 20 MHz. The red trace represents shot noise level. **(c)** Squeezing (blue) and anti-squeezing (red) levels extracted from noise variance measurements at different detuning points (δ) for all qumodes. Shot noise levels are represented by the horizontal dashed gray lines. Lorentzian fitting of the anti-squeezing spectrum (red dash line) is used to find the qumode center frequencies. Vertical dashed black lines represent the equidistant frequencies for each qumodes. **(d)** Summary of the measured relative qumode frequencies (red) from qumodes (-3,3) to (-23,23). The two-sided averaged cavity mode spectrum: -($\Delta\omega_N$ + $\Delta\omega_{-N}$)/2 is plotted in green and it agrees well with the qumode spectrum.

7.4.1 Mode spectrum measurement of a hot cavity

To study the relation between qumode spectrum and cavity mode spectrum, it is necessary to measure the hot cavity mode spectrum which can be realized by counter propagating pumps. Shown in Fig. 7.10, an auxiliary laser (pump 2) is used to heat up the cavity on the counter propagating direction. Pump 1 is the probe pump that is used to detect the cavity modes. Pump 1 has a small enough power to avoid additional thermal effect. When performing the hot cavity measurement, pump 2 is locked to the dip of one of the cavity modes, and is shifted one FSR away from the probe laser pump 1 to avoid the interference from the reflected light. Then regular mode spectrum measurement can be perform using the probe laser pump 1 with either the wavelength sweep method or EOM method introduced in Chapter 3 Section 3.4. The theory (Eq. (7.2) with higher orders of dispersion) and measurements of squeezing along with hot cavity mode spectrum suggest that the center of the qumodes are determined by $(\Delta\omega_N - \Delta\omega_{-N})/2$. Therefore only odd orders of dispersion will shift the center of the qumodes. The even orders of dispersion will affect the amount of squeezing generated. More studies and investigations will be presented in the future publications.

7.5 Summary

In this chapter, we introduced the basic theories of a two-mode squeezed microcomb as well as the experiment demonstration. The generation of squeezed microcomb is not limited to Kerr microresonators, but can also be realized in microresonator-based $\chi^{(2)}$ parametric oscillators [186, 187, 188, 189]. For our system, the raw squeezing can be improved in the future by reducing system losses, improving photodiode quantum
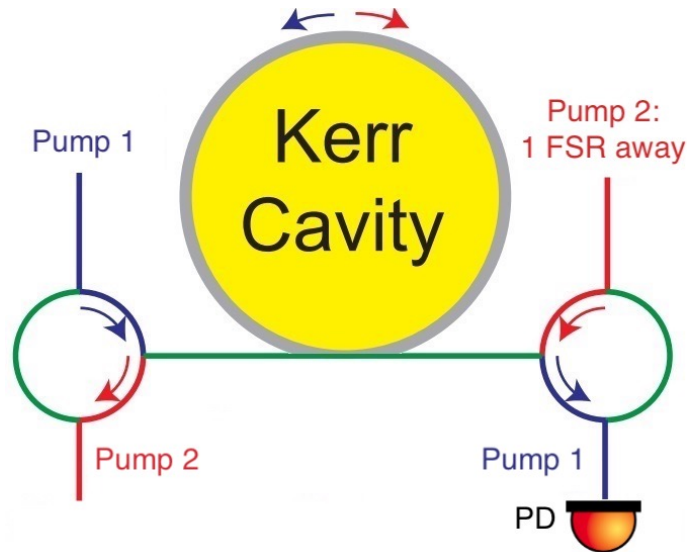
Figure 7.10: **Counter propagating pumps to measure hot cavity mode spectrum.** Pump 1 is the probe laser that has a small enough power that doesn't introduce thermal effect in the cavity. Pump 2 is the auxiliary laser that has a large enough power to heat up the cavity.

efficiency, and achieving higher resonator-waveguide escape efficiency. The number of measurable qumodes, 40, is primarily limited by the span of the local oscillator, and this could be dramatically increased in the future by spectrum broadening of the EOM comb [183], or by using broadband dissipative Kerr soliton microcombs[10] as the local oscillators. The optical span of quantum microcombs will ultimately be limited by the microresonator dispersion, which sets the bandwidth of Kerr parametric gain. Through dispersion engineering, Kerr parametric sidebands that are $\sim \pm 80$ THz away from the pump frequency have been reported in microresonators[190], which indicates the possibility of creating hundreds or thousands of qumodes in a single microresonator. The miniaturization of deterministic quantum frequency combs provides a path towards mass production, which could be critical for applications in quantum computing, quantum metrology, and quantum sensing[191, 192].

Bibliography

[1]   John L Hall. "Nobel Lecture: Defining and measuring optical frequencies". In: *Reviews of modern physics* 78.4 (2006), p. 1279.

[2]   Theodor W Hänsch. "Nobel lecture: passion for precision". In: *Reviews of Modern Physics* 78.4 (2006), p. 1297.

[3]   Th Udem, Ronald Holzwarth, and Theodor W Hänsch. "Optical frequency metrology". In: *Nature* 416.6877 (2002), pp. 233–237.

[4]   SA Diddams et al. "Standards of time and frequency at the outset of the 21st century". In: *Science* 306.5700 (2004), pp. 1318–1324.

[5]   Nathan R Newbury. "Searching for applications with a fine-tooth comb". In: *Nat. Photon.* 5.4 (2011), pp. 186–188.

[6]   P Del'Haye et al. "Optical frequency comb generation from a monolithic microresonator". In: *Nature* 450.7173 (2007), pp. 1214–1217.

[7]   Tobias J Kippenberg, Ronald Holzwarth, and SA Diddams. "Microresonator-based optical frequency combs". In: *Science* 332.6029 (2011), pp. 555–559.

[8]   François Leo et al. "Temporal cavity solitons in one-dimensional Kerr media as bits in an all-optical buffer". In: *Nat. Photon.* 4.7 (2010), pp. 471–476.

[9]   T Herr et al. "Temporal solitons in optical microresonators". In: *Nat. Photon.* 8.2 (2014), pp. 145–152.

[10]   Tobias J Kippenberg et al. "Dissipative Kerr solitons in optical microresonators". In: *Science* 361.6402 (2018), eaan8083.

[11]   Alexander L Gaeta, Michal Lipson, and Tobias J Kippenberg. "Photonic-chip-based frequency combs". In: *nature photonics* 13.3 (2019), pp. 158–169.

[12]   Daryl T Spencer et al. "An optical-frequency synthesizer using integrated photonics." In: *Nature* 557.7703 (2018), pp. 81–85.

[13]   Myoung-Gyun Suh et al. "Microresonator soliton dual-comb spectroscopy". In: *Science* 354.6312 (2016), pp. 600–603.

[14]   Yanne K Chembo. "Quantum dynamics of Kerr optical frequency combs below and above threshold: Spontaneous four-wave mixing, entanglement, and squeezed states of light". In: *Physical Review A* 93.3 (2016), p. 033820.

[15]   Christian Reimer et al. "Generation of multiphoton entangled quantum states by means of integrated frequency combs". In: *Science* 351.6278 (2016), pp. 1176–1180.

[16]   Michael Kues et al. "On-chip generation of high-dimensional entangled quantum states and their coherent control". In: *Nature* 546.7660 (2017), pp. 622–626.

[17]   Poolad Imany et al. "50-GHz-spaced comb of high-dimensional frequency-bin entangled photons from an on-chip silicon nitride microresonator". In: *Optics express* 26.2 (2018), pp. 1825–1840.

[18]   Michael Kues et al. "Quantum optical microcombs". In: *Nature Photonics* 13.3 (2019), pp. 170–179.

[19]   Melissa A Guidry et al. "Quantum optics of soliton microcombs". In: *arXiv preprint arXiv:2103.10517* (2021).

[20]   NG Pavlov et al. "Soliton dual frequency combs in crystalline microresonators". In: *Optics Letters* 42.3 (2017), pp. 514–517.

122

[21] Avik Dutt et al. "On-chip dual-comb source for spectroscopy". In: *Science advances* 4.3 (2018), e1701858.

[22] Chengying Bao, Myoung-Gyun Suh, and Kerry Vahala. "Microresonator soliton dual-comb imaging". In: *Optica* 6.9 (2019), pp. 1110–1116.

[23] Xu Yi et al. "Imaging soliton dynamics in optical microcavities". In: *Nature communications* 9.1 (2018), pp. 1–8.

[24] Myoung-Gyun Suh and Kerry J Vahala. "Soliton microcomb range measurement". In: *Science* 359.6378 (2018), pp. 884–887.

[25] Philipp Trocha et al. "Ultrafast optical ranging using microresonator soliton frequency combs". In: *Science* 359.6378 (2018), pp. 887–891.

[26] Pablo Marin-Palomo et al. "Microresonator-based solitons for massively parallel coherent optical communications". In: *Nature* 546.7657 (2017), pp. 274–279.

[27] Yun Zhao et al. "Near-degenerate quadrature-squeezed vacuum generation on a silicon-nitride chip". In: *Physical Review Letters* 124.19 (2020), p. 193601.

[28] VD Vaidya et al. "Broadband quadrature-squeezed vacuum and nonclassical photon number correlations from a nanophotonic device". In: *Science Advances* 6.39 (2020), eaba9186.

[29] Y Zhang et al. "Squeezed light from a nanophotonic molecule". In: *Nature Communications* 12 (2021), p. 2233.

[30] Zijiao Yang et al. "A squeezed quantum microcomb on a chip". In: *Nature Communications* 12.1 (2021), pp. 1–8.

[31] Kerry J Vahala. "Optical microcavities". In: *Nature* 424.6950 (2003), pp. 839–846.

[32] Lord Rayleigh. "CXII. The problem of the whispering gallery". In: *The London, Edinburgh, and Dublin Philosophical Magazine and Journal of Science* 20.120 (1910), pp. 1001–1004.

[33] RD Richtmyer. "Dielectric resonators". In: *Journal of applied physics* 10.6 (1939), pp. 391–398.

[34] TJ Kippenberg, SM Spillane, and KJ Vahala. "Kerr-nonlinearity optical parametric oscillation in an ultrahigh-Q toroid microcavity". In: *Physical Review Letters* 93.8 (2004), p. 083904.

[35] Hansuek Lee et al. "Chemically etched ultrahigh-Q wedge-resonator on a silicon chip". In: *Nat. Photon.* 6.6 (2012), pp. 369–373.

[36] Hojoong Jung et al. "Optical frequency comb generation from aluminum nitride microring resonator". In: *Opt. Lett.* 38.15 (2013), pp. 2810–2813.

[37] Mian Zhang et al. "Monolithic ultra-high-Q lithium niobate microring resonator". In: *Optica* 4.12 (2017), pp. 1536–1537.

[38] David J Moss et al. "New CMOS-compatible platforms based on silicon nitride and Hydex for nonlinear optics". In: *Nature photonics* 7.8 (2013), pp. 597–607.

[39] Hermann Haus. "Waves and fields in optoelectronics." In: *PRENTICE-HALL, INC., ENGLEWOOD CLIFFS, NJ 07632, USA, 1984, 402* (1984).

[40] T Herr et al. "Universal formation dynamics and noise of Kerr-frequency combs in microresonators". In: *Nat. Photon.* 6.7 (2012), pp. 480–487.

[41] Luigi A Lugiato and René Lefever. "Spatial dissipative structures in passive optical systems". In: *Phys. Rev. Lett.* 58.21 (1987), p. 2209.

[42] AB Matsko et al. "Mode-locked Kerr frequency combs". In: *Opt. Lett.* 36.15 (2011), pp. 2845–2847.

124

[43] Yanne K Chembo and Curtis R Menyuk. "Spatiotemporal Lugiato-Lefever formalism for Kerr-comb generation in whispering-gallery-mode resonators". In: *Phys. Rev. A* 87.5 (2013), p. 053852.

[44] Govind P Agrawal. *Nonlinear fiber optics*. Academic press, 2007.

[45] Yanne K Chembo and Nan Yu. "Modal expansion approach to optical-frequency-comb generation with monolithic whispering-gallery-mode resonators". In: *Physical Review A* 82.3 (2010), p. 033801.

[46] Andrey B Matsko and Lute Maleki. "On timing jitter of mode locked Kerr frequency combs". In: *Opt. Express* 21.23 (2013), pp. 28862–28876.

[47] James W Cooley and John W Tukey. "An algorithm for the machine calculation of complex Fourier series". In: *Mathematics of computation* 19.90 (1965), pp. 297–301.

[48] John M Dudley, Goëry Genty, and Stéphane Coen. "Supercontinuum generation in photonic crystal fiber". In: *Reviews of modern physics* 78.4 (2006), p. 1135.

[49] Yoshitomo Okawachi et al. "Bandwidth shaping of microresonator-based frequency combs via dispersion engineering". In: *Optics letters* 39.12 (2014), pp. 3535–3538.

[50] Johann Riemensberger et al. "Dispersion engineering of thick high-Q silicon nitride ring-resonators via atomic layer deposition". In: *Optics express* 20.25 (2012), pp. 27661–27669.

[51] Victor Brasch et al. "Self-referenced photonic chip soliton Kerr frequency comb". In: *Light: Science & Applications* 6.1 (2017), e16202.

[52]   Yoshitomo Okawachi et al. "Octave-spanning frequency comb generation in a silicon nitride chip". In: *Optics letters* 36.17 (2011), pp. 3398–3400.

[53]   Qi-Fan Yang et al. "Spatial-mode-interaction-induced dispersive-waves and their active tuning in microresonators". In: *Optica* 3 (2016), pp. 1132–1135.

[54]   Yoshitomo Okawachi et al. "Active tuning of dispersive waves in Kerr soliton combs". In: *Optics Letters* 47.9 (2022), pp. 2234–2237.

[55]   Yang Liu et al. "Investigation of mode coupling in normal-dispersion silicon nitride microresonators for Kerr frequency comb generation". In: *Optica* 1.3 (2014), pp. 137–144.

[56]   Hermann A Haus and Weiping P Huang. "Coupled-mode theory". In: *Proceedings of the IEEE* 79.10 (1991), pp. 1505–1518.

[57]   Jan Wiersig. "Formation of long-lived, scarlike modes near avoided resonance crossings in optical microcavities". In: *Phys. Rev. Lett.* 97.25 (2006), p. 253901.

[58]   Xu Yi et al. "Single-mode dispersive waves and soliton microcomb dynamics". In: *Nature Communications* 8 (2017), p. 14869.

[59]   PKA Wai et al. "Nonlinear pulse propagation in the neighborhood of the zero-dispersion wavelength of monomode optical fibers". In: *Opt. Lett.* 11.7 (1986), pp. 464–466.

[60]   Nail Akhmediev and Magnus Karlsson. "Cherenkov radiation emitted by solitons in optical fibers". In: *Phys. Rev. A* 51.3 (1995), p. 2602.

[61]   Changjing Bao et al. "Nonlinear conversion efficiency in Kerr frequency comb generation". In: *Opt. Lett.* 39.21 (2014), pp. 6126–6129.

[62]   Xu Yi et al. "Soliton frequency comb at microwave rates in a high-Q silica microresonator". In: *Optica* 2.12 (2015), pp. 1078–1085.

[63] Pascal Del'Haye et al. "Frequency comb assisted diode laser spectroscopy for measurement of microcavity dispersion". In: *Nature Photonics* 3.9 (2009), pp. 529–533.

[64] N Akhmediev and A Ankiewicz. *Dissipative Solitons: From Optics to Biology and Medicine*. 2008.

[65] Myoung-Gyun Suh and Kerry Vahala. "Gigahertz-repetition-rate soliton microcombs". In: *Optica* 5.1 (2018), pp. 65–66.

[66] Qing Li et al. "Stably accessing octave-spanning microresonator frequency combs in the soliton regime". In: *Optica* 4.2 (2017), pp. 193–203.

[67] Martin HP Pfeiffer et al. "Octave-spanning dissipative Kerr soliton frequency combs in Si_3N_4 microresonators". In: *Optica* 4.7 (2017), pp. 684–691.

[68] Brian Stern et al. "Battery-operated integrated frequency comb generator". In: *Nature* 562.7727 (2018), pp. 401–405.

[69] Ki Youl Yang et al. "Bridging ultrahigh-Q devices and photonic circuits". In: *Nature Photonics* 12.5 (2018), pp. 297–302.

[70] Erwan Lucas et al. "Ultralow-noise photonic microwave synthesis using a soliton microcomb-based transfer oscillator". In: *Nature Communications* 11.1 (2020), pp. 1–8.

[71] Tal Carmon, Lan Yang, and Kerry J Vahala. "Dynamical thermal behavior and thermal self-stability of microcavities". In: *Optics express* 12.20 (2004), pp. 4742–4750.

[72] Jordan R Stone et al. "Thermal and nonlinear dissipative-soliton dynamics in Kerr-microresonator frequency combs". In: *Physical review letters* 121.6 (2018), p. 063902.

[73]   Seung Hoon Lee et al. "Towards visible soliton microcomb generation". In: *Nature communications* 8.1 (2017), pp. 1–8.

[74]   Jae K Jang et al. "Synchronization of coupled optical microresonators". In: *Nature Photonics* 12.11 (2018), pp. 688–693.

[75]   Qi-Fan Yang et al. "Counter-propagating solitons in microresonators". In: *Nature Photonics* 11 (2017), pp. 560–564.

[76]   Chaitanya Joshi et al. "Counter-rotating cavity solitons in a silicon nitride microresonator". In: *Optics letters* 43.3 (2018), pp. 547–550.

[77]   Erwan Lucas et al. "Spatial multiplexing of soliton microcombs". In: *Nature photonics* 12.11 (2018), pp. 699–705.

[78]   Jiang Li et al. "Electro-optical frequency division and stable microwave synthesis". In: *Science* 345.6194 (2014), pp. 309–313.

[79]   V Brasch et al. "Photonic chip–based optical frequency comb using soliton Cherenkov radiation". In: *Science* 351.6271 (2016), pp. 357–360.

[80]   Pei-Hsun Wang et al. "Intracavity characterization of micro-comb generation in the single-soliton regime". In: *Opt. Express* 24.10 (2016), pp. 10890–10897.

[81]   Chaitanya Joshi et al. "Thermally controlled comb generation and soliton mode-locking in microresonators". In: *Opt. Lett.* 41.11 (2016), pp. 2565–2568.

[82]   Thibault Wildi et al. "Thermally stable access to microresonator solitons via slow pump modulation". In: *Optics letters* 44.18 (2019), pp. 4447–4450.

[83]   Mengjie Yu et al. "Mode-locked mid-infrared frequency combs in a silicon microresonator". In: *Optica* 3.8 (2016), pp. 854–860.

[84]   Zheng Gong et al. "High-fidelity cavity soliton generation in crystalline AlN micro-ring resonators". In: *Optics letters* 43.18 (2018), pp. 4366–4369.

[85] Cheng Wang et al. "Monolithic lithium niobate photonic circuits for Kerr frequency comb generation and modulation". In: *Nature communications* 10.1 (2019), pp. 1–6.

[86] Yang He et al. "Self-starting bi-chromatic LiNbO$_3$ soliton microcomb". In: *Optica* 6.9 (2019), pp. 1138–1144.

[87] Zheng Gong et al. "Soliton microcomb generation at 2 μm in z-cut lithium niobate microring resonators". In: *Optics letters* 44.12 (2019), pp. 3182–3185.

[88] Martin HP Pfeiffer et al. "Photonic Damascene process for integrated high-Q microresonator based nonlinear photonics". In: *Optica* 3.1 (2016), pp. 20–25.

[89] Junqiu Liu et al. "Photonic microwave generation in the X-and K-band using integrated soliton microcombs". In: *Nature Photonics* (2020), pp. 1–6.

[90] Edik U Rafailov, Maria Ana Cataluna, and Wilson Sibbett. "Mode-locked quantum-dot lasers". In: *Nature photonics* 1.7 (2007), pp. 395–401.

[91] Zachary L Newman et al. "Architecture for the photonic integration of an optical atomic clock". In: *Optica* 6.5 (2019), pp. 680–685.

[92] Tara M Fortier et al. "Generation of ultrastable microwaves via optical frequency division". In: *Nature Photonics* 5.7 (2011), p. 425.

[93] Zhi Jiang et al. "Optical arbitrary waveform processing of more than 100 spectral comb lines". In: *Nature Photonics* 1.8 (2007), pp. 463–467.

[94] Steven T Cundiff and Andrew M Weiner. "Optical arbitrary waveform generation". In: *Nature Photonics* 4.11 (2010), pp. 760–766.

[95] Debabrata Goswami. "Optical pulse shaping approaches to coherent control". In: *Physics Reports* 374.6 (2003), pp. 385–481.

[96]   Matthew C Stowe et al. "High resolution atomic coherent control via spectral phase manipulation of an optical frequency comb". In: *Physical review letters* 96.15 (2006), p. 153001.

[97]   Itan Barmes, Stefan Witte, and Kjeld SE Eikema. "Spatial and spectral coherent control with frequency combs". In: *Nature Photonics* 7.1 (2013), pp. 38–42.

[98]   David J Geisler et al. "Modulation-format agile, reconfigurable Tb/s transmitter based on optical arbitrary waveform generation". In: *Optics express* 17.18 (2009), pp. 15911–15925.

[99]   Han-Sung Chan et al. "Synthesis and measurement of ultrafast waveforms from five discrete optical harmonics". In: *Science* 331.6021 (2011), pp. 1165–1168.

[100]   Vicente Durán, Santiago Tainta, et al. "Ultrafast electrooptic dual-comb interferometry". In: *Optics express* 23.23 (2015), pp. 30557–30569.

[101]   Vicente Durán, Peter A Andrekson, et al. "Electro-optic dual-comb interferometry over 40 nm bandwidth". In: *Optics letters* 41.18 (2016), pp. 4190–4193.

[102]   Fahmida Ferdous et al. "Dual-comb electric-field cross-correlation technique for optical arbitrary waveform characterization". In: *Optics letters* 34.24 (2009), pp. 3875–3877.

[103]   Xin Zhou et al. "Pair-by-pair pulse shaping for optical arbitrary waveform generation by dual-comb heterodyne". In: *Optics letters* 38.24 (2013), pp. 5331–5333.

[104]   Feifei Yin et al. "Broadband radio-frequency signal synthesis by photonic-assisted channelization". In: *Optics Express* 29.12 (2021), pp. 17839–17848.

130

[105] Vahid Ataie et al. "Subnoise detection of a fast random event". In: *Science* 350.6266 (2015), pp. 1343–1346.

[106] I Coddington, William C Swann, and Nathan R Newbury. "Coherent linear optical sampling at 15 bits of resolution". In: *Optics letters* 34.14 (2009), pp. 2153–2155.

[107] Jim-Wein Lin et al. "Photonic generation and detection of W-band chirped millimeter-wave pulses for radar". In: *IEEE Photonics Technology Letters* 24.16 (2012), pp. 1437–1439.

[108] Paolo Ghelfi et al. "A fully photonics-based coherent radar system". In: *Nature* 507.7492 (2014), pp. 341–345.

[109] Ingrid S Lin, Jason D McKinney, and Andrew M Weiner. "Photonic synthesis of broadband microwave arbitrary waveforms applicable to ultra-wideband communication". In: *IEEE Microwave and Wireless Components Letters* 15.4 (2005), pp. 226–228.

[110] Fahmida Ferdous et al. "Spectral line-by-line pulse shaping of on-chip microresonator frequency combs". In: *Nature Photonics* 5.12 (2011), pp. 770–776.

[111] Maroof H Khan et al. "Ultrabroad-bandwidth arbitrary radiofrequency waveform generation with a silicon photonic chip-based spectral shaper". In: *Nature Photonics* 4.2 (2010), pp. 117–122.

[112] Amir Rashidinejad and Andrew M Weiner. "Photonic radio-frequency arbitrary waveform generation with maximal time-bandwidth product capability". In: *Journal of Lightwave Technology* 32.20 (2014), pp. 3383–3393.

[113] Amir Rashidinejad, Daniel E Leaird, and Andrew M Weiner. "Ultrabroadband radio-frequency arbitrary waveform generation with high-speed phase and amplitude modulation capability". In: *Optics express* 23.9 (2015), pp. 12265–12273.

[114] Amir Rashidinejad, Yihan Li, and Andrew M Weiner. "Recent advances in programmable photonic-assisted ultrabroadband radio-frequency arbitrary waveform generation". In: *IEEE Journal of Quantum Electronics* 52.1 (2015), pp. 1–17.

[115] Jian Wang et al. "Reconfigurable radio-frequency arbitrary waveforms synthesized in a silicon photonic chip". In: *Nature communications* 6.1 (2015), pp. 1–8.

[116] Mengxi Tan et al. "Photonic RF arbitrary waveform generator based on a soliton crystal micro-comb source". In: *Journal of Lightwave Technology* 38.22 (2020), pp. 6221–6226.

[117] Abdul Rahim et al. "Open-access silicon photonics platforms in Europe". In: *IEEE Journal of Selected Topics in Quantum Electronics* 25.5 (2019), pp. 1–18.

[118] Cheng Wang et al. "Integrated lithium niobate electro-optic modulators operating at CMOS-compatible voltages". In: *Nature* 562.7725 (2018), pp. 101–104.

[119] Camiel Op de Beeck et al. "Heterogeneous III-V on silicon nitride amplifiers and lasers via microtransfer printing". In: *Optica* 7.5 (2020), pp. 386–393.

[120] Qianhuan Yu et al. "Heterogeneous photodiodes on silicon nitride waveguides". In: *Optics express* 28.10 (2020), pp. 14824–14830.

[121] Beichen Wang et al. "Vernier frequency division with dual-microresonator solitons". In: *Nature communications* 11.3975 (2020).

[122] Walt Kester. "Understand SINAD, ENOB, SNR, THD, THD+ N, and SFDR so you don't get lost in the noise floor". In: *MT-003 Tutorial, www. analog. com/static/importedfiles/tutorials/MT-003. pdf* (2009).

[123] H Heffner. "The fundamental noise limit of linear amplifiers". In: *Proceedings of the IRE* 50.7 (1962), pp. 1604–1608.

[124] H Kogelnik and A Yariv. "Considerations of noise and schemes for its reduction in laser amplifiers". In: *Proceedings of the IEEE* 52.2 (1964), pp. 165–172.

[125] Govind Agrawal. *Applications of nonlinear fiber optics*. Elsevier, 2001.

[126] Philippe M Becker, Anders A Olsson, and Jay R Simpson. *Erbium-doped fiber amplifiers: fundamentals and technology*. Elsevier, 1999.

[127] Govind P Agrawal. *Lightwave technology: telecommunication systems*. John Wiley & Sons, 2005.

[128] Emmanuel Desurvire and Michael N Zervas. "Erbium-doped fiber amplifiers: principles and applications". In: *Physics Today* 48.2 (1995), p. 56.

[129] Beichen Wang et al. "Towards high-power, high-coherence, integrated photonic mmWave platform with microcavity solitons". In: *Light: Science & Applications* 10.1 (2021), pp. 1–10.

[130] Shuangyou Zhang et al. "Terahertz wave generation using a soliton microcomb". In: *Optics express* 27.24 (2019), pp. 35257–35266.

[131] Tomohiro Tetsumoto et al. "300 GHz wave generation based on a Kerr microresonator frequency comb stabilized to a low noise microwave reference". In: *Optics Letters* 45.16 (2020), pp. 4377–4380.

[132] Dongin Jeong et al. "Ultralow jitter silica microcomb". In: *Optica* 7.9 (2020), pp. 1108–1111.

[133] Claude Cohen-Tannoudji, Jacques Dupont-Roc, and Gilbert Grynberg. *Photons and atoms-introduction to quantum electrodynamics*. 1997.

[134] Marlan O Scully and M Suhail Zubairy. *Quantum optics*. 1999.

[135] Dan F Walls and John D Harvey. *Quantum Optics VI: Proceedings of the Sixth International Symposium on Quantum Optics, Rotorua, New Zealand, January 24–28, 1994*. Vol. 77. Springer Science & Business Media, 2012.

[136] E Knill, R Laflamme, and G J Milburn. "A scheme for efficient quantum computation with linear optics". In: *Nature (London)* 409 (Jan. 2001), pp. 46–52. DOI: 10.1038/35051009.

[137] Alexander I Lvovsky, Barry C Sanders, and Wolfgang Tittel. "Optical quantum memory". In: *Nature photonics* 3.12 (2009), pp. 706–714.

[138] Matthew Pysher et al. "Parallel generation of quadripartite cluster entanglement in the optical frequency comb". In: *Physical review letters* 107.3 (2011), p. 030505.

[139] Moran Chen, Nicolas C Menicucci, and Olivier Pfister. "Experimental realization of multipartite entanglement of 60 modes of a quantum optical frequency comb". In: *Physical review letters* 112.12 (2014), p. 120505.

[140] Bo-Han Wu et al. "Quantum computing with multidimensional continuous-variable cluster states in a scalable photonic platform". In: *Physical Review Research* 2.2 (2020), p. 023138.

[141] Ulrik L Andersen et al. "30 years of squeezed light generation". In: *Physica Scripta* 91.5 (2016), p. 053001.

134

[142] Junaid Aasi et al. "Enhanced sensitivity of the LIGO gravitational wave detector by using squeezed states of light". In: *Nature Photonics* 7.8 (2013), pp. 613–619.

[143] Han-Sen Zhong et al. "Quantum computational advantage using photons". In: *Science* (2020), eabe8770. ISSN: 0036-8075.

[144] JM Arrazola et al. "Quantum circuits with many photons on a programmable nanophotonic chip". In: *Nature* 591.7848 (2021), pp. 54–60.

[145] Seth Lloyd and Samuel L Braunstein. "Quantum computation over continuous variables". In: *Physical Review Letters* 82 (1999), p. 1784.

[146] Nicolas C Menicucci et al. "Universal quantum computation with continuous-variable cluster states". In: *Physical review letters* 97.11 (2006), p. 110501.

[147] Nicolas C Menicucci, Steven T Flammia, and Olivier Pfister. "One-way quantum computing in the optical frequency comb". In: *Physical review letters* 101.13 (2008), p. 130501.

[148] Nicolas C Menicucci. "Fault-tolerant measurement-based quantum computing with continuous-variable cluster states". In: *Physical review letters* 112.12 (2014), p. 120504.

[149] Olivier Pfister. "Continuous-variable quantum computing in the quantum optical frequency comb". In: *Journal of Physics B: Atomic, Molecular and Optical Physics* 53.1 (2019), p. 012001.

[150] Akira Furusawa et al. "Unconditional quantum teleportation". In: *science* 282.5389 (1998), pp. 706–709.

[151] Xiaoying Li et al. "Quantum dense coding exploiting a bright Einstein-Podolsky-Rosen beam". In: *Physical review letters* 88.4 (2002), p. 047904.

[152] Hoi-Kwan Lau and Christian Weedbrook. "Quantum secret sharing with continuous-variable cluster states". In: *Physical Review A* 88.4 (2013), p. 042313.

[153] Frédéric Grosshans et al. "Quantum key distribution using gaussian-modulated coherent states". In: *Nature* 421.6920 (2003), pp. 238–241.

[154] Jonathan Roslund et al. "Wavelength-multiplexed quantum networks with ultrafast frequency combs". In: *Nature Photonics* 8.2 (2014), pp. 109–112.

[155] Shota Yokoyama et al. "Ultra-large-scale continuous-variable cluster states multiplexed in the time domain". In: *Nature Photonics* 7.12 (2013), pp. 982–986.

[156] Warit Asavanant et al. "Generation of time-domain-multiplexed two-dimensional cluster state". In: *Science* 366.6463 (2019), pp. 373–376.

[157] Mikkel V Larsen et al. "Deterministic generation of a two-dimensional cluster state". In: *Science* 366.6463 (2019), pp. 369–372.

[158] Seiji Armstrong et al. "Programmable multimode quantum networks". In: *Nature communications* 3 (2012), p. 1026.

[159] Ling-An Wu et al. "Generation of squeezed states by parametric down conversion". In: *Physical review letters* 57.20 (1986), p. 2520.

[160] Vincent Boyer, AM Marino, and PD Lett. "Generation of spatially broadband twin beams for quantum imaging". In: *Physical review letters* 100.14 (2008), p. 143601.

[161] Zhongzhong Qin et al. "Experimental generation of multiple quantum correlated beams from hot rubidium vapor". In: *Physical review letters* 113.2 (2014), p. 023602.

136

[162] Xuan Zhu et al. "Hypercubic cluster states in the phase modulated quantum optical frequency comb". In: *arXiv preprint arXiv:1912.11215* (2019).

[163] Haowei Shi et al. "Entanglement-assisted absorption spectroscopy". In: *Physical Review Letters* 125.18 (2020), p. 180502.

[164] Xueshi Guo et al. "Distributed quantum sensing in a continuous-variable entangled network". In: *Nature Physics* 16.3 (2020), pp. 281–284.

[165] Gregory S Kanter et al. "Squeezing in a LiNbO 3 integrated optical waveguide circuit". In: *Optics express* 10.3 (2002), pp. 177–182.

[166] JU Fürst et al. "Quantum light from a whispering-gallery-mode disk resonator". In: *Physical Review Letters* 106.11 (2011), p. 113901.

[167] Avik Dutt et al. "On-chip optical squeezing". In: *Physical Review Applied* 3.4 (2015), p. 044005.

[168] Micheal Stefszky et al. "Waveguide cavity resonator as a source of optical squeezing". In: *Physical Review Applied* 7.4 (2017), p. 044026.

[169] Francesco Lenzini et al. "Integrated photonic platform for quantum information with continuous variables". In: *Science advances* 4.12 (2018), eaat9331.

[170] Alexander Otterpohl et al. "Squeezed vacuum states from a whispering gallery mode resonator". In: *Optica* 6.11 (2019), pp. 1375–1380.

[171] Takahiro Kashiwazaki et al. "Continuous-wave 6-dB-squeezed light with 2.5-THz-bandwidth from single-mode PPLN waveguide". In: *APL Photonics* 5.3 (2020), p. 036104.

[172] Joel F Tasker et al. "Silicon photonics interfaced with integrated electronics for 9 GHz measurement of squeezed light". In: *Nature Photonics* 15.1 (2020), pp. 11–15.

[173]   Robert W Boyd. *Nonlinear optics.* Academic press, 2020.

[174]   Andrey B Matsko et al. "Optical hyperparametric oscillations in a whispering-gallery-mode resonator: Threshold and phase diffusion". In: *Physical Review A* 71.3 (2005), p. 033804.

[175]   Yanne K Chembo, Dmitry V Strekalov, and Nan Yu. "Spectrum and dynamics of optical frequency combs generated with monolithic whispering gallery mode resonators". In: *Physical review letters* 104.10 (2010), p. 103902.

[176]   Henning Vahlbruch et al. "Detection of 15 dB squeezed states of light and their application for the absolute calibration of photoelectric quantum efficiency". In: *Physical review letters* 117.11 (2016), p. 110801.

[177]   Kosuke Fukui et al. "High-threshold fault-tolerant quantum computation with analog quantum error correction". In: *Physical review X* 8.2 (2018), p. 021054.

[178]   T Herr et al. "Mode spectrum and temporal soliton formation in optical microresonators". In: *Phys. Rev. Lett.* 113.12 (2014), p. 123901.

[179]   Jiang Li et al. "Sideband spectroscopy and dispersion measurement in microcavities". In: *Optics express* 20.24 (2012), pp. 26337–26344.

[180]   Arne Kordts et al. "Higher order mode suppression in high-Q anomalous dispersion SiN microresonators for temporal dissipative Kerr soliton formation". In: *Optics letters* 41.3 (2016), pp. 452–455.

[181]   Hiroshi Murata et al. "Optical pulse generation by electrooptic-modulation method and its application to integrated ultrashort pulse generators". In: *IEEE Journal of Selected Topics in Quantum Electronics* 6.6 (2000), pp. 1325–1331.

[182]   Takao Aoki, Go Takahashi, and Akira Furusawa. "Squeezing at 946nm with periodically poled KTiOPO 4". In: *Optics express* 14.15 (2006), pp. 6930–6935.

[183] David R Carlson et al. "Ultrafast electro-optic light with subcycle control". In: *Science* 361.6409 (2018), pp. 1358–1363.

[184] Ming Cai, Oskar Painter, and Kerry J. Vahala. "Observation of Critical Coupling in a Fiber Taper to a Silica-Microsphere Whispering-Gallery Mode System". In: *Phys. Rev. Lett.* 85 (1 July 2000), pp. 74–77.

[185] Myoung-Gyun Suh et al. "Searching for exoplanets using a microresonator astrocomb". In: *Nature photonics* 13.1 (2019), pp. 25–30.

[186] Alexander W Bruch et al. "Pockels soliton microcomb". In: *Nature Photonics* 15.1 (2021), pp. 21–27.

[187] Juanjuan Lu et al. "Ultralow-threshold thin-film lithium niobate optical parametric oscillator". In: *arXiv preprint arXiv:2101.04735* (2021).

[188] Timothy P McKenna et al. "Ultra-low-power second-order nonlinear optics on a chip". In: *arXiv preprint arXiv:2102.05617* (2021).

[189] Luis Ledezma et al. "Intense optical parametric amplification in dispersion engineered nanophotonic lithium niobate waveguides". In: *arXiv preprint arXiv:2104.08262* (2021).

[190] Noel Lito B Sayson et al. "Octave-spanning tunable parametric oscillation in crystalline Kerr microresonators". In: *Nature Photonics* 13.10 (2019), pp. 701–706.

[191] Bei-Bei Li et al. "Quantum enhanced optomechanical magnetometry". In: *Optica* 5.7 (2018), pp. 850–856.

[192] Benjamin J Lawrie et al. "Quantum sensing with squeezed light". In: *ACS Photonics* 6.6 (2019), pp. 1307–1318.